N 71 10020
NASA CR-72767

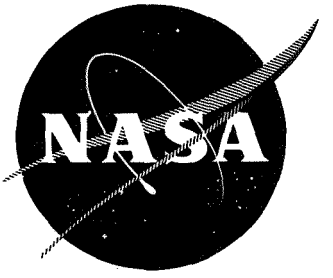

MULTISTAGE DEPRESSED ELECTROSTATIC COLLECTOR FOR MAGNETICALLY FOCUSED SPACE BORNE KLYSTRONS

by

W. Neugebauer and Dr. T. G. Mihran

GENERAL ELECTRIC COMPANY

prepared for

NATIONAL AERONAUTICS AND SPACE ADMINISTRATION

NASA Lewis Research Center

Contract NAS3-11532

G. J. Chomos, Project Manager

Requests for copies of this report should be referred to

National Aeronautics and Space Administration
Scientific and Technical Information Facility
P.O. Box 33
College Park, Md. 20740

NASA CR-72767

FINAL REPORT

MULTISTAGE DEPRESSED ELECTROSTATIC COLLECTOR
for
MAGNETICALLY FOCUSED SPACE BORNE KLYSTRONS

by

W. Neugebauer and T. G. Mihran

GENERAL ELECTRIC COMPANY
Tube Department
Microwave Tube Operation
Schenectady, New York

prepared for

NATIONAL AERONAUTICS AND SPACE ADMINISTRATION

September 14, 1970

CONTRACT NO. NAS3-11532

NASA Lewis Research Center
Cleveland, Ohio
G. J. Chomos, Project Manager
Spacecraft Technology Division

FOREWORD

The work reported herein was conducted at the General Electric Company, Schenectady, New York, under NASA Contract NAS3-11532. Mr. W. Neugebauer of the Microwave Tube Operation was Project Engineer assisted by Dr. T. G. Mihran of the Research and Development Center. Mr. Gerald J. Chomos, Spacecraft Technology Division, NASA-Lewis Research Center, was Project Manager.

TABLE OF CONTENTS

ABSTRACT

A ten-stage electrostatic depressed collector was designed with the aid of an analog computer and tested on a 750-MHz klystron under varying conditions of drive. The measured performance showed excellent agreement with the design theory. At the full saturated rf power output, in excess of one kilowatt CW, the action of the collector raised the undepressed conversion efficiency of the klystron from 54.3 to 70.9 percent. This performance could only be achieved through the use of a small focusing coil between the output gap and the collector. Without this coil the corresponding net tube efficiency would have been 65.3 percent. At a lower drive level the collector raised the undepressed conversion efficiency from 29.2 to 54.2 percent, an increase of 25 percentage points. No spurious oscillations or instabilities were detectable and electron backstreaming was virtually non-existent. Intentional short circuiting of individual collector electrode pairs was shown to cause only minor degradation in collector performance.

SUMMARY

A method based on analog computer trajectory calculations has been established for the design of depressed collectors. This design method includes the effect of initial transverse velocities and of magnetic fields in the collector. It is based on the performance observed on a four-stage electrostatic depressed collector constructed in the initial phases of the program. A ten-stage depressed collector built subsequently showed excellent agreement with the predicted performance characteristics under varying conditions of drive and output cavity coupling. This collector effectively suppresses secondary electron emission by means of the reflex collection principle, where electrons are collected in an electric field which tends to drive them into the surface. At the most negative electrode, secondary emission is controlled by a suppressor grid.

The ten-stage electrostatic depressed collector was demonstrated on a 750-MHz klystron having an rf output power in excess of one kilowatt CW. At full saturated power output the action of the collector raised the undepressed conversion efficiency of the klystron from 54.3 to 70.9 percent. This performance depended on the use of a small focusing coil between the output gap and the collector. The magnetic fields produced by this coil caused some refocusing of the spent beam and made it fit the collector structure somewhat better. Without this coil the net tube efficiency at the corresponding point would have been 65.3 percent. At a lower drive level this collector raised the undepressed conversion efficiency from 29.2 to 54.2 percent, an increase of 25 percentage points. Klystron input power was calculated from data measured with calibrated dc voltmeters and ammeters, while the rf output power was measured by calorimetric means. The output-cavity circuit efficiency of 90 percent was established by measuring the loaded and unloaded Q parameters. No spurious oscillations or instabilities were detectable and electron backstreaming was virtually nonexistent. It was also demonstrated that collector performance does not critically depend on the precise voltages present on the electrodes. Changes in voltage as high as ten percent on any single electrode or the short circuiting of individual electrode pairs did not seriously degrade the efficiency of the collector.

INTRODUCTION

A microwave power source with a high dc-to-rf power conversion efficiency is a prime requirement for space broadcasting applications. Without exception, the reports of five exploratory tube design contracts submitted to NASA in late 1968 indicated that the efficiency of both O-type and M-type microwave tubes would benefit greatly from use of a depressed collector to recover energy from the spent beam.

Although a depressed collector offers an excellent way of increasing tube efficiency in theory, in practice the actual operation of depressed collectors achieved on O-type tubes during the past decade has not been outstanding. Prior to 1970, depressed collectors were generally found to add ten points or less to the efficiency of tubes that had reasonably good undepressed efficiencies ($>$40 percent).

The renewal of interest in depressed collectors today is based on the premise that by taking advantage of the new analytic techniques that have become increasingly available during the past decade -- specifically the use of analog and digital computers -- depressed collectors can now be designed successfully.

A preliminary analog computer study performed under NASA Contract NAS3-11514 by the General Electric Company during 1968 disclosed a potentially interesting form of depressed collector, called a "reflex collector". The reflex collector is an electrostatic collector which is designed so that most electrons strike the collector electrode surfaces which face away from the cathode end of the tube. To do this, the electrons are slowed down and then are slightly reaccelerated before collection -- hence the name "reflex". If such a collector is designed properly by a careful study of electron trajectories, secondary electrons are almost completely suppressed. Furthermore, there is a tendency to achieve a focus in the orbits of returning electrons which have the same energy but which originated at different input conditions. Both of these features -- secondary electron suppression and refocusing upon reflection -- serve to increase the efficiency of a reflex collector.

The work reported here is the result of a fifteen month study to design and demonstrate a reflex collector on an operating klystron. Two collector/tube assemblies were tested, utilizing an interim and a final collector design. The interim model was built primarily to test mechanical assembly techniques

and to establish test equipment needs. The interim collector further served the important purpose of providing a base of measured data against which accurate computational techniques could be tested and improved. These techniques were then used to design the final collector.

The performance of the final collector is in excellent agreement with theoretical predictions. Moreover, its performance places it well above the performance of most collectors previously reported. As an example, the final reflex collector recovers 60 percent of the spent beam energy of a klystron whose base efficiency is 45 percent, raising net tube efficiency to 67 percent. This is an increase of twenty-two percentage points in net tube efficiency, in contrast to the ten or less previously reported.

In the next section, a brief description is given of collector performance as reported in the literature prior to 1970, as well as some basic concepts useful for collector evaluation. Subsequent sections include, respectively: a description of the test klystron and test equipment setup; some preliminary analog computer studies preceding the design of the interim collector; construction and evaluation of the interim collector; analog computer studies underlying the design of the final collector; construction and evaluation of the final collector; and our conclusions and recommendations for future work.

BACKGROUND AND BASIC CONCEPTS

Previously published work on depressed collectors and the basic concepts needed for collector evaluation are summarized in the following paragraphs.

SUMMARY OF PREVIOUS WORK

The most practical measure of the quality of a depressed collector is its ability to increase the efficiency of a tube from η_o, its base efficiency without depression, to a higher efficiency η, the net tube efficiency with depression. Collector performance reported in the literature from 1954 to 1968 is summarized in Figure 1. In this figure, net tube efficiency η is plotted as a function of base tube efficiency η_o. The data points indicated by filled-in circles and triangles represent cases in which the tube to which the collector was attached was a klystron tube. The hollow points represent data taken using traveling wave tubes. The high efficiency shown by Priest and Leidigh[1] was achieved with a single-stage electrostatic collector. They attribute their success to the narrow velocity spread present in the spent beam of an extended-interaction klystron.

The data of Figure 1 indicate that for tubes with low to moderate base efficiencies, collector depression has reportedly more than doubled tube efficiency in some cases. However, for high efficiency tubes ($40\% < \eta_o > 60\%$) collector depression in general has added ten points or less to the base tube efficiency.

With the exception of Chen (1963)[2], who used an eight-stage collector, the data shown in Figure 1 involved use of one- and two-stage collectors. It seems reasonable that a properly designed five- or ten-stage collector, such as that described in this report, could significantly improve on the performance shown in the figure.

BASIC CONCEPTS

In order to develop the relationships existing between the base tube efficiency η_o and the net tube efficiency η in terms of measured data, a few parameters must be defined. In the following discussion, all voltages are measured with respect to the tube body, which is generally at ground potential.

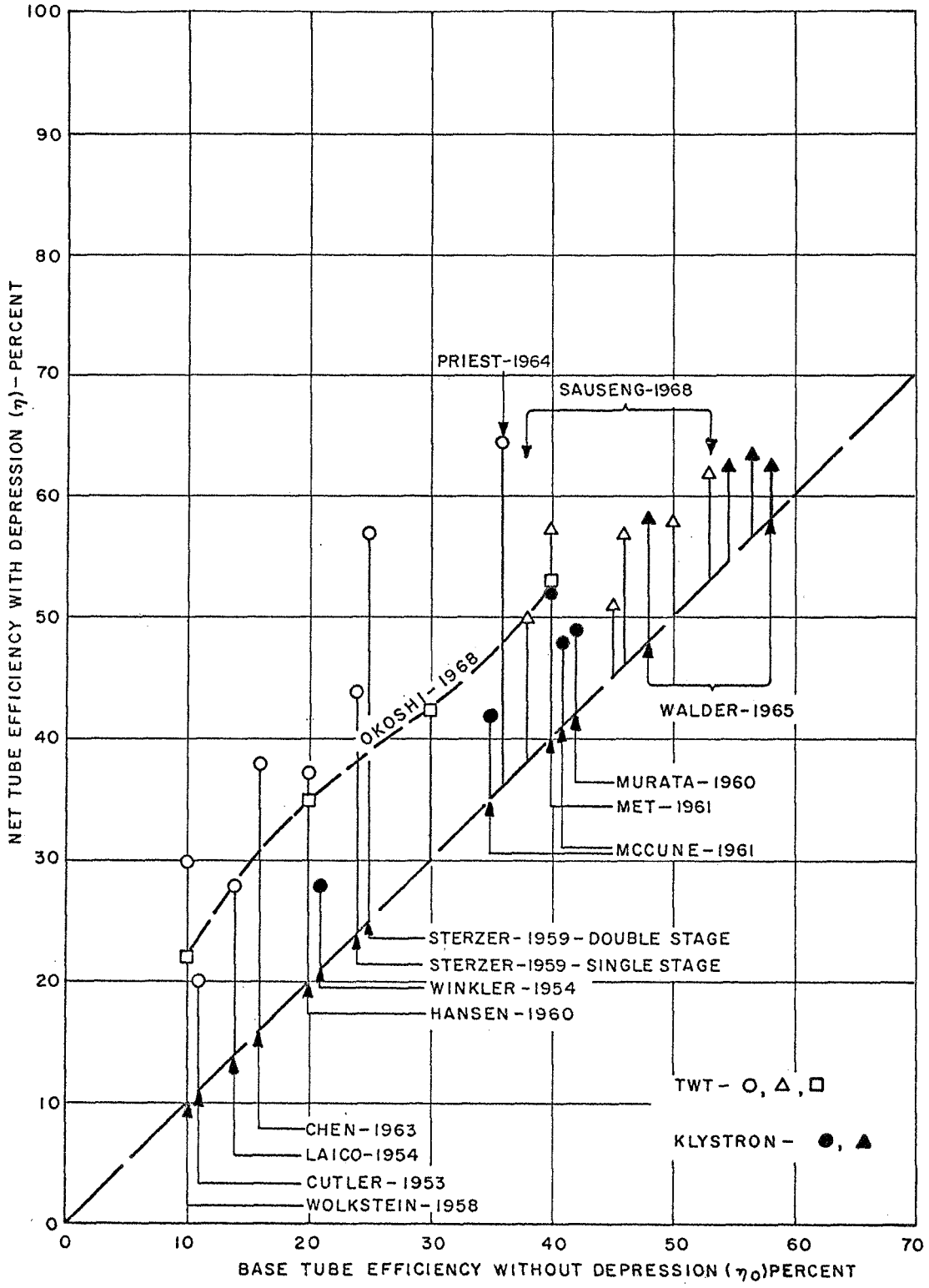

Figure 1 - Efficiency with Depression versus Undepressed Efficiency

If the cathode voltage is V_o and the cathode current is I_o, then the power P_o flowing into the tube is given by

$$P_o = I_o V_o \tag{1}$$

In regular tube operation, without collector depression, this would be the net input power. With collector depression, however, the net input power will be less than P_o. Suppose a depressed collector has N electrodes with the i'th electrode at a potential V_i with respect to the tube body and that this electrode collects a current I_i. If V_i were a battery, the flow of the current I_i under normal conditions will be such that the battery will be charged. The power P_{rec} recovered through the depressed collector is clearly given by

$$P_{rec} = \sum_{1}^{N} V_i I_i \tag{2}$$

In applying this relationship to measured data, care must be taken to observe the direction of the current flow, which may reverse under certain conditions involving large secondary emission coefficients. The net power into the tube with collector depression is the difference between P_o and the recovered power.

$$P_{net} = P_o - P_{rec} \tag{3}$$

Generally not all of the current I_o reaches the collector because some fraction is intercepted on the body of the tube. If under dc conditions the intercepted body current is I_{bdc} and under rf conditions at the same cathode voltage this current is I_{brf}, then the continuity equation requires that

$$I_o - \sum_{1}^{N} I_i = \begin{cases} I_{bdc} & \text{dc conditions} \\ I_{brf} & \text{rf conditions} \end{cases} \tag{4}$$

The intercepted dc current impinges on the drift tube wall with an energy corresponding to the full beam voltage V_o. The additional current intercepted when rf power is generated impinges with energies below V_o because some energy has been converted to useful rf power. Generally most of this

additional current is collected on the second half of the output cavity, or just after the main rf interaction. It is useful to denote by αV_o the energy with which this additional current impinges on the tube structure.

The rf power generated by the tube is denoted by P_{rf} and the power delivered to an external load will be slightly less due to circuit losses in the output cavity and the coupling mechanism. The output power P_{out} is therefore given by

$$P_{out} = \eta_{ckt} P_{rf} \tag{5}$$

where η_{ckt} is the circuit efficiency which can be established by measuring the loaded and unloaded Q of the output cavity. Thus,

$$\eta_{ckt} = 1 - Q_L/Q_U \tag{6}$$

Having developed the basic concepts regarding power flow in the tube and collector, it is now possible to compute the efficiencies associated with rf performance. The base tube conversion efficiency is clearly defined by

$$\eta_o = P_{rf}/P_o \tag{7}$$

while the net tube conversion efficiency is given by

$$\eta = P_{rf}/(P_o - P_{rec}) = P_{rf}/P_{net} \tag{8}$$

where P_{net} is the total dc input power. The collector efficiency $\eta_{c\text{-}rf}$ is more difficult to compute because of the added complication of intercepted current. While it is easy enough to define the collector efficiency as the ratio of the recovered power to the total power entering the collector, it is relatively difficult to determine the latter quantity. In the absence of intercepted current, the collector efficiency is easily computed to be the ratio of the recovered power to the difference between P_o and the generated rf power.

$$\eta_{c\text{-}rf} = P_{rec}/(P_o - P_{rf}) \quad \text{(no interception)} \tag{9}$$

The effect of body interception can be taken into account approximately, however, by writing

$$\eta_{c\text{-}rf} = P_{rec}/\left[P_o - P_{rf} - V_o I_{bdc} - \alpha V_o (I_{brf} - I_{bdc})\right] \tag{10}$$

where the additional terms in the denominator represent the power intercepted on the drift tube. The fraction α may be anywhere between zero and one. In this report, α is assumed to be 0.5 for both the interim collector and the final collector. Because there is no universal agreement as to the proper choice of this parameter, the results obtained with the final collector are presented with α equal to 0.5 and zero. Since the tube transmission was reasonably good, the difference in the two values of $\eta_{c\text{-}rf}$ is relatively minor.

The basic relationships developed here are used in the remainder of this report for analyzing the measured data. The concept of recovered power may sound superfluous as it pertains to power supply design, but it is helpful in visualizing the behavior of depressed collectors. A similar analysis based on net power flow with all voltages referred to cathode has been shown to yield the same equations for the various efficiencies.

TEST KLYSTRON AND TEST SET

OPERATING PARAMETERS AND CONSTRUCTION

The klystron used for demonstrating the reflex depressed collectors is a standard General Electric Z-5061 tube (similar to Eimac 3K3000LQ tube). This klystron has three external tunable cavities and exhibits the electrical performance listed in Table I.

- - - - - - -

TABLE I - Z-5061 KLYSTRON PARAMETERS

Beam perveance	0.1 to 0.7 microperveance, controlled via non-intercepting electrode
Beam voltage	9 kilovolts maximum
Frequency	Tunable 650 to 800 MHz
Bandwidth	Variable up to approx. 4 MHz
Output power (sat.)	1 to 2 kilowatts CW
Efficiency	45 to 50 percent, undepressed
Gain	18 to 24 dB (depends on perveance)
Focusing	Brillouin flow

- - - - - - -

The klystron is solenoid focused and requires a field strength of approximately 250 gauss. The mechanical layout of the klystron, with a conventional undepressed collector, is shown in Figure 2. The tube body is air cooled by means of the fins attached to the drift sections. The conventional collector is forced-air cooled and dissipates between one and two kilowatts of power. The three cavity ceramic cylinders and the cathode insulator are identical. A shorter alumina cylinder is used between the output cavity and the collector to allow measurement of collector current. This insulator was also retained for the depressed collector demonstration to allow measurement of the collector housing current.

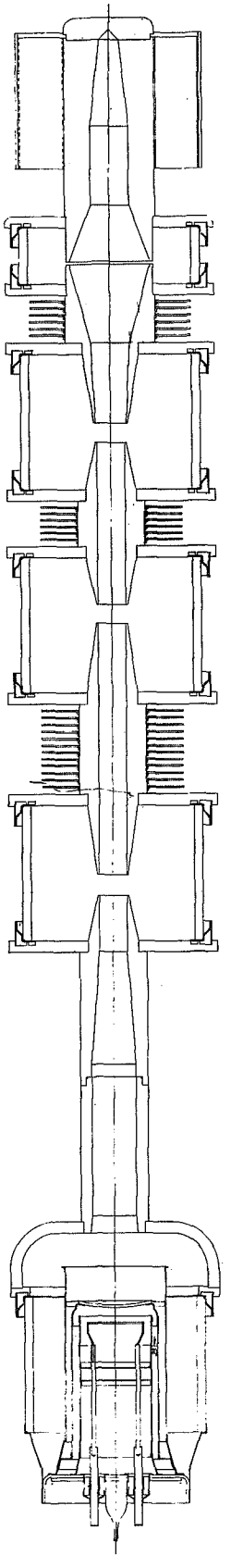

Figure 2 - Z-5061 Klystron Layout

TEST SET

A schematic drawing of the test circuit for the interim collector is given in Figure 3. The test circuit for the final collector was the same except that more of the 35 taps on the 3500-ohm divider resistor were used. The current and voltage at each collector electrode were individually monitored with the meters labeled I_{1-4} and V_{1-4}. The spike and cup, which were generally operated at the same voltage, are shown electrically shorted. Current which enters the collector but is unable to reach any active electrode is measured with the collector housing ammeter labeled I_{CH}. Since the tube body is grounded for safety, the intercepted current must be measured between the power supply positive terminal and ground with the meter I_B. The cathode voltage and current are measured by the meters shown while the focus control electrode voltage and current are monitored by the bias meters. The bias voltage is generally several hundred volts negative with respect to the cathode while the bias current is zero under all conditions.

The rf power flow during testing is measured through directional couplers and a thermistor type power bridge as shown in Figure 3, with an absolute calibration of the output power being established by calorimetric means. The power meter was calibrated near saturated tube output and this calibration was assumed to hold linearly for lower values of output power.

All the voltmeters and ammeters used in the test set have been calibrated and the overall accuracy of the measurements is approximately two percent.

All tests were made with dc voltages on the cathode and electrodes so that transient effects could not appear. The gas pressure, body current, magnetic field, water flow, cathode current, and divider temperature were interlocked with the supply so that any unusual condition immediately removed the dc power from the tube, thus preventing any damage. Collector oscillations were suppressed by placing a bypass capacitor in series with a 12-ohm resistor from each electrode to ground with the shortest possible lead lengths. In addition, a 20-ohm resistor was placed close to the collector feedthroughs in each line coming from the 3500-ohm divider. Besides dampening any possible oscillations, the latter resistors also acted as crude fuses, protecting the electrodes from serious arc damage.

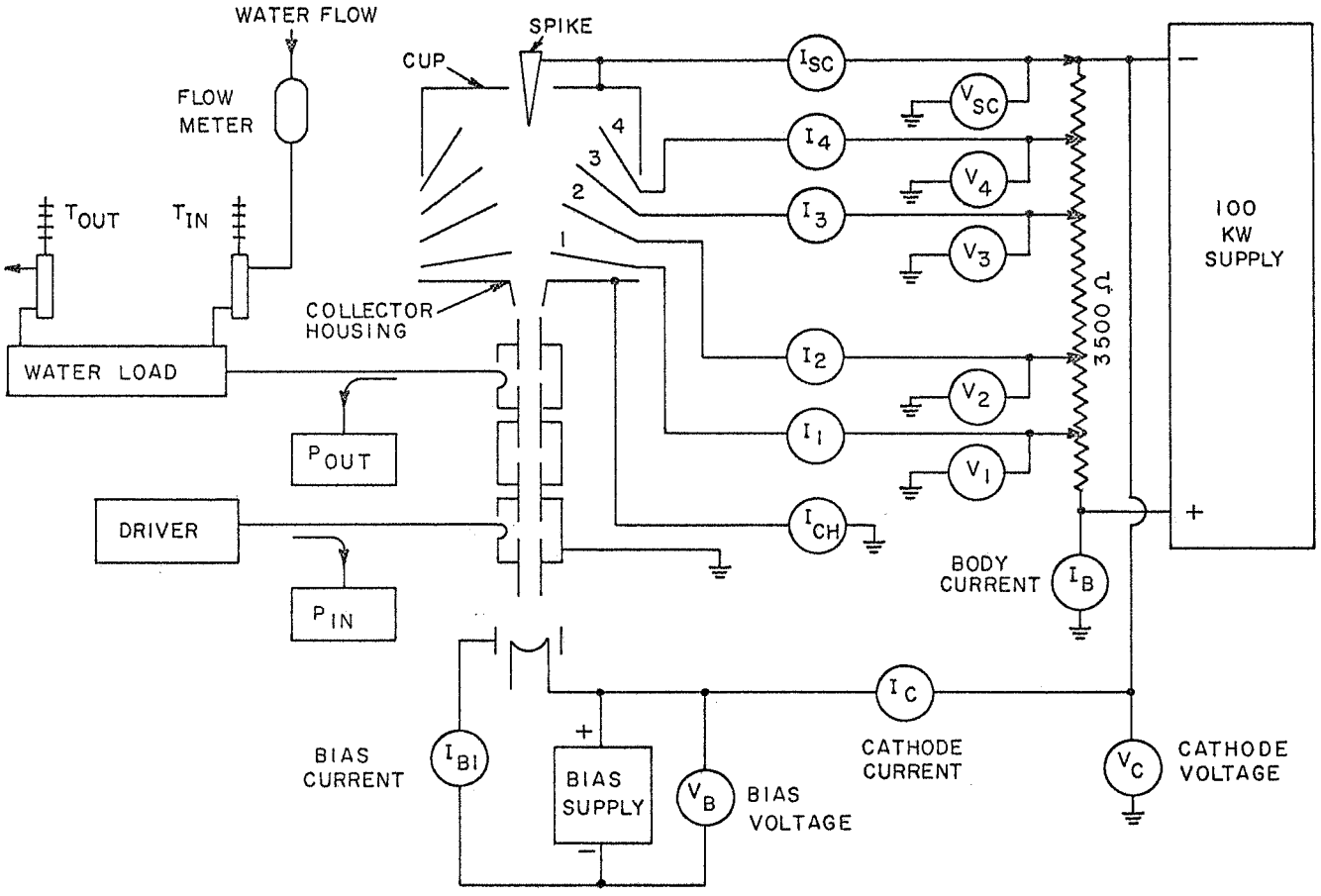

Figure 3 - Test Set Circuit

INTERIM COLLECTOR

ANALOG COMPUTER STUDIES FOR INTERIM COLLECTOR

Description of Analog Computer System

Design studies of the reflex depressed collectors were conducted on electrical models set up on a precision resistor network integrated with two PACE analog computers and an array of current sources for the simulation of space charge. A view of this facility is given in Figure 4, while Figure 5 depicts the resistor network and probe assembly. In operation, the metallic boundaries of a given electrode system are defined by interconnecting appropriate nodes of the network, and a 100-volt potential is applied between the simulated tube body and the most negative collector electrode. The four-point probe, which is servo controlled by the computer, reads the potential and the potential gradient at a given point in the region between electrodes, and the electron trajectories are computed and plotted on an X-Y recorder. A stepping voltage generated in the computation moves the probe assembly from one resistor cell to the next in the direction of the trajectory. After an initial run to solve the space-charge free problem, the current sources may be used to simulate space charge by injecting appropriate currents at the resistor nodes. For exploratory studies, it is usually sufficient to approximate the space charge rather crudely. Magnetic field effects are entered into the computations by means of a curve-follower X-Y plotter, upon which the measured axial magnetic field profile is plotted.

Magnetic Field Profile

The magnetic field associated with the focusing coils of the test klystron was carefully measured with particular attention being given to leakage fields in the collector region. Under typical tube operating conditions it was established that these leakage fields were much too large for successful reflex collector operation. A layered Mu-metal shield was therefore constructed and was shown to reduce the leakage field to an acceptable level of a few gauss. Figure 6 shows the measured magnetic field profile that was used in the analog computer design of the interim collector. If excessive leakage fields were allowed in the collector, the magnetic refocusing of electrons would not be conducive to efficient collection and considerable backstreaming into the rf interaction region might also result.

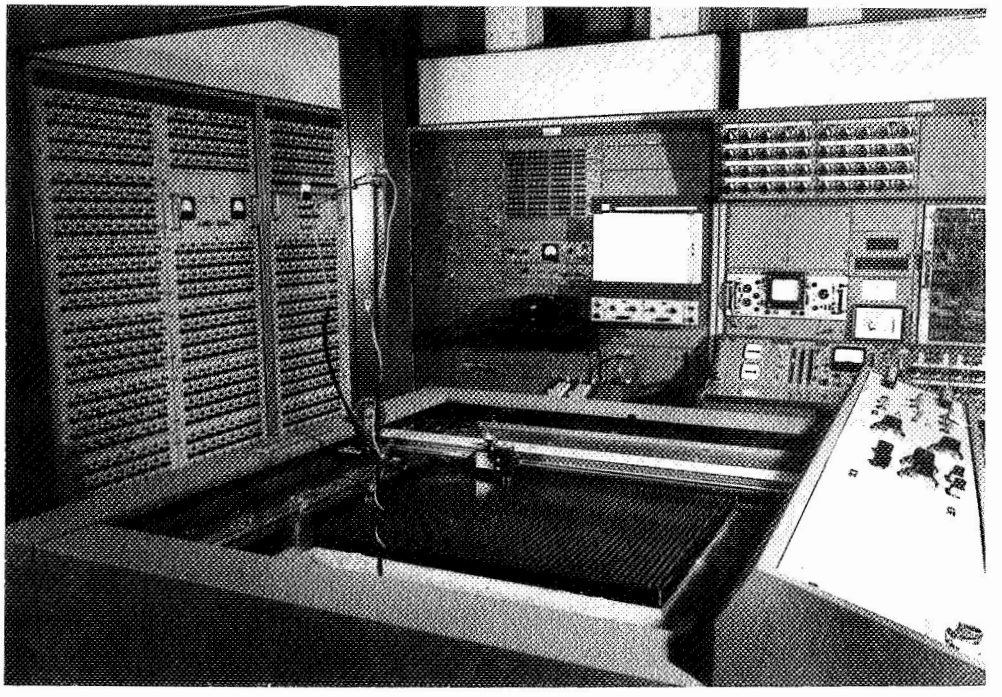

Figure 4 - General View of Analog Computer Beam Optics Facility

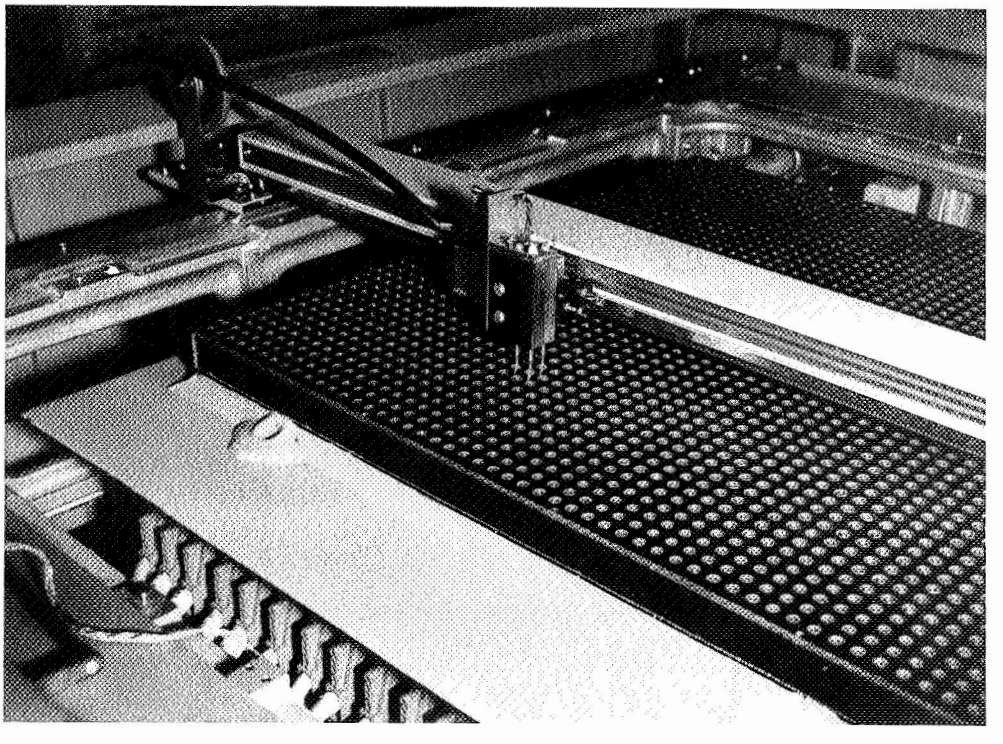

Figure 5 - Resistor Network and Potential Probes

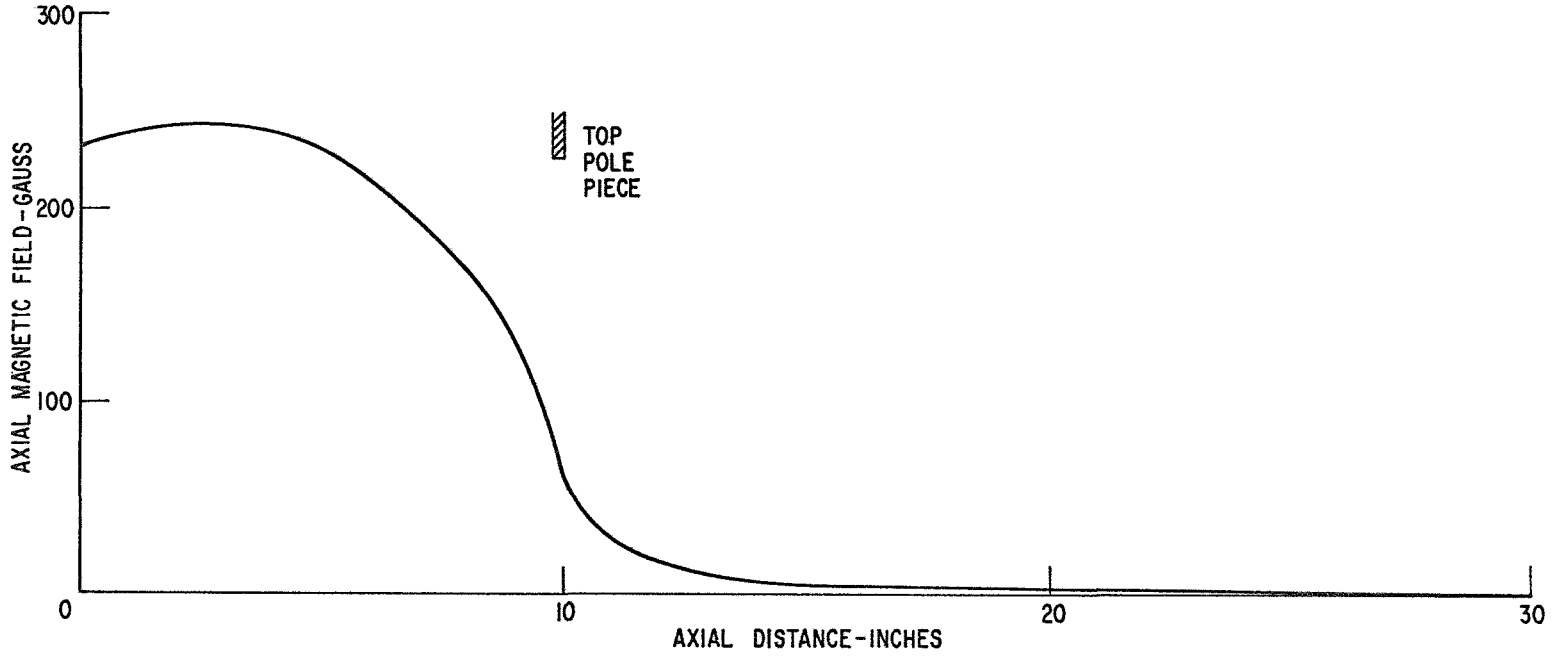

Figure 6 - Axial Magnetic Field Profile for Z-5061 Klystron

Collector Entrance Conditions

The single, most important unknown item in the design of the interim collector was the vector velocity distribution of the spent klystron beam. The first simple assumption was that the spent beam is parallel with a diameter corresponding to the equilibrium conditions associated with the magnetic field. This assumption was used in the interim collector design.

In order to obtain a better understanding of the spent beam velocities, a short analog computer program was written for calculating electron trajectories near the output gap. This program was based on the following assumptions:

(a) laminar flow at the klystron input gap

(b) axial space-charge forces are negligible

(c) linear buildup (or decay) of space charge from input to output gap

(d) a $\cos^2 (\beta - z)$ rf field distribution in the output gap

(e) non-relativistic motion

(f) constant magnetic field

(g) no rf magnetic field effects

(h) magnetically shielded cathode

With these assumptions the equations of motion mechanized on the analog computer were

$$\ddot{r} = \frac{eI}{2m\epsilon_o \pi r \dot{z}} + \frac{e}{m}\left\{\frac{\pi A r}{4\ell} \sin\frac{\pi z}{\ell} \sin(\omega t + \theta)\right\} - r\left(\frac{e B_z}{2m}\right)^2 \qquad (11)$$

$$\ddot{z} = -\frac{e}{m} A \cos^2\left|\frac{\pi z}{2\ell}\right| \sin(\omega t + \theta) \qquad (12)$$

where A = peak rf field strength

ℓ = gap length

I = beam current (varies linearly with z)

r, z = radial, axial displacements

B_z = axial magnetic field strength

The other symbols are standard notation. The output gap is centered at $z = 0$ and the computer is programmed to make $A = 0$ for $|z| > \ell$.

Typical results from this program are shown in Figure 7 where the beam edge is given as a function of rf voltage amplitude. Interception on the output drift tube appears to occur just below 7 kV/cm peak rf field strength. The linear rise in radial space-charge force associated with the bunch causes the beam to expand as it moves from the input to the output gap. The beam ripple just before the output gap is approximately 10 percent. At the output gap, the bunch is acted upon by radial defocusing and then a focusing field, but the main perturbation comes from the axial field which extracts rf energy. The increased space-charge forces cause rapid dispersion of the electrons in the bunch. These results indicate that the slowest electrons have the greatest entrance angles at the collector input. This model and the parallel beam model were used in designing the final collector.

Investigation of Collector Geometries

Various collector geometries were analyzed by means of the analog computer to determine the most promising design. Both constructional simplicity and electrical performance were taken into consideration. The different geometries are described in the paragraphs which follow.

Disk Collector: This collector consists of a series of large washers axially spaced along the spent beam. The design was rejected because it appeared to be incapable of slowing down electrons having considerable radial velocity, either as a result of the rf interaction or the action of the centrally located dispersion spike. When the final collector was being designed later in the program, however, it was found that a disk collector could have satisfactory electrical performance if careful attention were paid to the apertures in the electrodes and their location.

Cylinder Collector: In this collector, Figure 8, the electrodes are a set of concentric cylinders having different axial lengths. Analog investigation of this model showed that a large number of electrons were reflected directly back into the drift tube. This design was therefore judged unacceptabl

Deep Collector with Dispersion Spike: This reflex collector, Figure 9, has a long, narrow shape, with a centrally located dispersion spike. Analog study of this model showed that a large fraction of the electrons did not fountain outward as they should, but rather turned toward the axis as they were reflected. Many electrons were also reflected back into the drift tube. This design, too, was deemed unacceptable.

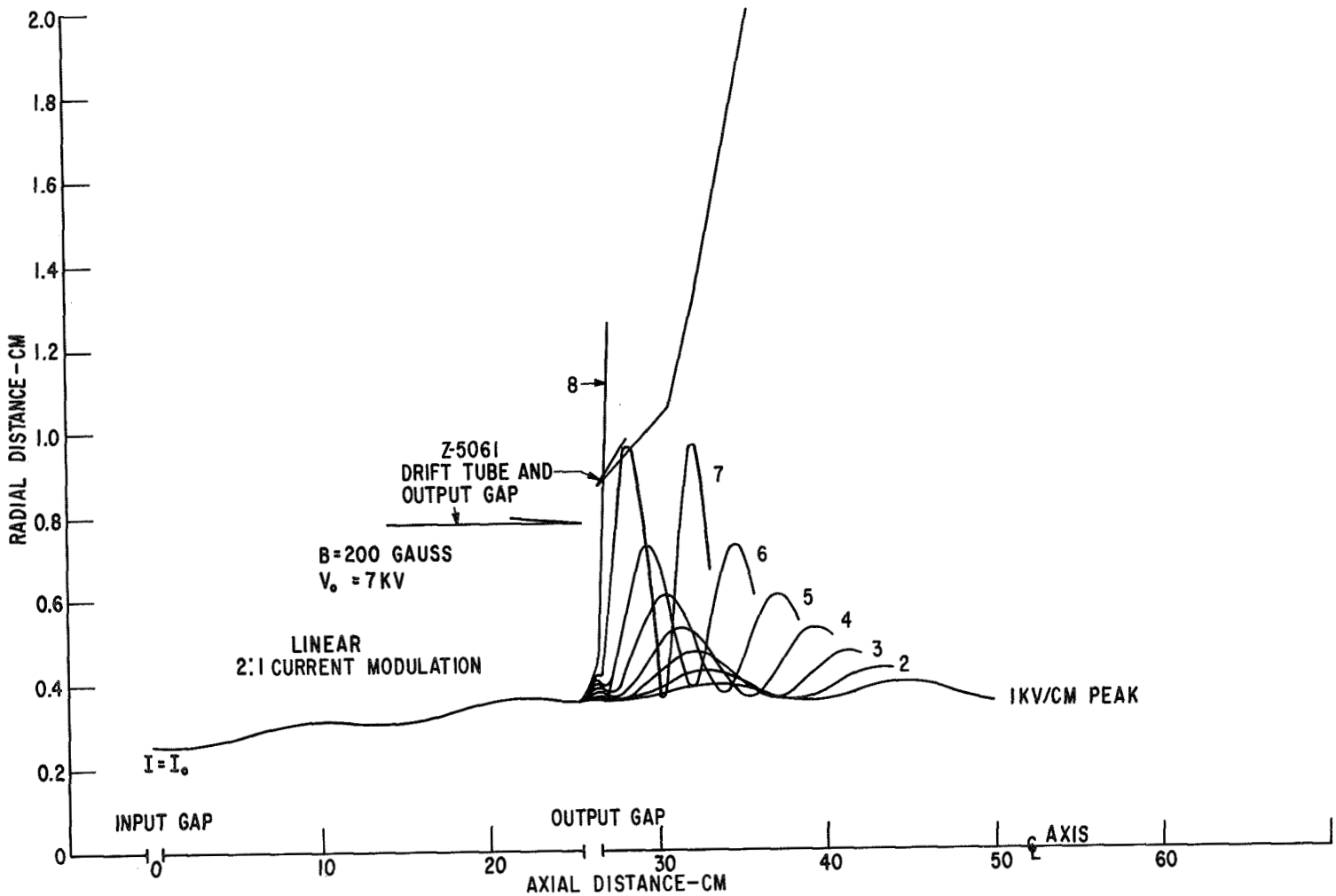

Figure 7 - Beam Envelope Variations with RF Output Gap Voltage

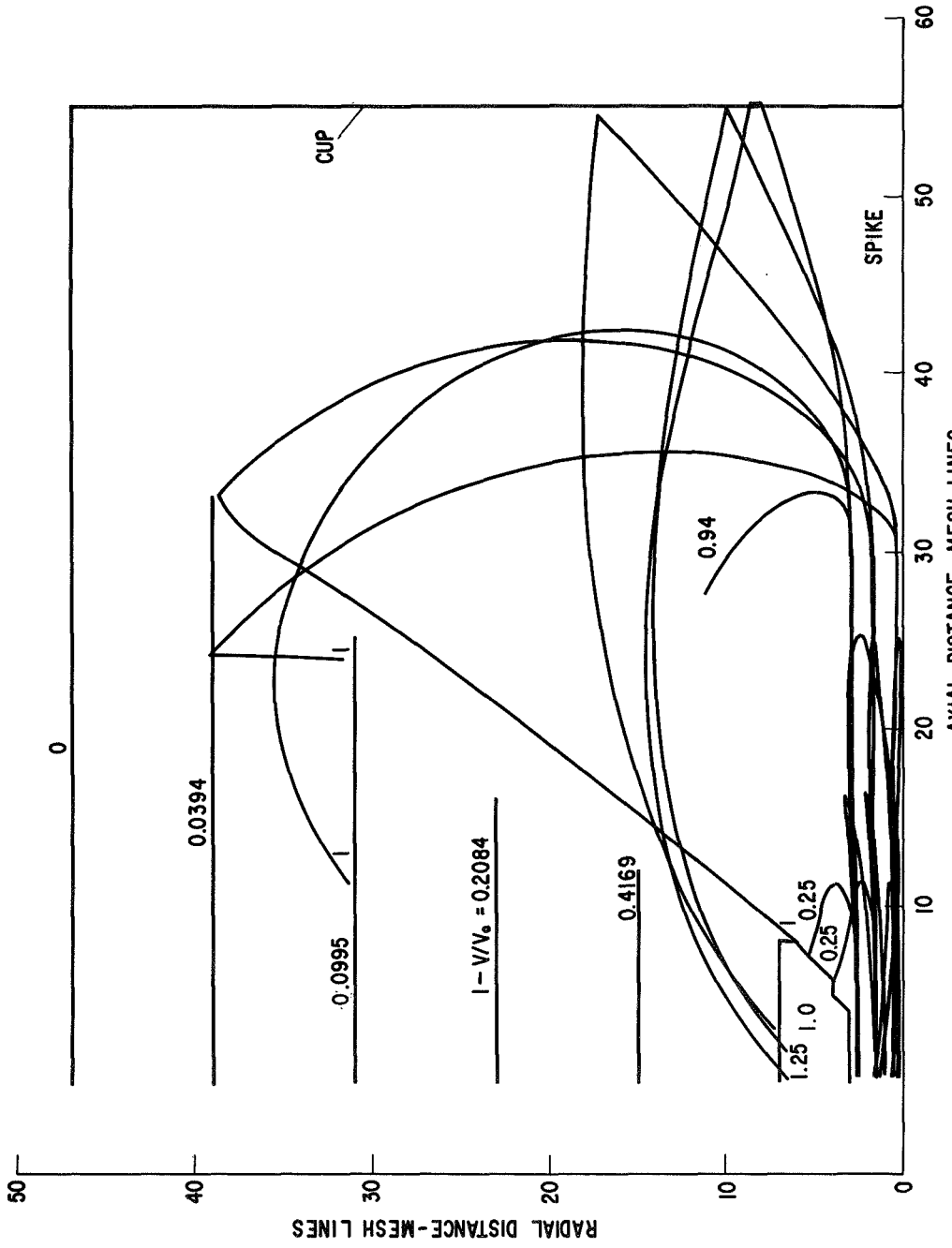

Figure 8 - Cylinder Collector Trajectories

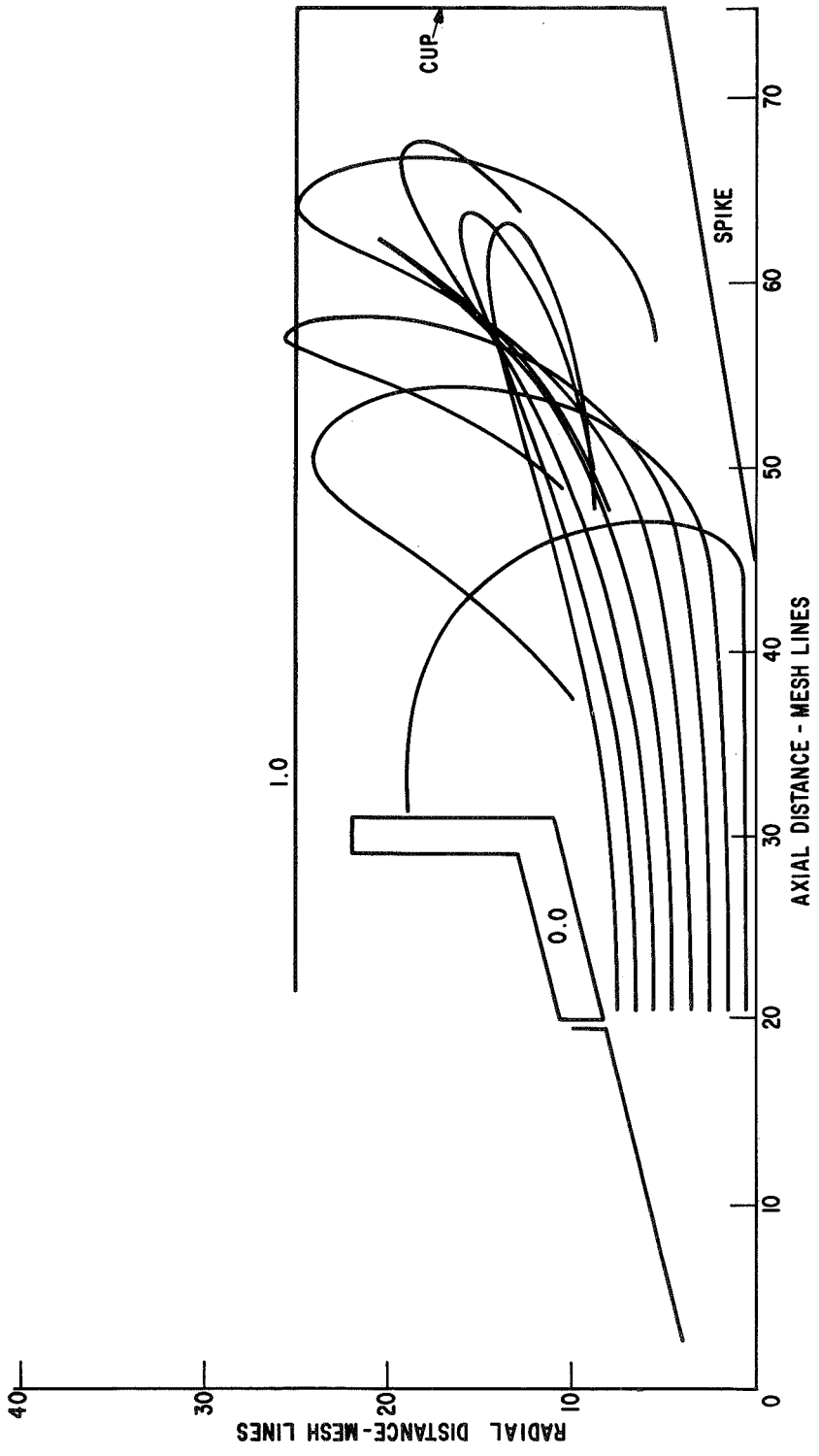

Figure 9 - Deep Collector Trajectories

Toroidal Collector: This type of reflex collector, Figure 10, has electrodes which are portions of toroidal surfaces axially spaced, with concentric apertures. The final electrode is a toroidal surface having a cusp on the axis which acts as a dispersion spike. Analysis of this design showed that electrons entering the collector smoothly convert their axial velocity into radial velocity without the desirable large reduction in kinetic energy necessary for efficient performance. This design was also rejected.

Selection of Square-Aspect-Ratio Collector as Interim Design: Trajectories associated with this collector are shown in Figure 11, together with the proposed electrodes (heavy lines) and the equipotentials. The trajectories have parallel entry, starting at radii consistent with Brillouin flow. The magnetic field measured previously was included in the calculation. Five energy classes and four radii having equal currents between them are given in Figure 11. Further analog studies of this model using different entrance conditions indicated no obvious defects. The computations included a study of very slow electron classes which showed that only an insignificant number (less than 0.1 percent) of electrons is capable of returning to the interaction region. In this design, secondary electrons are always intercepted on intermediate electrodes and cannot return to the drift tube. The energy margin for a four plate collector appears to be 30 percent and is only a very weak function of the electrode potentials. In other words, the collector supply voltages could have poor regulation without serious drawbacks. This design was chosen for the interim collector.

CONSTRUCTION OF INTERIM COLLECTOR

A layout of the interim collector is given in Figure 12, which depicts the various electrodes and the insulators. All the active electrodes are water cooled by means of stainless-steel pipes brazed to the copper surfaces. The dispersion spike incorporates a molybdenum tip to withstand possible heating due to positive ions. The main body of the spike is made of copper which is cooled by an axially located water jet not shown in the figure. The entire collector housing is made of non-magnetic stainless steel and is heavy enough to have negligible deflection when full atmospheric pressure is applied. It is connected to the Z-5061 tube by means of the collector insulator so that current to the housing may be monitored. Also shown is the second half of the klystron output cavity. An ion pump was attached to the collector to ensure that good vacuum conditions would be maintained in the tube.

All vacuum seals on the interim collector are either brazed or are welded disk flanges. Welded flanges facilitate collector repair if such become

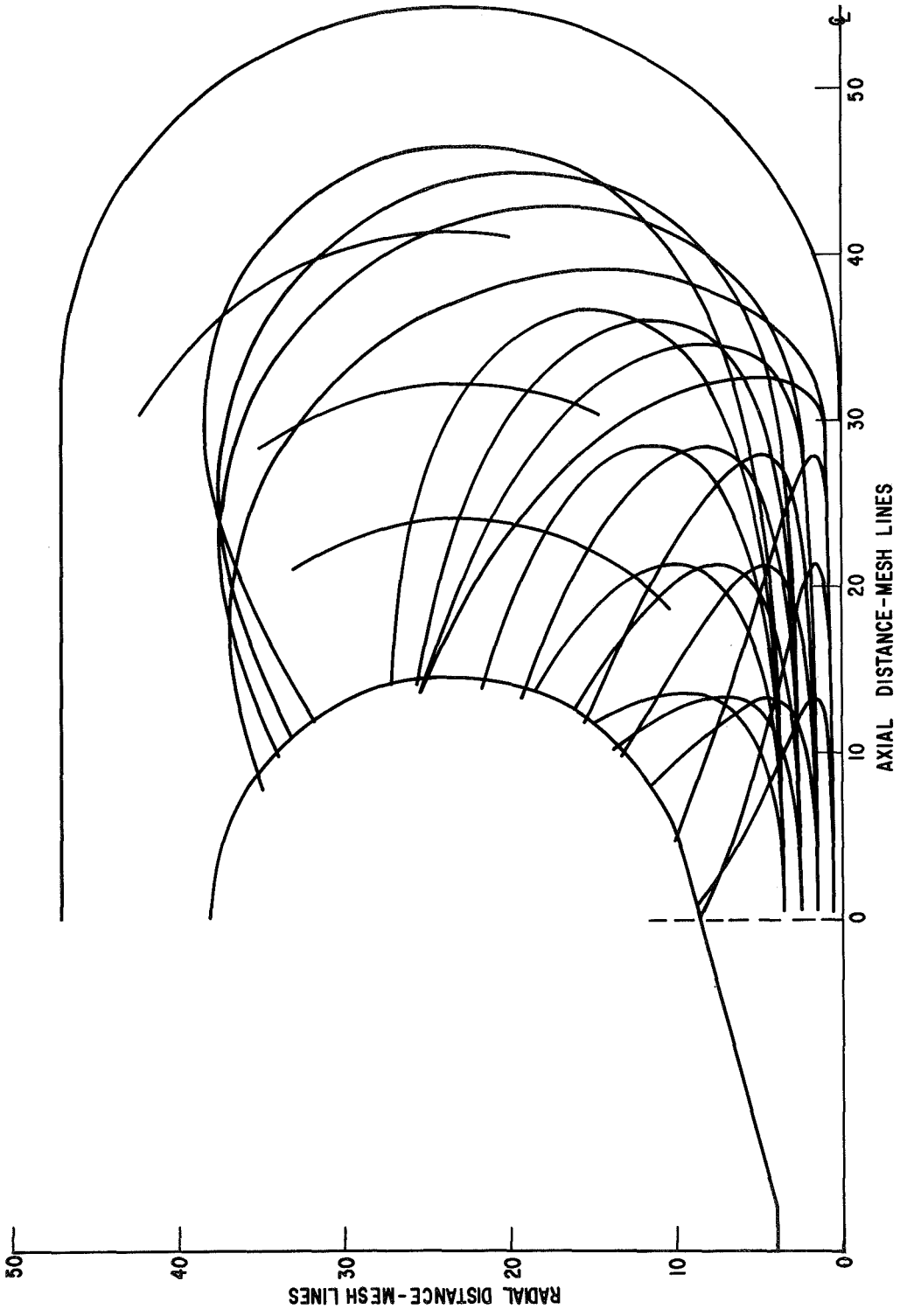

Figure 10 - Toroidal Collector Trajectories

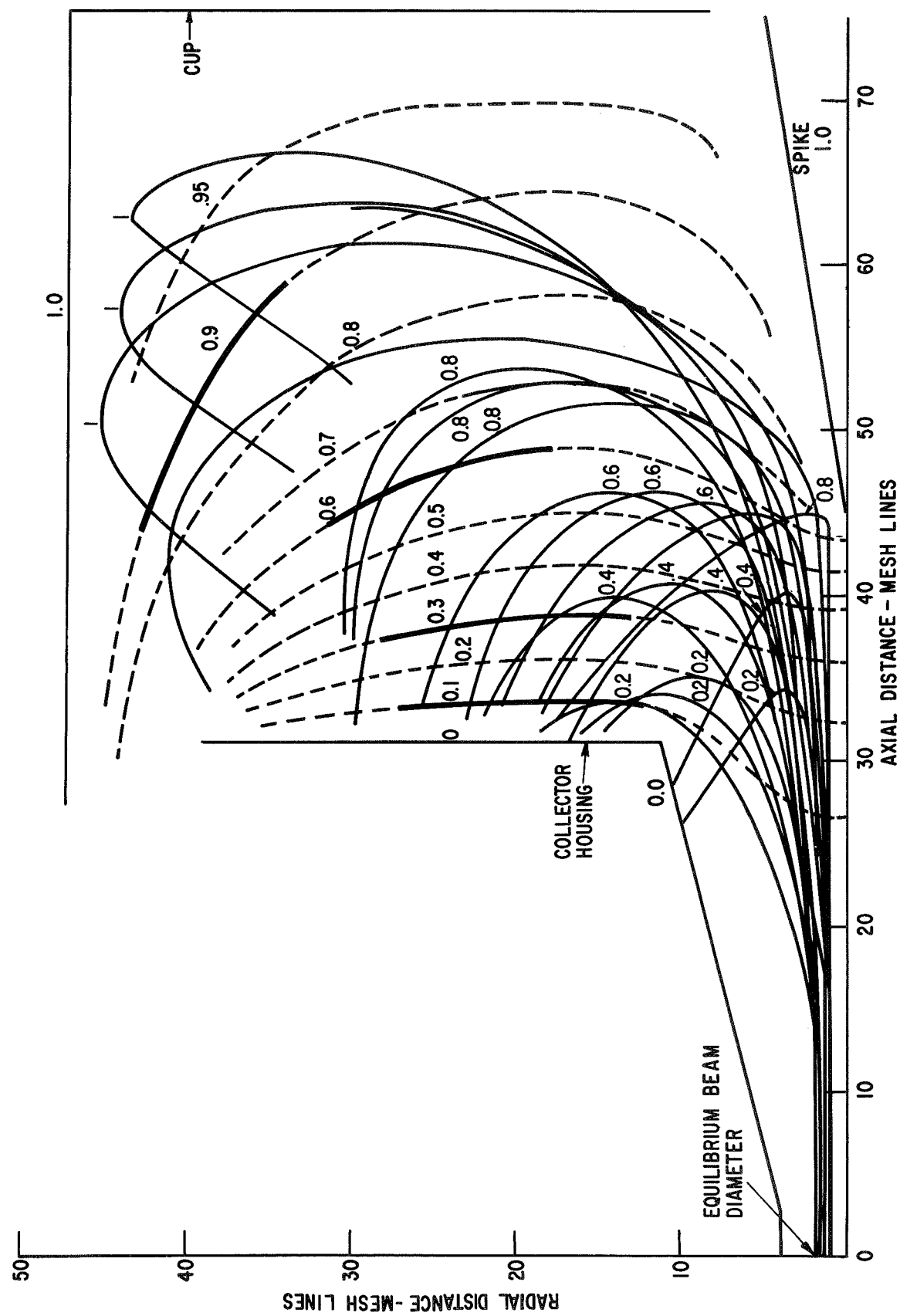

Figure 11 - Interim Collector Trajectories

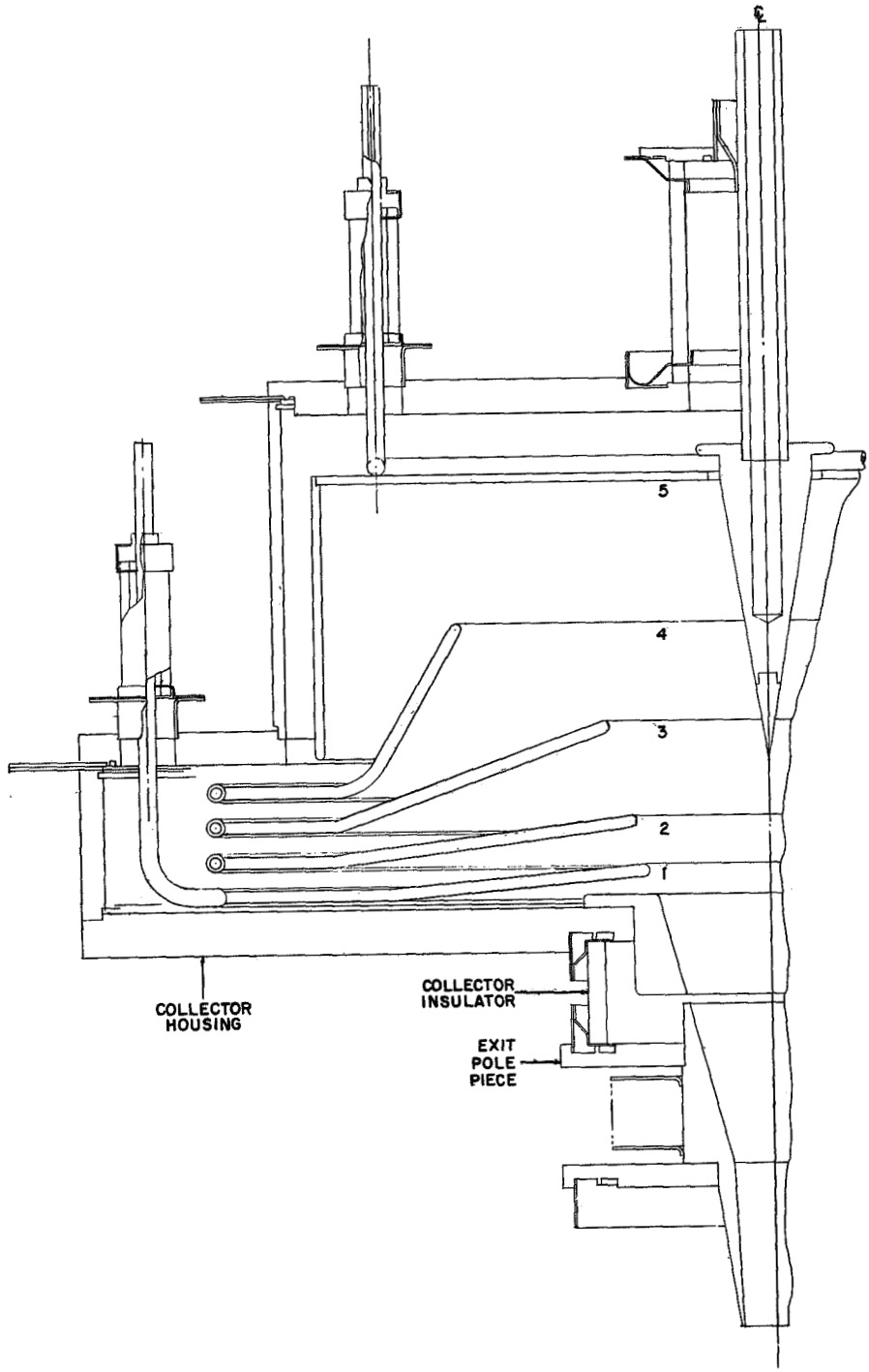

Figure 12 - Interim Collector Layout

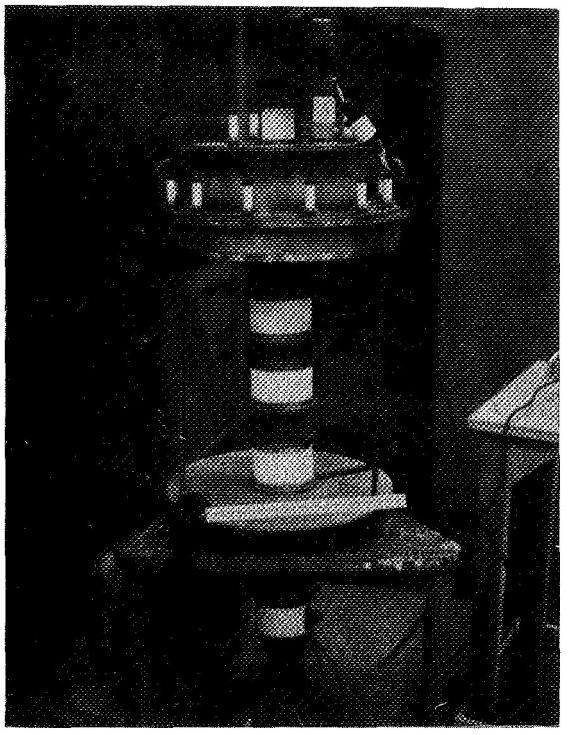

Figure 13 - Interim Depressed Collector and Klystron

necessary. The klystron-collector combination was purposely constructed as a sealed-off vacuum system to avoid the leakage and outgassing problems associated with demountable systems. Collector and tube were processed according to standard practices used in the manufacture of vacuum tubes.

Before attaching the collector, the cathode of the klystron was cleaned and recoated with oxide emission mix. Leak checking and other quality control procedures were also conducted in the same manner as applicable to regular production tubes. A cracked ceramic seal which was discovered after exhaust was quickly replaced. The second tube exhaust with another new cathode coating proved to be successful. A photograph of the tube and the interim collector is shown as Figure 13. A 12-inch architect's rule is shown near the input cavity ceramic seal for appropriate dimensional comparison.

EVALUATION OF INTERIM COLLECTOR

The performance of the interim collector was investigated on three levels: (1) current division as a function of dc beam voltage, (2) dc collector efficiency as a function of dc beam voltage, and (3) rf collector efficiency as

a function of rf power output. The most sensitive indicator of internal collector dynamics is item (1), current division. Item (2) essentially represents an integration of item (1) at a given beam voltage, and item (3) represents another integration, this one with respect to beam voltage, since under rf conditions a continuum of energy classes are being collected.

The interim collector was tested and evaluated on all three levels in order to provide the most meaningful evaluation possible of the computer simulation. Correlation between measured and computed results will now be discussed.

Current Distribution

The measured currents to each of the five active electrodes of the interim collector as a function of beam voltage are shown by the upper five solid curves in Figure 14. The two lower plots in the figure are the currents to the tube tunnel and to the collector housing, both electrodes being at zero potential. Also shown are dashed rectangles indicating how the current would switch from electrode to electrode under ideal conditions.

The measured curves of Figure 14 display a number of interesting characteristics. First, rather than being rectangular they exhibit a slow rise and a slow fall, displacing them appreciably to the right of the idealized rectangles. Second, preceding the onset of the main current rise, a small region is present in which the current goes negative. Third, aligned with each negative current region there is a higher-than-average current burst to the electrode immediately adjacent and lower in potential. Finally, at voltages higher than 7 kV the cup/spike current goes negative and the current to electrodes #3 and #4 exhibit marked increases. Individual measurement of the spike current shows that it is zero under practically all conditions.

Agreement between the idealized and measured current patterns shown in Figure 14 is good qualitatively, but each of the characteristics noted above causes a significant deterioration in collector efficiency, as will be shown in the final portion of this section.

The great value of the interim collector measurements is that they provide an experimental base on which a valid computer model can be established. In the computer analysis of the interim collector, 310 electron trajectories were calculated. The electron beam was divided into ten annuli, each containing one-tenth of the beam area. Representative electron trajectories were calculated beginning at the radius of gyration of each of the annuli.

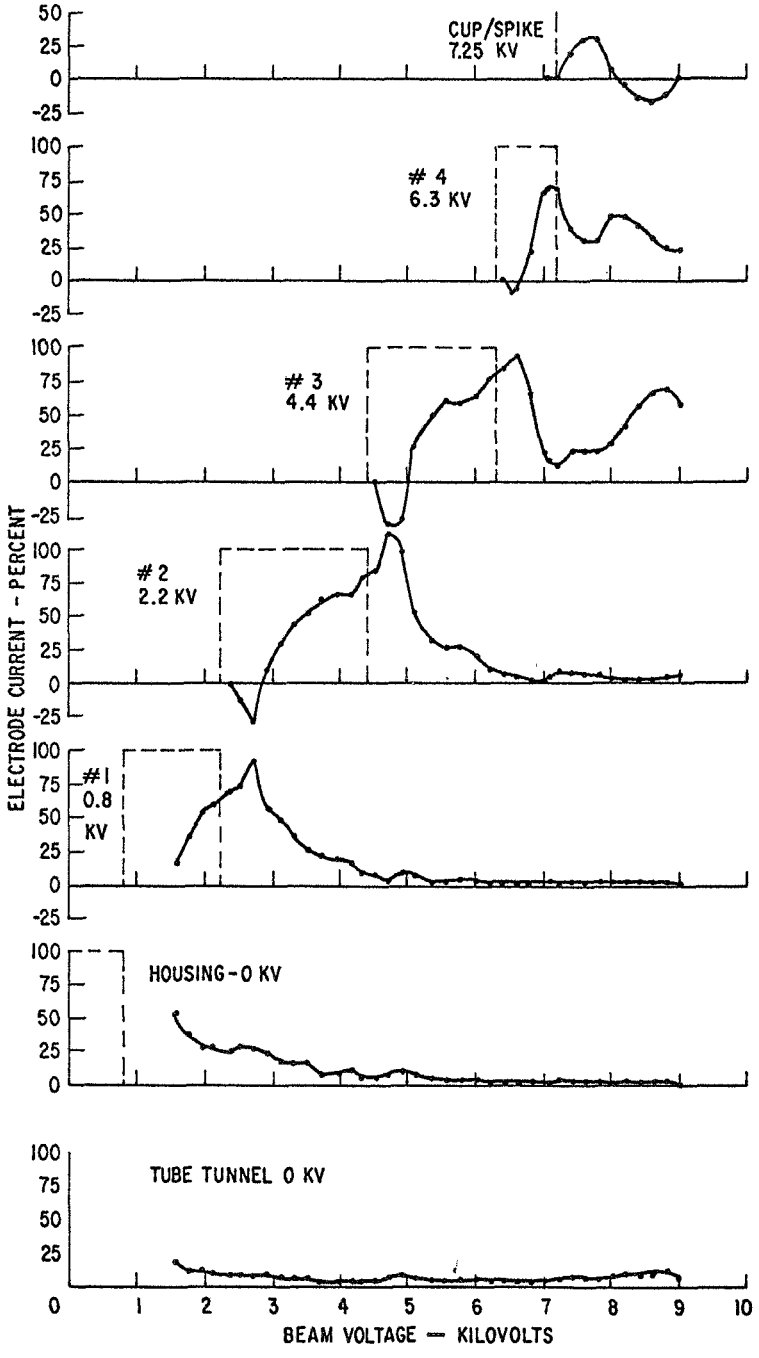

Figure 14 - Measured Current Division of Interim Collector

Thirty one trajectories were plotted for each annulus corresponding to electron energies ranging from 1000 to 7000 volts, in steps of 200 volts. The trajectories for each electron were computed until the electron reached the top or bottom surface of a collecting electrode. If the top surface was struck, the electron was assumed to contribute one unit to the current to that electrode. If the bottom surface was struck, it was assumed that a secondary could be generated with a yield of unity, in which case the current effectively flowed to the electrode at the next lower potential.

In this manner, it was possible to make a "bean count" of the current expected to each electrode, as a function of beam voltage. The computed electrode currents are shown in Figure 15; these should be compared directly with the measured currents in Figure 14. In most respects the correlation between measured and computed electrode current is striking. The basic triangular current pattern is present in both cases. Only the fine structure of dips and peaks are absent in the computed curves. The effect of secondaries appears to shift all curves slightly to the right.

The major dips and peaks in the experimental data are undoubtedly due to secondary electrons leaving the bottom surface of one electrode and arriving at the upper surface of the electrode next lower in potential. This does not show up in the computed currents because for the calculations shown in Figure 15 the secondary yield has been taken to be unity. The measured data suggest that in the vicinity of the electrode voltages the yield is considerably larger than unity since the currents actually reverse at times. This seems reasonable because just before the primary current switches to a new electrode, the electrons skim the bottom surface of the electrode with low energy and at grazing incidence, and the yield is greatly increased. The computer analysis could be refined to take this higher yield into account, but this has not been done.

Also lacking in the computed data are the pronounced peaks in #3 and #4 electrode current at energies greater than 7 kV. These peaks are thought to be due to secondaries leaving the upper flat portion of the cup. These secondaries, however, fall more than one step down in electrode potential because of the fanned-out geometry of the electrode structure. This shift of current from the final electrode to electrodes several steps down in potential appears to be the source of the single most serious loss of efficiency in the interim collector, as will be discussed later under "Final Collector".

The computed curves of Figure 15 are based on an extremely simple choice of spent beam input conditions. The spent beam is assumed to be

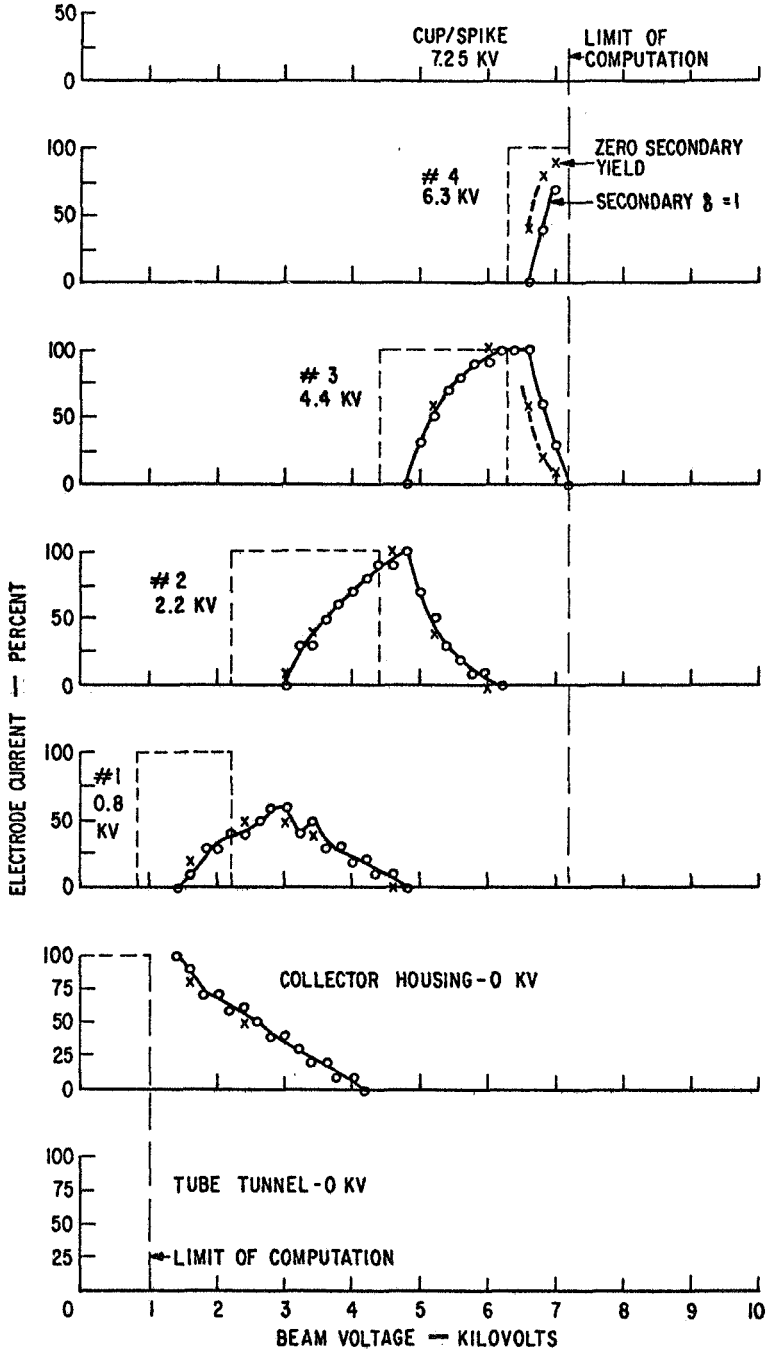

Figure 15 - Computed Current Division of Interim Collector

traveling parallel to the z-axis and its beam radius for all energy classes is assumed to be 0.6 of the wall radius midway down the taper section between the drift tube and the collector proper. The justification for this choice of input conditions is also given later under "Final Collector".

DC Collector Efficiency

The currents collected at each of the electrodes in Figure 14 may be multiplied by the electrode voltages, and the sum of these recovered powers may be used to calculate the dc collector efficiency in accordance with the equations developed previously in this report. In Figure 16, this measured collector efficiency is plotted as a function of beam voltage for two choices of electrode voltages. The two curves exhibit very similar behavior in that they both rise in a roughly linear fashion with dc beam voltage, and they both exhibit severe narrow dips of efficiency at voltages several hundred volts above the respective electrode voltages. The slow linear rise with voltage is disappointing; a higher, concave-downward curve is needed if collector efficiency is to exceed 50 percent. Furthermore, above the full beam voltage of 7 kV the collector efficiency falls rapidly. To obtain the remainder of this curve up to 14 kV, the power dissipation rating of the bleeder resistors in the electrode supply would have been exceeded. Instead, another curve was taken in which all voltages were scaled down by a factor of two, allowing the region of the dc collector efficiency curve from V_o and $2V_o$ to be completed. This curve is shown in Figure 17 as a solid line. The "design electrode voltage" curve from Figure 16 is plotted in Figure 17 as a dashed line. The agreement is quite good up to $1.3\,V_o$ lending support to the idea that above $1.3\,V_o$ the behavior of a tube with a beam voltage of 7 kV should be similar to the behavior at one-half voltage.

Collector efficiency can be computed approximately using the simple idealized model, corresponding to the dashed rectangular current shapes shown in Figures 14 and 15. When this is done, the saw-tooth shaped curve shown in Figure 17 is obtained for collector efficiency as a function of beam voltage. Above 7 kV, collector efficiency falls hyperbolically as V_o/V. This idealized curve is a very crude approximation to the measured collector efficiency shown in Figures 16 and 17. A much more accurate calculation can be made using the computed currents shown in Figure 15. If secondary electrons are ignored -- ie., bottom side hits are credited to the struck electrode -- the solid line curve in Figure 18 is obtained. If a secondary yield of unity is assumed, the collector efficiency below 7 kV drops only slightly, as shown by the dashed line in Figure 18. However,

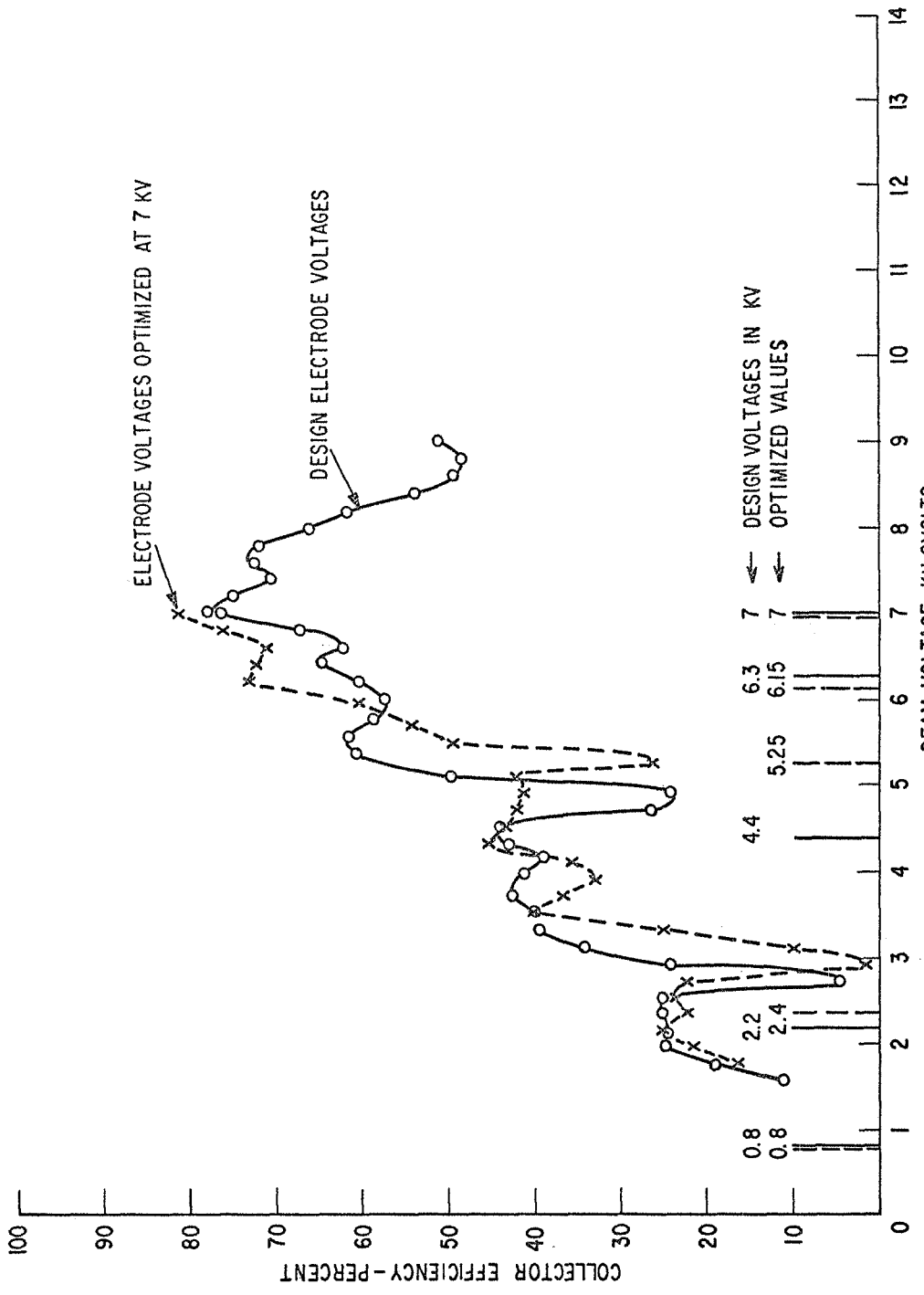

Figure 16 - Measured DC Collector Efficiency of Interim Collector

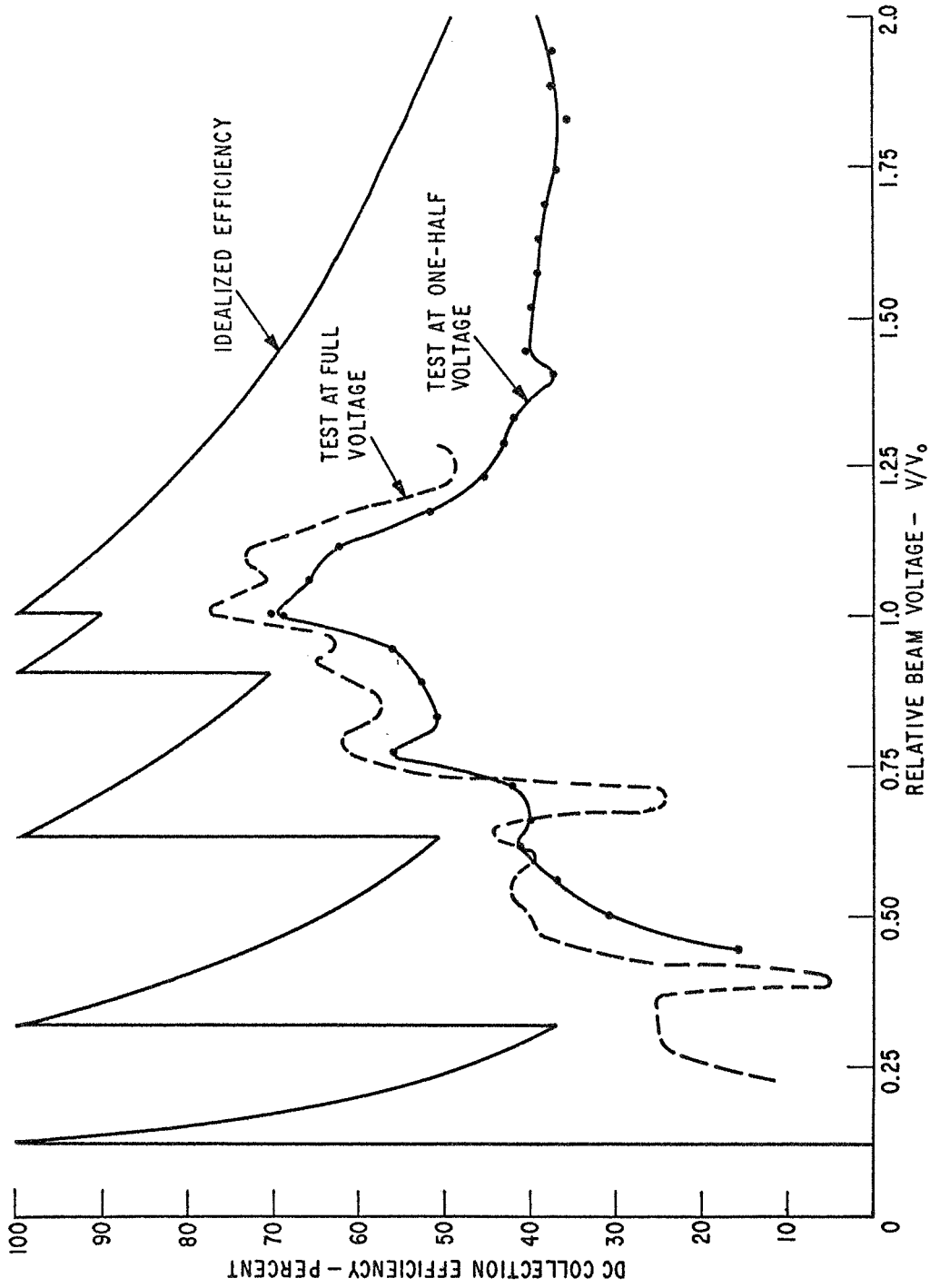

Figure 17 - DC Collector Efficiency at Reduced Voltage

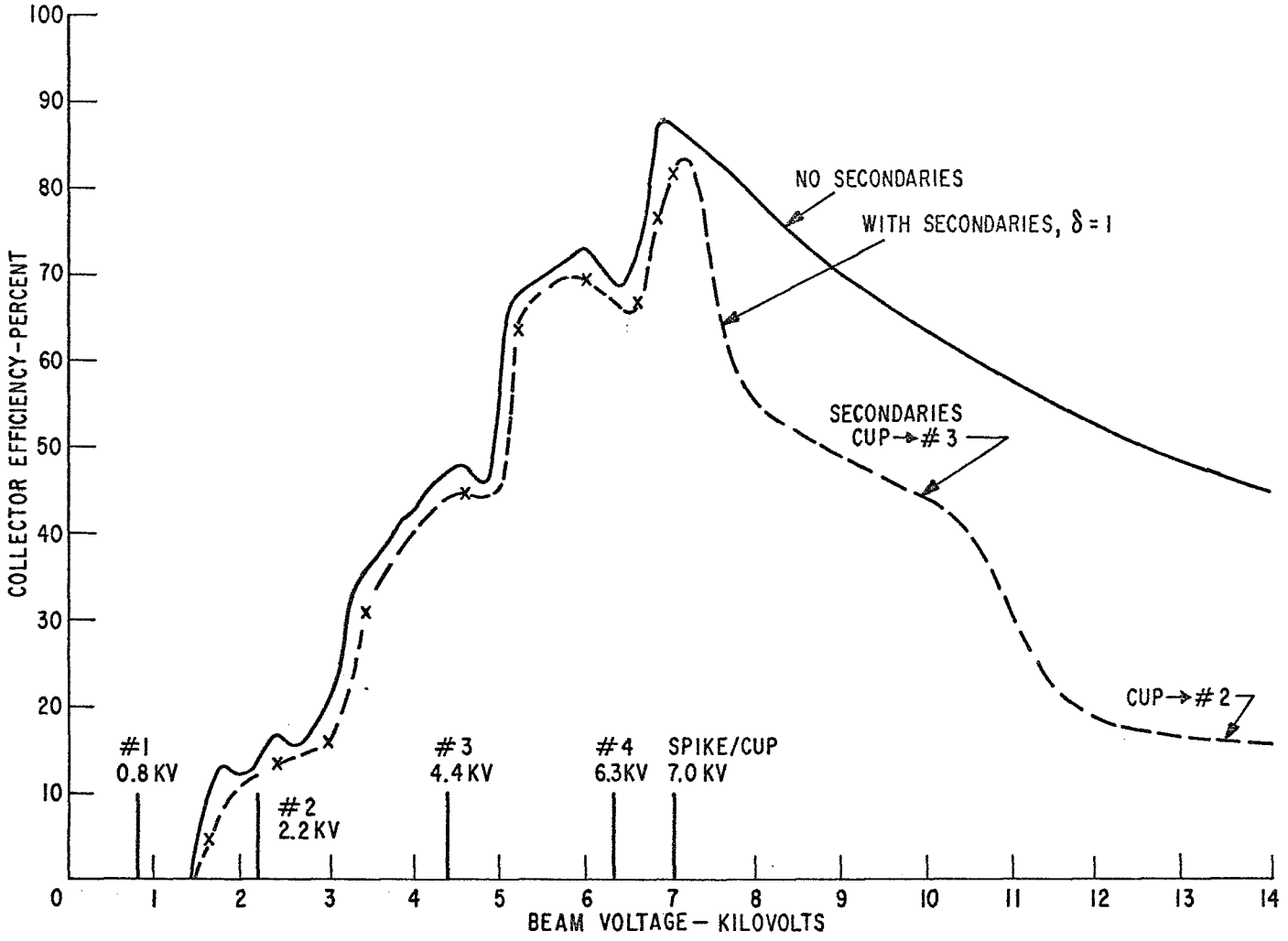

Figure 18 - Computed DC Efficiency of Interim Collector

above 7 kV the loss of secondaries, first to electrode #4, then to electrodes #3 and #2 at successively higher voltages, causes a serious loss in collector efficiency. The voltages at which switching occurs from one electrode to another were taken from the trajectory studies described previously. In the high-voltage region shown in Figure 18, the efficiency drops to the extensions of the various hyperbolic curves making up the idealized efficiency curve. The data in Figure 17, indicate that in this region the measured loss in efficiency is not as severe as predicted in Figure 18, probably due to a reduced secondary yield at the higher beam voltages. However, the high relative voltage data shown in Figure 17 were not available at the time the bulk of the calculations in this section were made. Therefore, the dashed curve in Figure 18 forms the basis for the calculation of rf collector efficiency given in the final portion of this section.

A direct comparison of the measured and computed dc collector efficiency is shown in Figure 19. The correlation is excellent in most respects. Missing in the computed curve are the "icicles" hanging down from the measured curve. These could probably be generated computationally if secondary yields in excess of unity were assumed for conditions of grazing incidence.

RF Collector Efficiency

One of the most important characteristics of a collector is its ability to recover energy under rf conditions. The measured rf collector efficiency of the interim collector as a function of rf power output is shown as a solid line in Figure 20. At zero power output the efficiency is 80 percent for this run of data, in close agreement with the figure of 78 percent at 7 kV shown in Figure 19. As the power output is increased by increasing drive power, the rf collector efficiency drops rapidly until at the full power output of 740 watts, the collector efficiency is 34 percent. This curve was taken with a constant output impedance; hence, assuming that beam loading in the output gap is negligible compared to the external loading, the output voltage swing can be assumed to be proportional to the square root of rf power output. This assumption allows computation of the rf collector efficiency by direct integration of the dc collection efficiency shown in Figure 19 from $(1-\alpha_o)V_o$ to $(1+\alpha_o)V_o$ where

$$\alpha_o = \sqrt{P_{rf}/P_{rf\text{-}max}} \tag{13}$$

This method of integration for calculating rf collector efficiency from the dc measurements is fully described in the Analytic Collector Study final report[3] prepared under Contract NAS3-11530.

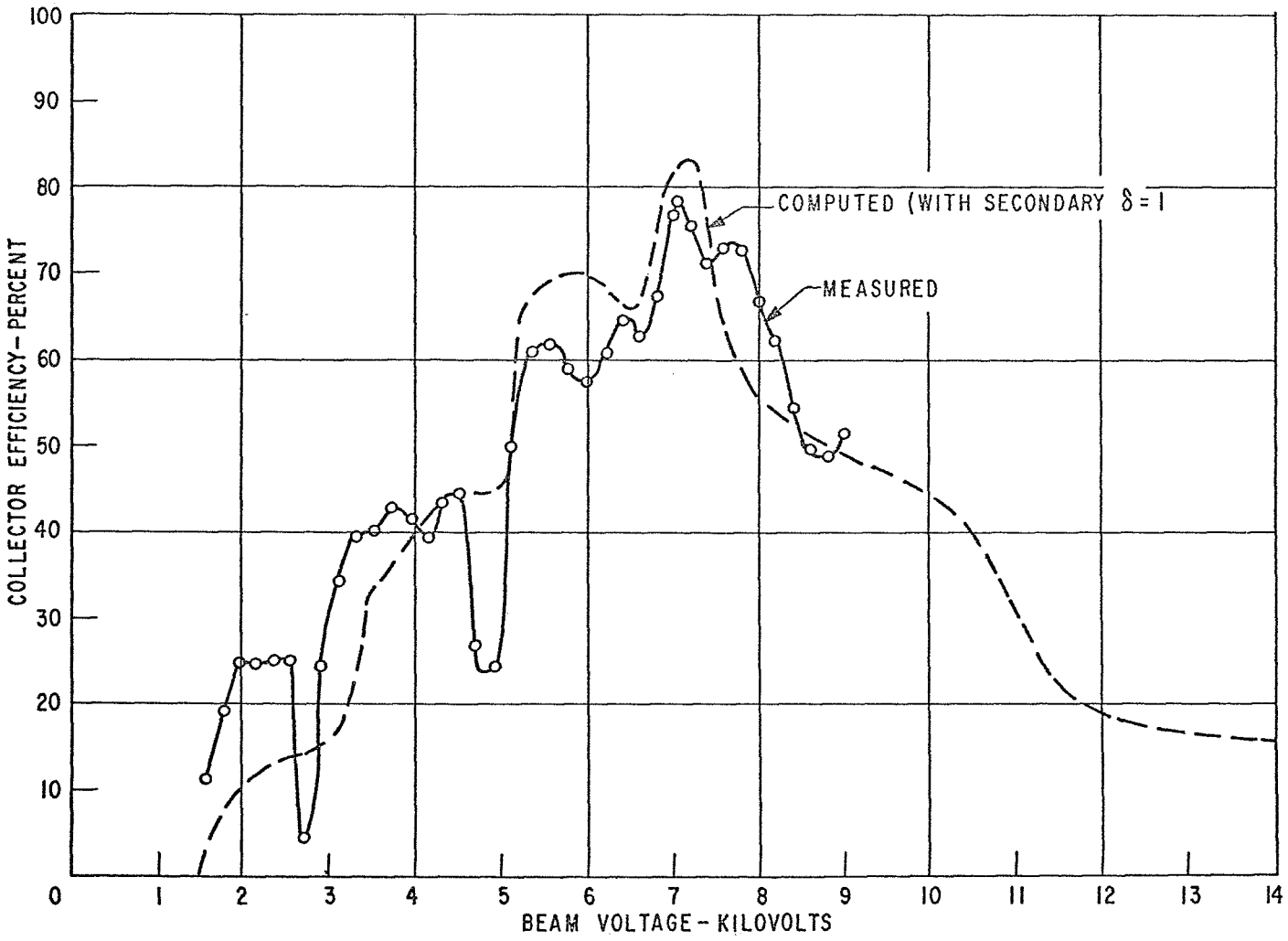

Figure 19 - Comparison of Measured and Computed DC Efficiencies of Interim Collector

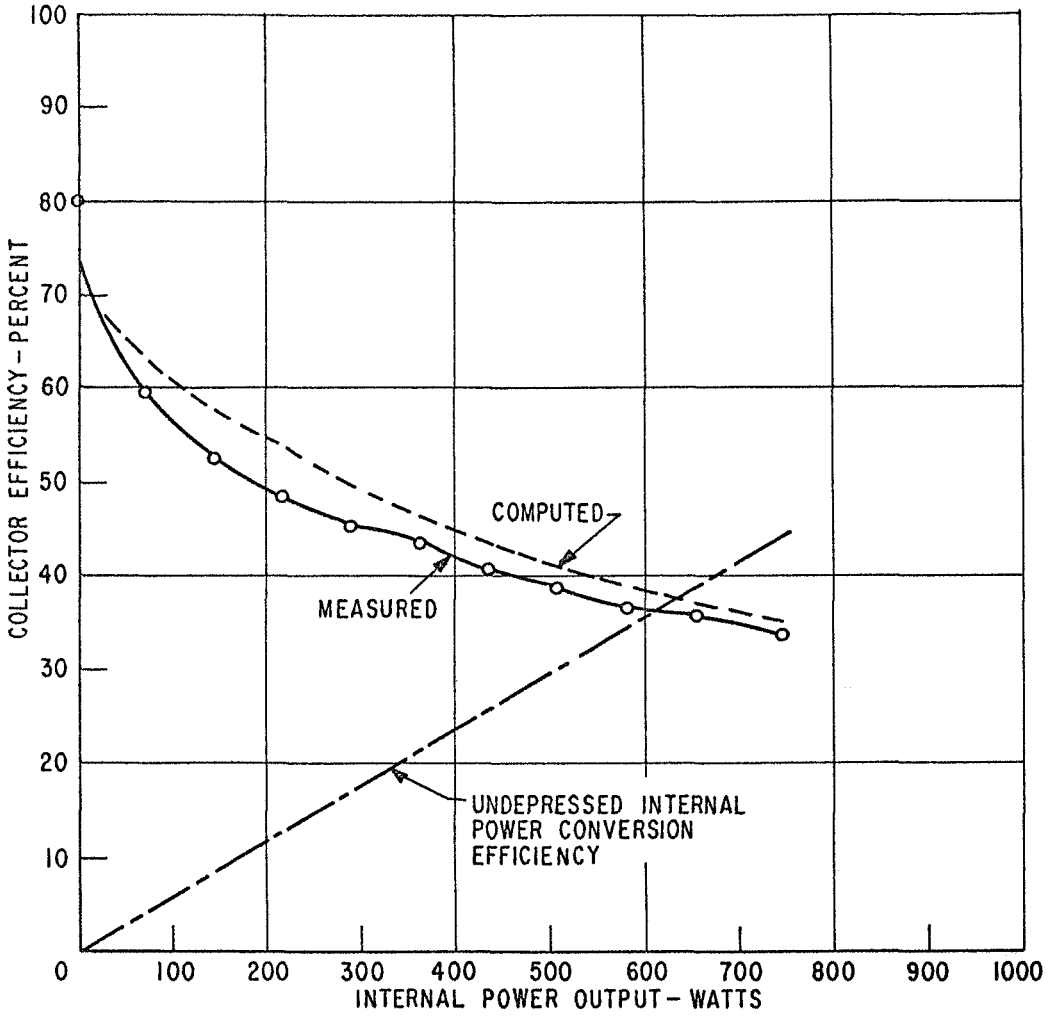

Figure 20 - Measured and Computed RF Efficiency of Interim Collector

The integration of the computed dc collection efficiency curve between these limits gives a computed curve of rf collector efficiency as a function of power output (shown in Figure 20 as a dashed line). The agreement between measured and computed collector efficiency is remarkedly close, even though under rf conditions it is likely that the electrons have somewhat different input conditions (eg., input radius, transverse velocity, etc.) than they do in the dc case. In computing rf collector efficiency from the measured current distribution, the output circuit efficiency is taken to be 85.7 percent based on the measured loaded and unloaded Q factors of 264 and 1840, respectively. The unloaded Q is low because of the external type cavity construction with numerous contact fingers and because the three bakeouts to which this tube has been subjected have left some lossy film deposits on the ceramic cylinders. The rf power output is taken to be the power generated at the output gap. On the basis of the success in using the dc characteristic to predict the rf efficiency it would appear that the major characteristics of the input conditions are caused by effects which are common to both the dc and rf measurements, such as transverse velocities due to the magnetic field, rather than effects unique to the rf interaction such as transverse rf fields in the output gap.

One discrepancy evident from Figure 20 is the wider spacing of the curves at a power output of 200 watts, and the gradually narrower spacing as saturation power output is reached. The main source of this discrepancy is the absence of the "icicles" in the computed curve of Figure 19. On the other hand, as saturation power is approached, the computed curve is falling faster than the measured curve. This suggests that the extremes of the computed collector efficiency curve, near 1 kV and near 13 kV in Figure 19, are too low. The upper extreme is probably pessimistic because the secondary yield should drop below unity for directly incident electrons with several kilovolts of energy, as suggested by Figure 17. The lower extreme of the computed efficiency curve in Figure 19 is also too low, but this is due to another reason: probably that the input conditions at the entrance plane to the collector are not constant for all energy classes, as was assumed in the calculation. The low end discrepancy in Figure 19 suggests that either the beam is larger in diameter than was assumed, or that transverse velocities were becoming of importance -- or most likely, a combination of both effects. This suggests that, if possible, a more accurate set of input conditions should be chosen for future computations. An attempt to do this is described in the next section, but surprisingly enough the agreement between measured and computed dc collector efficiency became worse, not better. Therefore, the simple input conditions described earlier for the interim collector computations were retained in the design of the final collector.

A final comparison of rf collector efficiency is shown in Figure 21. In this case the computed curve is based on an integration of the measured dc collection efficiency in Figure 19. The agreement between the two curves is slightly closer than in Figure 20, particularly at the first two measured points. At higher rf output power, the upward output voltage swing exceeds 10 kV. As is evident from Figure 19, no measured data are available for the dc collector efficiency above 9 kV; therefore, at higher drive levels the integration has been carried out using the computed dashed curve of Figure 19 to augment the measured dc curve from 1 to 9 kV. Thus, strictly speaking, Figure 21 is based on a combination of a measured and a computed dc collector efficiency characteristic.

The close correlation between measured and computed interim collector performance discussed in this section gives confidence in the analytical design procedures. The importance of secondary electron suppression is clearly brought out by the discrepancies between theory and experiment, particularly at high beam voltages. Therefore, in the final collector design the effects of secondaries were reduced by modifying the electrode placement to discourage grazing incidence, and by use of a suppressor grid in front of the final cup electrode. In the next section a number of alternative designs are discussed and evaluated, and the final choice of collector design is established.

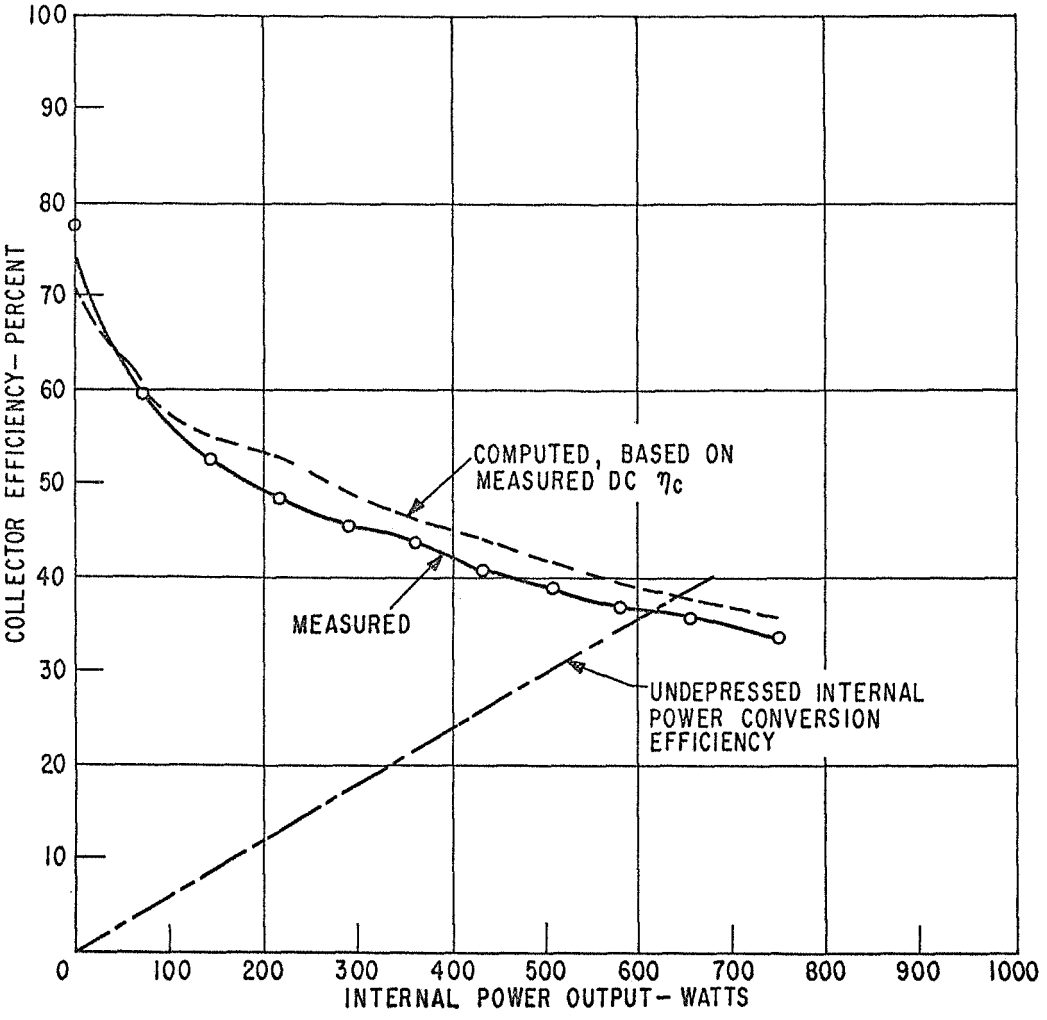

Figure 21 - Measured and Computed RF Efficiency of Interim Collector, Using Measured DC Efficiency Curve

FINAL COLLECTOR

ANALOG COMPUTER STUDIES

The validity of the analog computer program for collector design was established by the close correlation obtained between computed and measured results for the interim collector. The rf collector efficiency of the interim collector was considered too low for practical use, however, and in this section, several methods of increasing collector efficiency are described. These are: (1) increasing the number of electrodes in the interim collector, (2) using a spike, along which a gradient of potential can be established to improve electron sorting, and (3) a combination of increasing the electrode number, modifying the electrode edge locus, and using a suppressor grid.

Analysis shows that a simple increase in electrode number in the interim collector will not increase collector efficiency enough to be interesting. The graded-spike approach leads to excellent collector efficiency, but requires the use of a stable high-resistance film. It was felt that the development of a reliable technique for achieving this film would require more time than was available. The ultimate choice of design for the final collector was a straightforward improvement of the interim design; the only new technique needed for this approach was the development of a relatively coarse grid to suppress secondaries from the highest potential electrode.

Collector with Increased Number of Electrodes

The simplest way of improving collector efficiency would appear to be to increase the number of collecting electrodes in the interim collector from five to ten, or perhaps twenty. However, this approach is found to lead to a disappointingly small improvement in efficiency.

The electron trajectories that were calculated previously for the evaluation of the five-electrode collector can be used here to calculate the collector efficiency of a collector with an infinite number of electrodes. This is done by drawing a line through the leading edges of the five electrodes and determining the energy of each of ten ring-model electrons as it crosses this line. This was done for the interim collector at each of the thirty-one beam energies ranging from 1 kV to 7 kV. The dc collector efficiency for $N = \infty$ as a function of beam voltage, obtained in this manner, is plotted in Figure 22. The previously calculated curve for the interim collector ($N = 5$), taken from Figure 18, is also shown for reference as a dashed line. It is evident from

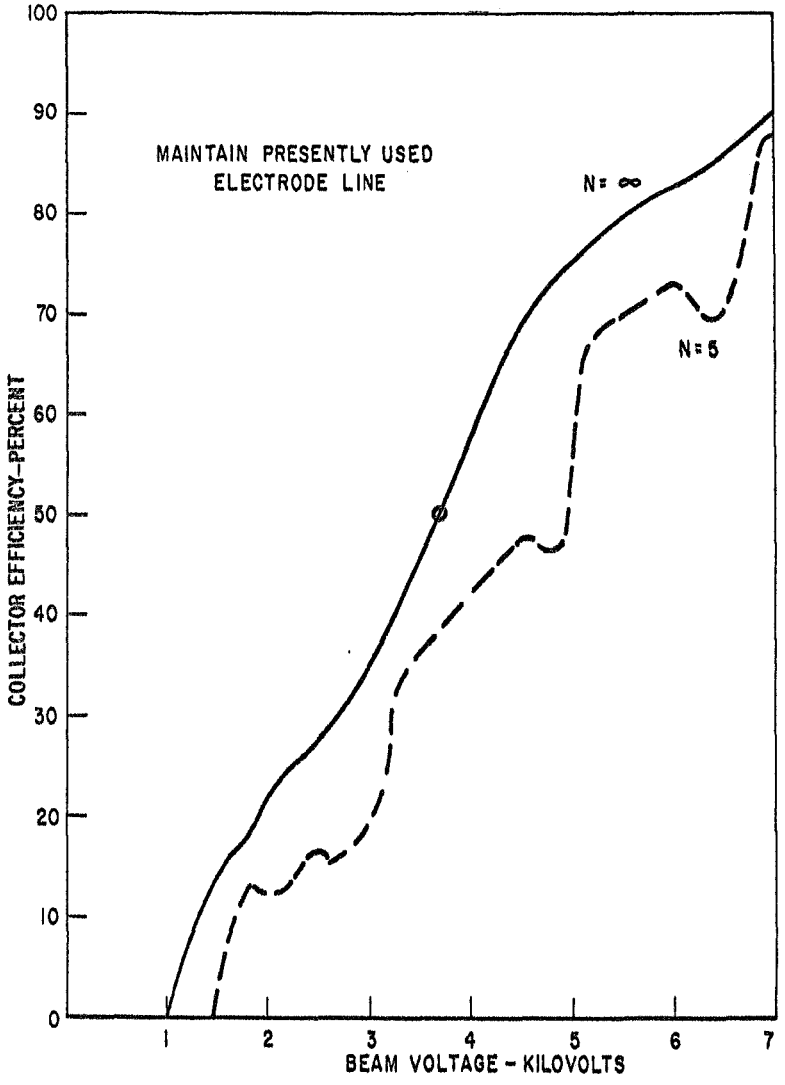

Figure 22 - Effect of Electrode Number on Performance of Interim Collector

the area under these curves that the use of even an infinite number of electrodes will not increase rf collector efficiency above 50 percent.

Thus the simple expedient of merely increasing the number of electrodes in the interim collector is not sufficient to improve the efficiency of the collector to a useful level.

Graded Spike Collector

One of the reasons for degradation in the performance of a depressed collector can be traced to the non-uniform dispersion of electrons originating at different radii, as was seen in Figure 11. The trajectories of the $0.2\,V_o$ electrons are seen to have different dispersion patterns, depending on the radius. In particular, the innermost electron shown is not deflected very well. One way of avoiding this problem is to establish a potential gradation on the axis which will deflect the innermost electrons more than those at larger radii. Figure 23 depicts a set of equipotential lines possessing this property. It can be seen that all the contours form a cusp on the axis. This cusp is produced by enforcing a potential gradient on the axis. Typical trajectories having parallel entry into this field are shown in Figure 24, where the much more uniform focusing may be seen. For any given energy class the electrons come to a reasonably well-defined focus very close to their optimum point of collection.

An analog computer calculation of the performance of a graded spike collector was made using 310 trajectories similar to the calculations on the interim collector. Thirty one energy classes originating at ten different radii form the basis of the results given in Figure 25, where the dc collector efficiency is shown for different numbers of electrodes and the two electrode lines of Figure 23. An electrode line is defined here as the line connecting the leading edge of all the electrodes. The electrodes themselves are, of course, chosen to lie along the equipotential lines of Figure 23 such that the trajectories are essentially independent of the number of electrodes. For both electrode lines the dc collector efficiency is seen to be substantially better than that associated with the interim collector (cf. Figure 18).

If a V_o/V upper half is assumed for the curves in Figure 25 then the rf collector efficiency can be computed as a function of output power by means of the integration method described earlier with the interim collector. The results of this integration are given in Figure 26 for both electrode lines and ten stages of depression. For comparison the computed interim collector performance is also shown. Again it may be observed that the graded spike collector offers a substantial improvement over the interim collector.

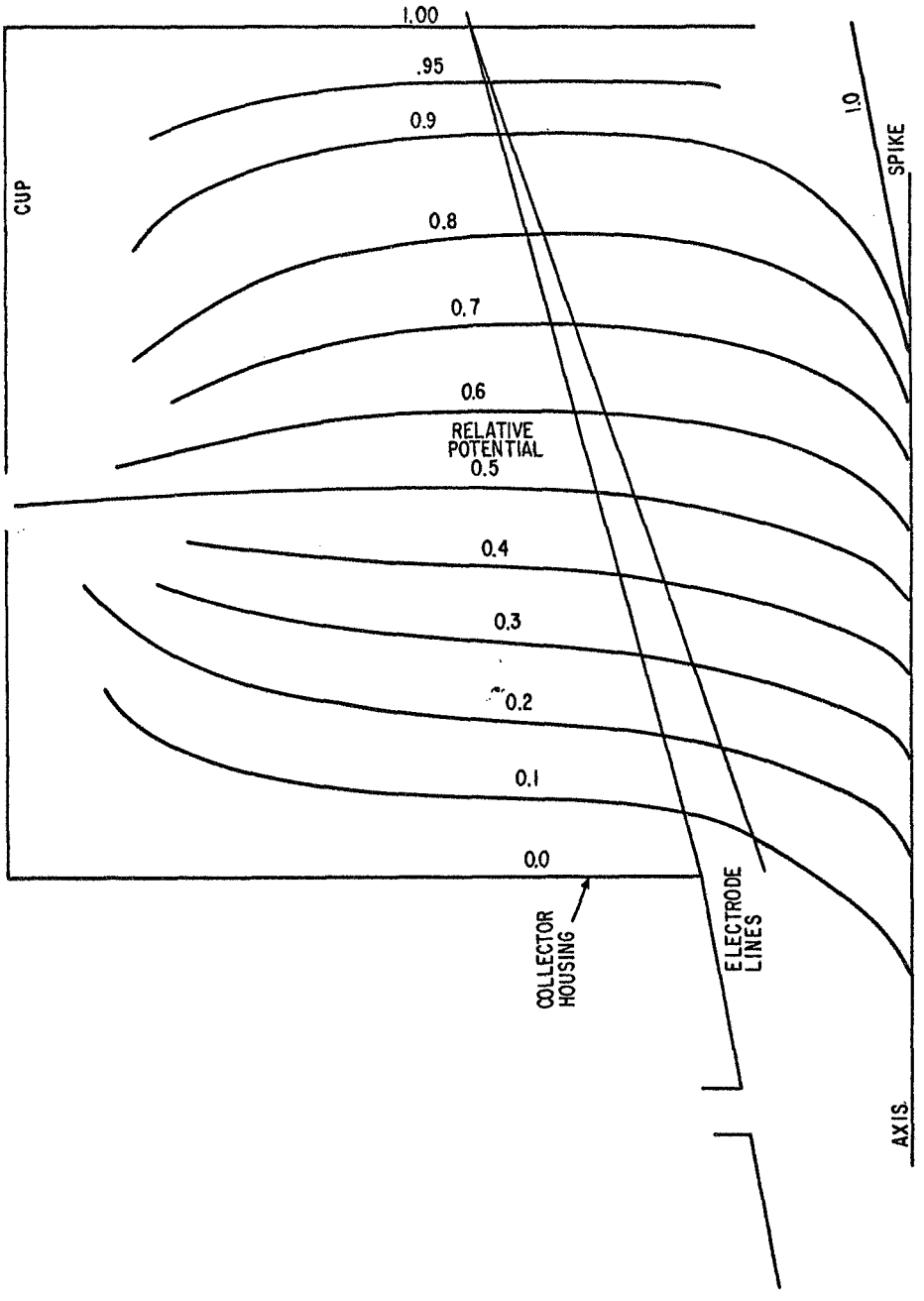

Figure 23 - Equipotential Contours of Graded Spike Collector

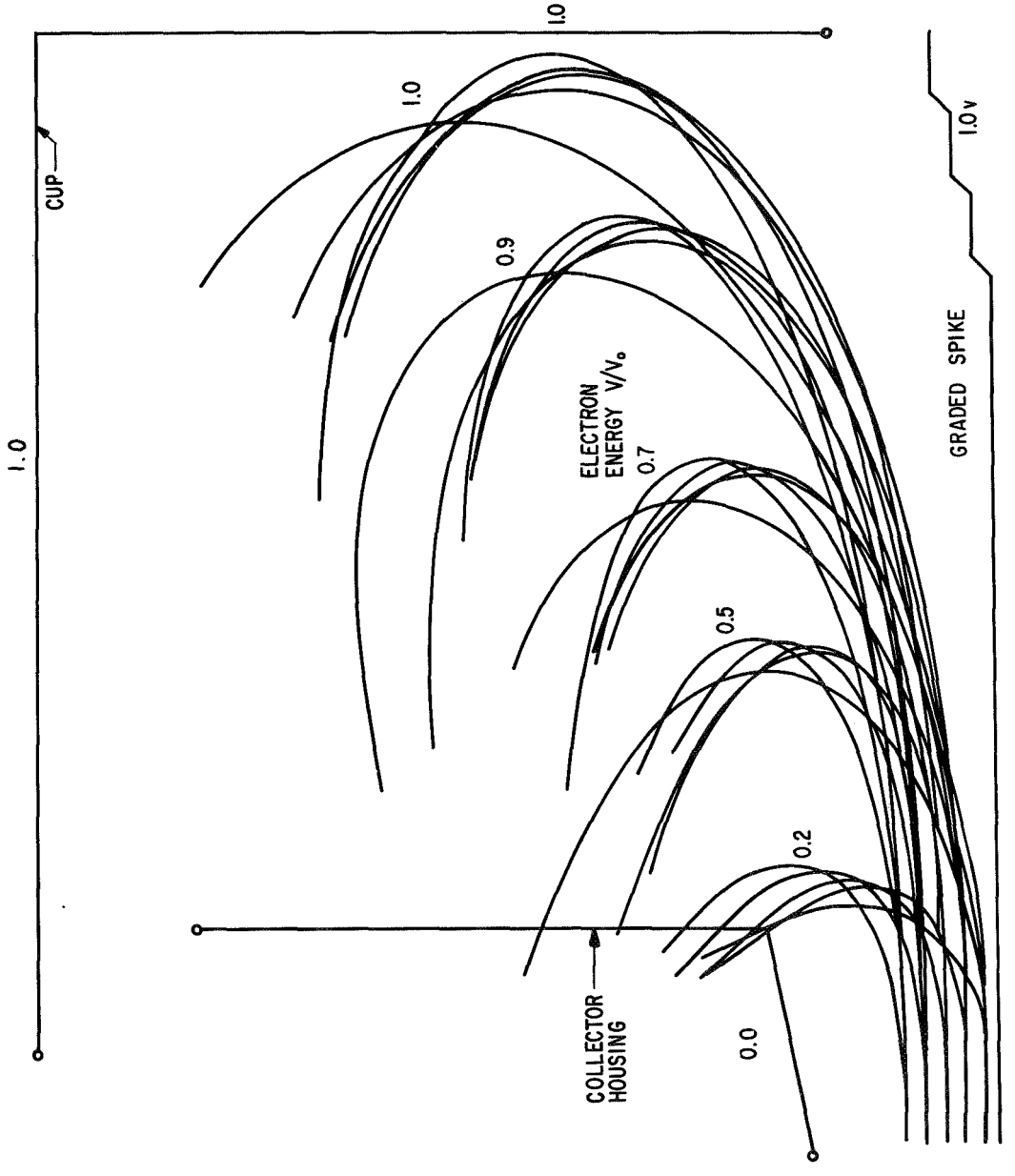

Figure 24 - Graded Spike Collector Trajectories

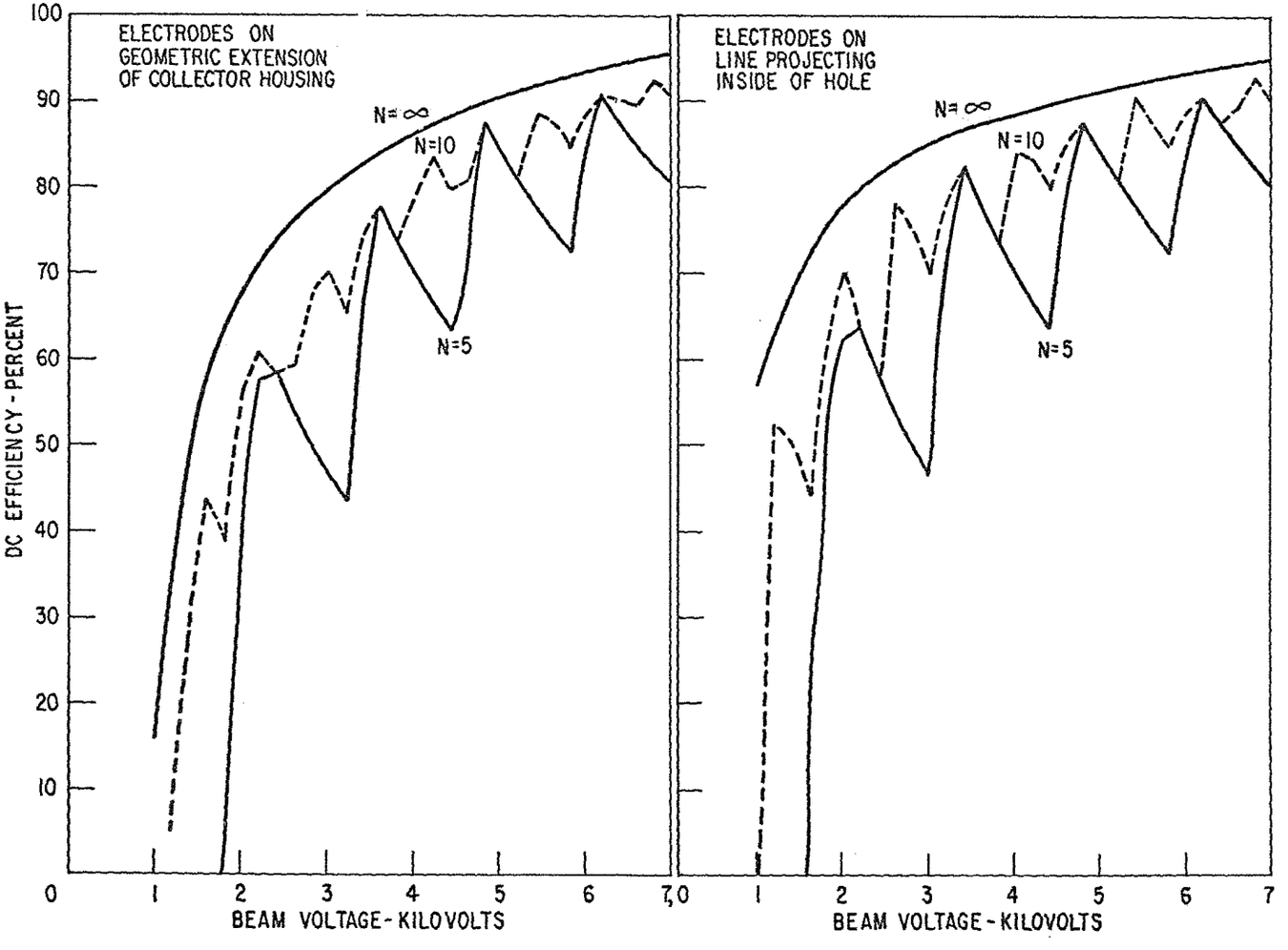

Figure 25 - Computed DC Efficiency of Graded Spike Collector

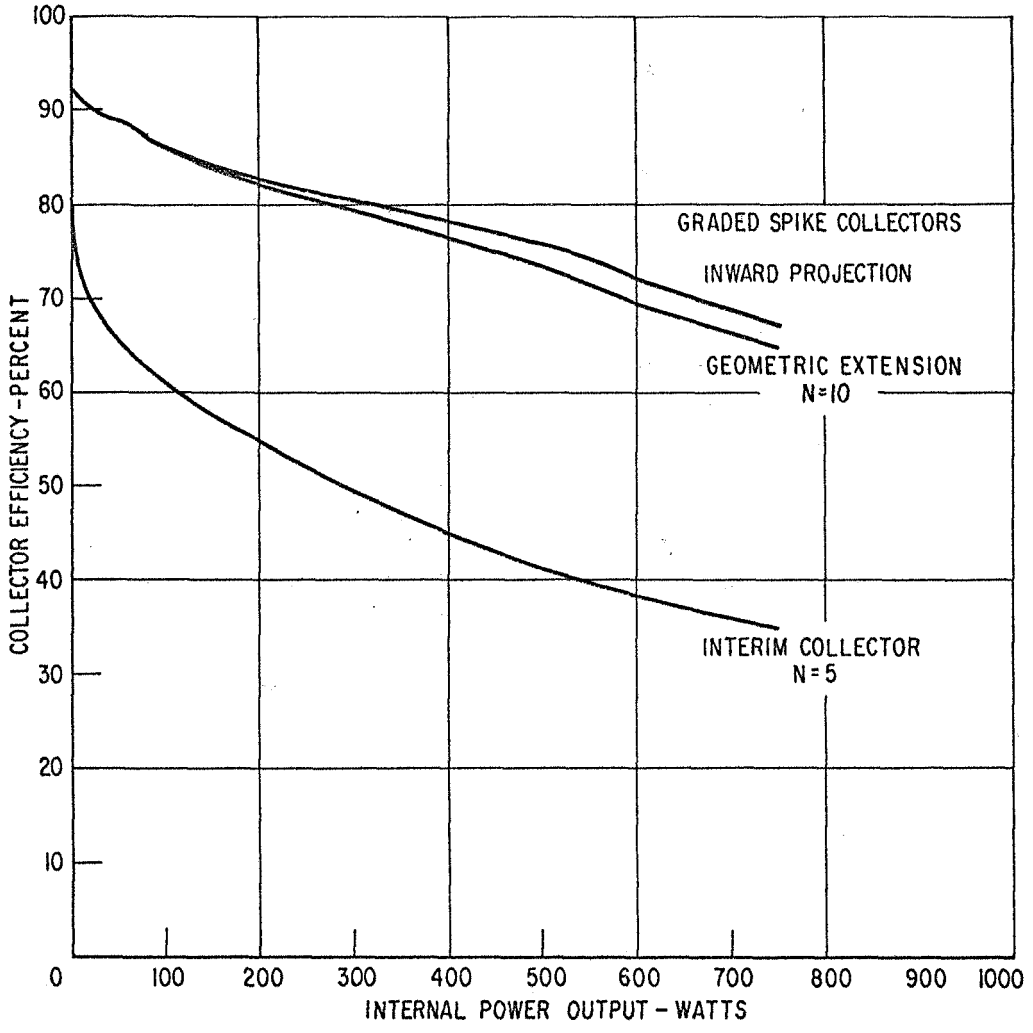

Figure 26 - Computed RF Efficiency of Graded Spike Collector

Relative to graded spike construction, the physical problem of establishing a given potential gradient along the axis of the collector was studied rather carefully and found to be quite formidable. First, the graded electrode must be thin when compared with the electron beam, yet it must also be able to withstand full beam voltage without breakdown. Secondly, if the gradient is established by a resistive film, the losses in this film must be small in order to prevent overheating of the spike and a degradation in efficiency. To meet these requirements, the film must have a resistance in excess of 10 megohms but not more than 100 megohms. The upper limit on the resistance is dictated by the intercepted current on the spike, which should not change the potential gradient.

Several bell jar tests were initiated on a structure similar to that shown in Figure 27. A resistive helix of chromium and silicon was sputtered onto a ceramic tubing by wrapping the tubing first with a tungsten ribbon and then subjecting it to the sputtering process. Films of nickel and chromium were also tried. When these resistive helices were tested at high voltage in a bell jar, they invariably exhibited a very large negative resistivity coefficient. Thus, as the helix temperature increased, the resistance would decrease, and the power input would increase because the total helix voltage was constant. This increasing power further raised the temperature and resulted in thermal runaway. This problem could be avoided by adequate cooling of the resistive spike as was shown by operating the helix stably at full voltage over long periods of time in air. Voltage breakdown did not seem to be a problem at 7 kV distributed over four inches of the helix.

Because of limitations imposed by the scope of the program, and the difficulty of solving the thermal runaway problem quickly, it was decided that a more conservative collector design should be pursued. A straightforward improvement of the interim collector with regard to both electrode number and electrode line location was shown to have an efficiency almost as good as that of a graded spike collector, as will be described next. Work on the graded spike was therefore discontinued.

Input Model for Final Collector Design

Trajectory studies for the graded spike collector showed that collector efficiency could be improved by using an electrode edge locus that projected slightly inside the diameter of the hole at the end of the taper between tube and collector (see Figure 23). However, the validity of this suggested improvement depends to a very great measure upon the choice of initial conditions assumed for the electrons at the collector input. The original choice

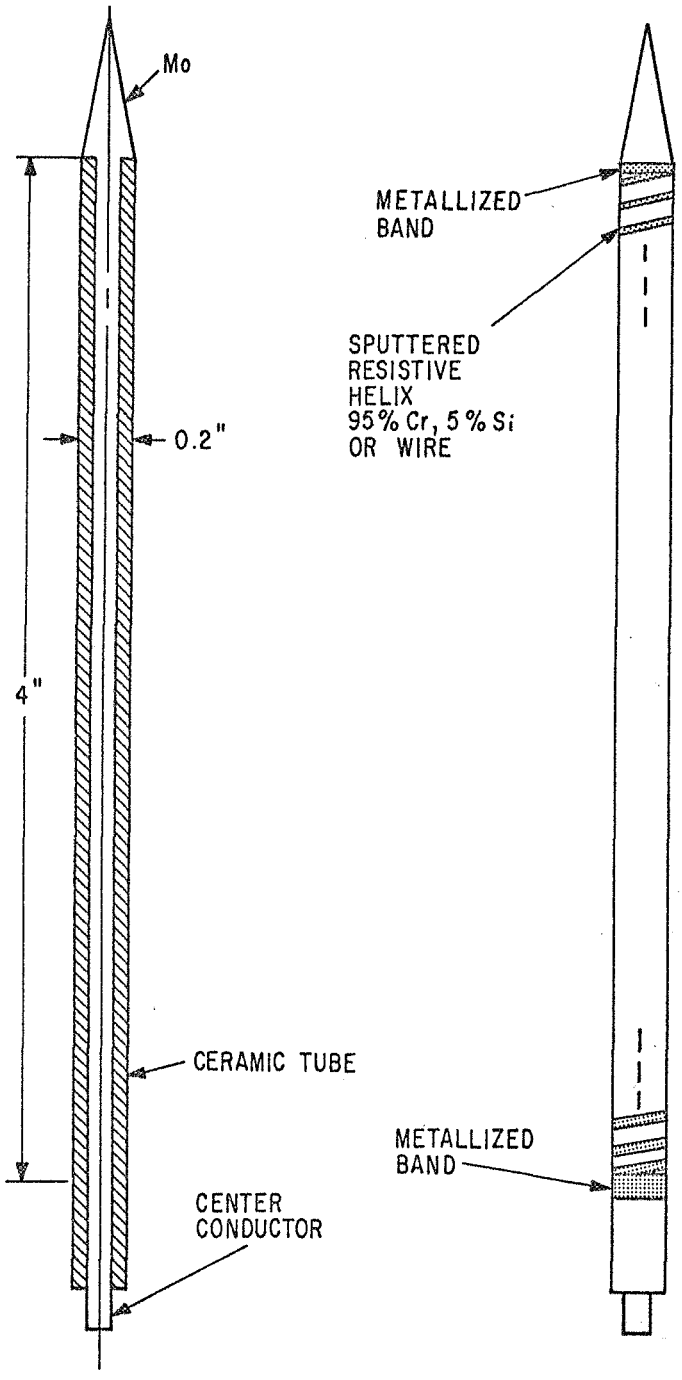

Figure 27 - Graded Spike Construction

of input conditions -- parallel flow, constant-diameter for all energy classes, half-filling the tapered drift tube at a point midway down the taper -- had been made primarily for convenience and expedience. At this stage in the collector evaluation it was felt that a more realistic set of input conditions should be used. It seemed reasonable that the electrons should be given some transverse velocity at the input plane. A schedule of transverse velocities and input radii was devised to simulate a point source for all electrons originating near the beginning of the taper. Three radial locations were established for each energy class, and an angle of injection was chosen such that the absolute transverse energy was independent of input energy. These conditions were applied at the midplane of the taper section. A list of relative radii and injection angles as a function of relative input energy is given in Table II. Ten energy input classes were chosen, and thirty electron trajectories were calculated for each collector configuration.

To test the validity of the spreading point source model, this model was used to calculate the efficiency of the interim collector as it was originally designed. Surprisingly enough, the use of this seemingly more accurate model leads to poorer agreement with experiment than is obtained using the simple parallel flow, constant beam diameter model. The comparison with measured collector efficiency is shown in Figure 28. In the upper plot the dashed curve, computed using the spreading-point source model, lies considerably higher than the measured curve, shown as a solid line. The lower dashed line plot, in which a parallel flow source was used for computations, is in much better agreement with the measured result.

Thus, while the spreading-point source model is intuitively more appealing as a description of the input condition of the spent beam, its application leads to considerably more deviation from the measured efficiency than is obtained with the parallel source model. Undoubtedly, the parameters used for the spreading-point source model could be altered from those shown in Table II to allow for less spreading, and in this way agreement with experiment could be improved. Because of the limitations of time, however, it was decided to calculate trajectories using both models, and then to choose an electrode edge locus which was a compromise between those suggested by the two models.

Final Collector Design

The low efficiency of the interim collector can be best understood by considering two regions separately: (1) the region from zero to 7 kV, and (2) the region from 7 to 14 kV. From Figure 18, it is evident that the area

TABLE II - BEAM ENTRANCE CONDITIONS

Relative Voltage	Beam Filling	Angle (Deg)
.1	.821	22.1
.1	.636	17.5
.1	.367	10.3
.2	.554	15.3
.2	.429	12.0
.2	.248	7.0
.3	.446	12.4
.3	.346	9.7
.3	.199	5.6
.4	.384	10.7
.4	.296	8.4
.4	.172	4.8
.5	.341	9.6
.5	.265	7.5
.5	.153	4.3
.6	.311	8.7
.6	.241	6.8
.6	.139	3.9
.7	.287	8.1
.7	.222	6.3
.7	.128	3.6
.8	.268	7.6
.8	.208	5.9
.8	.120	3.4
.9	.253	7.1
.9	.195	5.5
.9	.113	3.2
1.0	.239	6.8
1.0	.186	5.2
1.0	.107	3.0

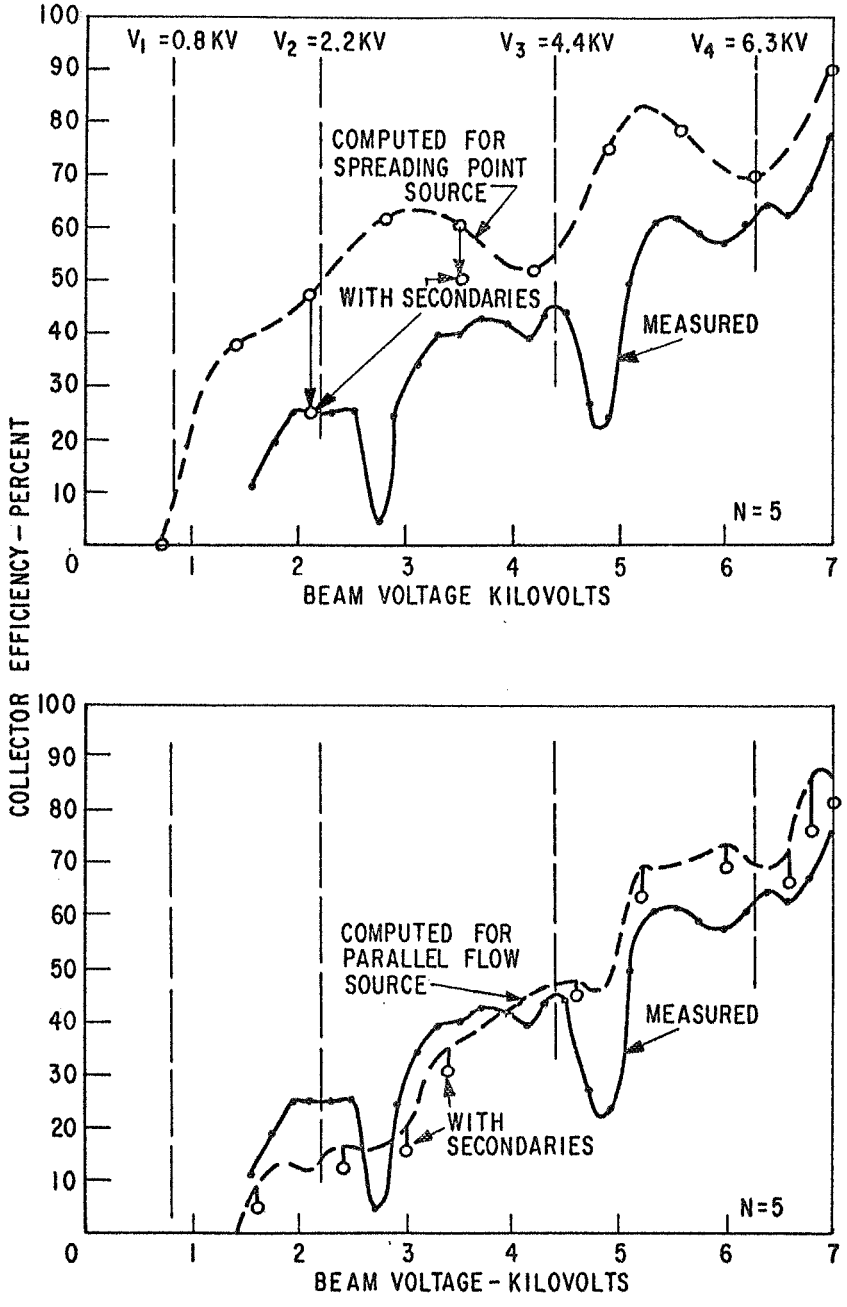

Figure 28 - Interim DC Collector Efficiency as a Function of Beam Voltage for Spreading Point Source and Parallel Flow Source

under the upper half of the dashed curve is considerably less than 50 percent of the available area. The dashed curve falls below the upper solid curve in this region due to secondary emission from the 7-kV cup electrode. It is evident from the solid line curve in this figure that if secondary emission could be suppressed, the area under the upper half of the curve would rise from less than 50 percent to the vicinity of 70 percent. This suppression can be achieved by installing a coarse suppressor grid in front of the final cup electrode and biasing it so as to return secondaries to the cup. Calculations indicate that if suppression of cup secondaries is achieved, the full swing rf collector efficiency of the five-stage interim collector would rise from 35 to over 50 percent.

A second source of efficiency improvement over the interim collector can be obtained by reducing the size of the apertures in the collector electrodes, thus bringing the electrode edge locus closer to the axis. In the final collector, the low energy electrodes are designed to actually project within the hole diameter of the taper that leads into the collector. Figure 29 depicts the electrode shapes and locations used in the final collector. Ten electrodes were used for the final design rather than five electrodes because it was believed that the improvement in other aspects of the collector design justified the extra refinement in sorting obtained by increasing the number of electrodes.

The electron trajectories using the parallel flow input conditions are also shown in Figure 29. A similar set of trajectories is shown in Figure 30 under spreading-point source input conditions. The final electrode edge locus was chosen as a compromise between the optimum edge loci associated with each input source model. It is not surprising, therefore, that the computed collector efficiency given by the two models is in close agreement in this case, as is shown in Figure 31. The computed points using the parallel source model are indicated by the circles in this figure; the computed points using the spreading point source model are indicated by crosses. The final computed collector efficiency was obtained by using the solid line, which is a compromise between the two sets of computed points. The portion of the curve between 7 and 14 kV in Figure 31 is simply a plot of V_o/V, which should be a fairly good measure of collector efficiency if secondaries are successfully suppressed by a grid located in front of the final cup electrode.

The computed dc collector efficiency shown in Figure 31 can be integrated to establish rf collector efficiency, as shown in the upper curve of Figure 32. An efficiency of 44 percent was taken to correspond to a relative rf voltage swing of unity in the output gap for this calculation. This correspondence was chosen because in the interim collector the maximum internal

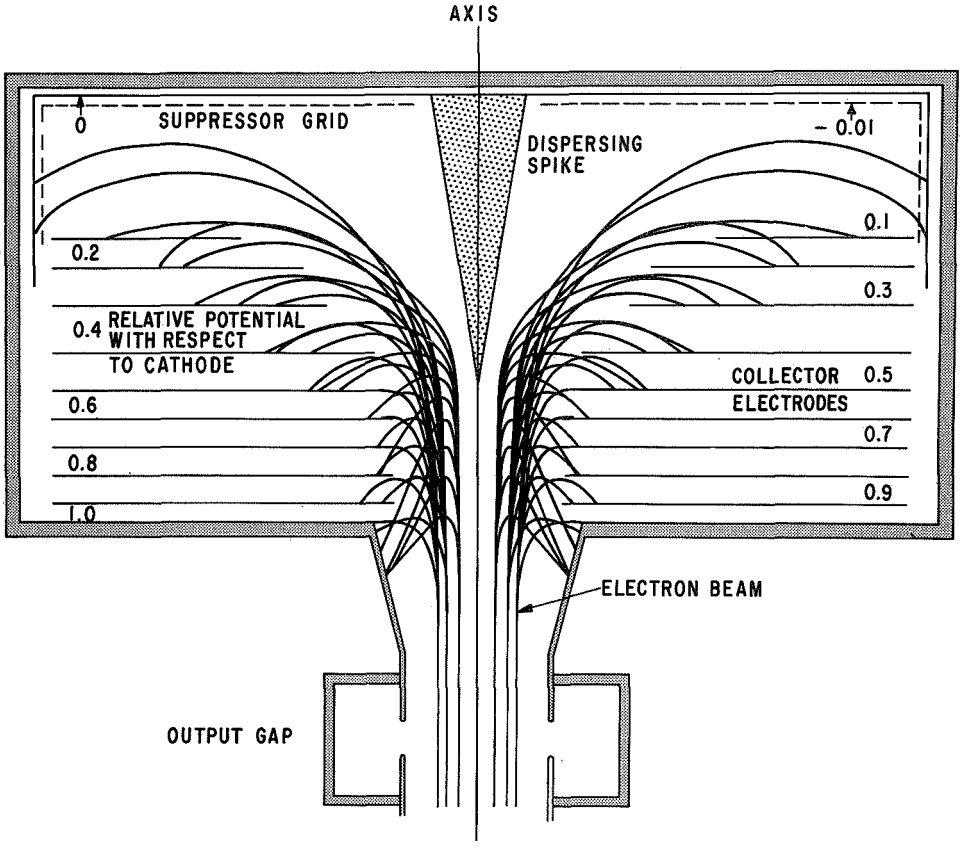

Figure 29 - Electron Trajectories in the Final Collector, Starting with Parallel Flow

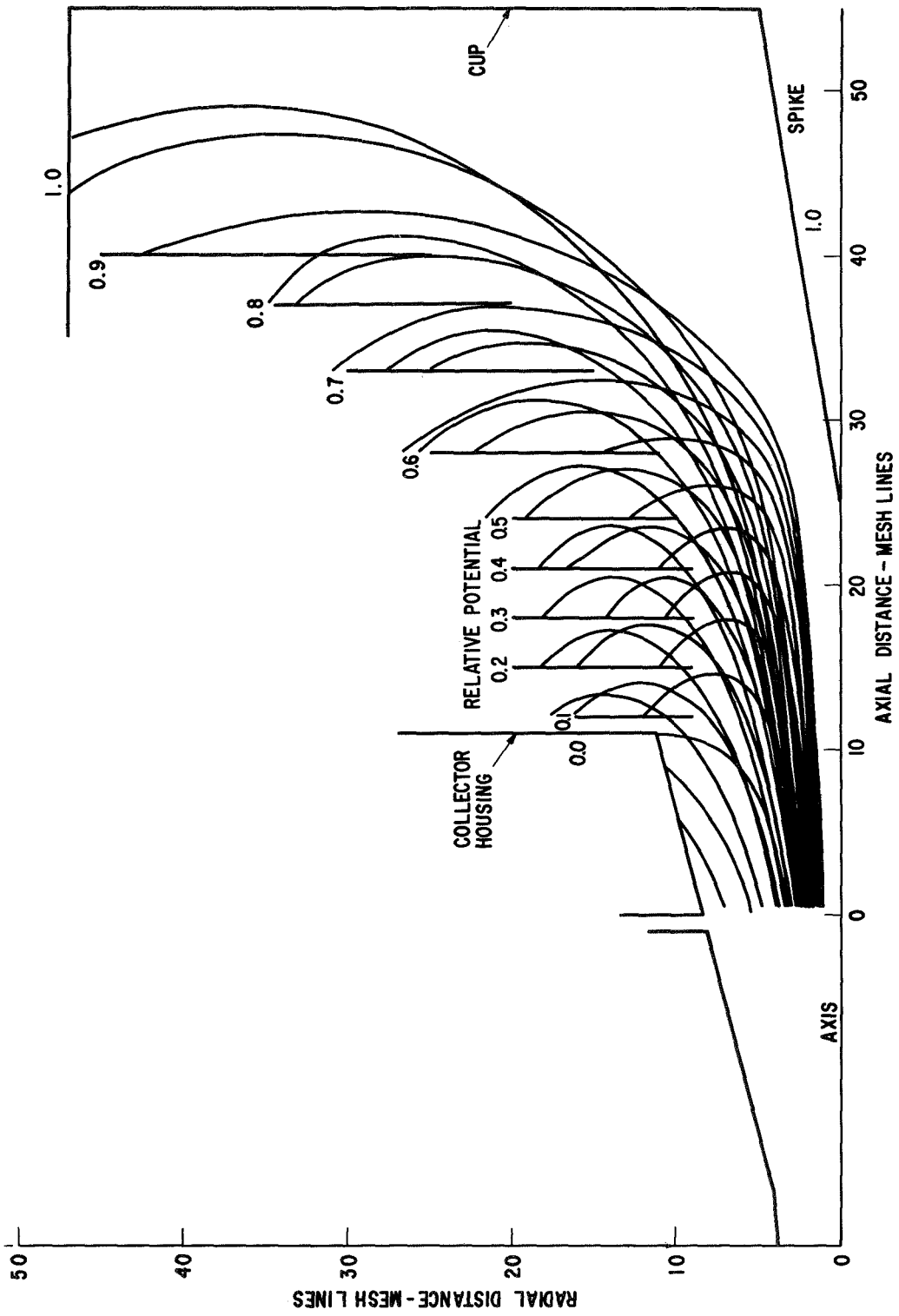

Figure 30 - Final Collector Trajectories Starting from a Point Source

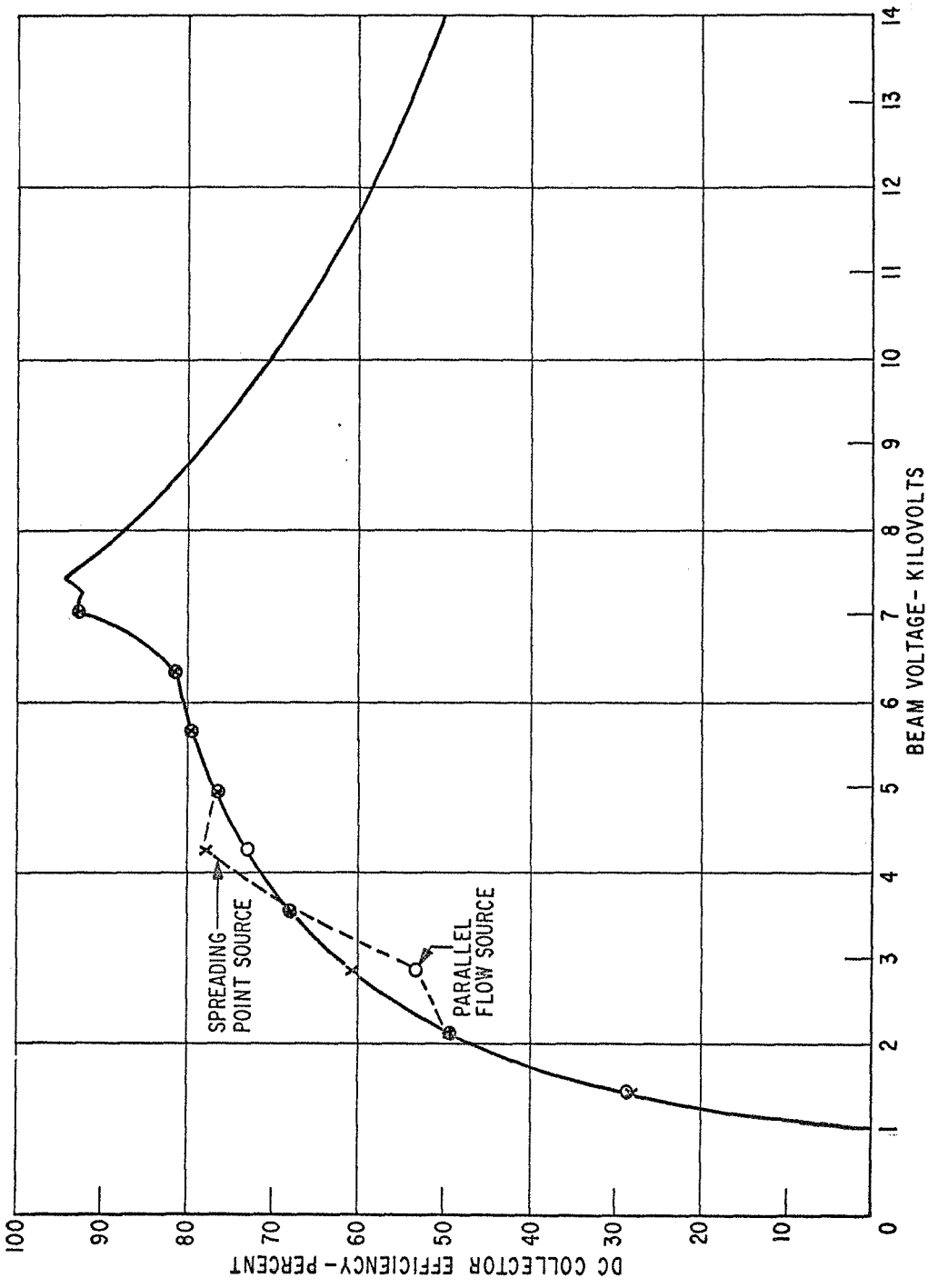

Figure 31 - Computed DC Efficiency of Final Collector

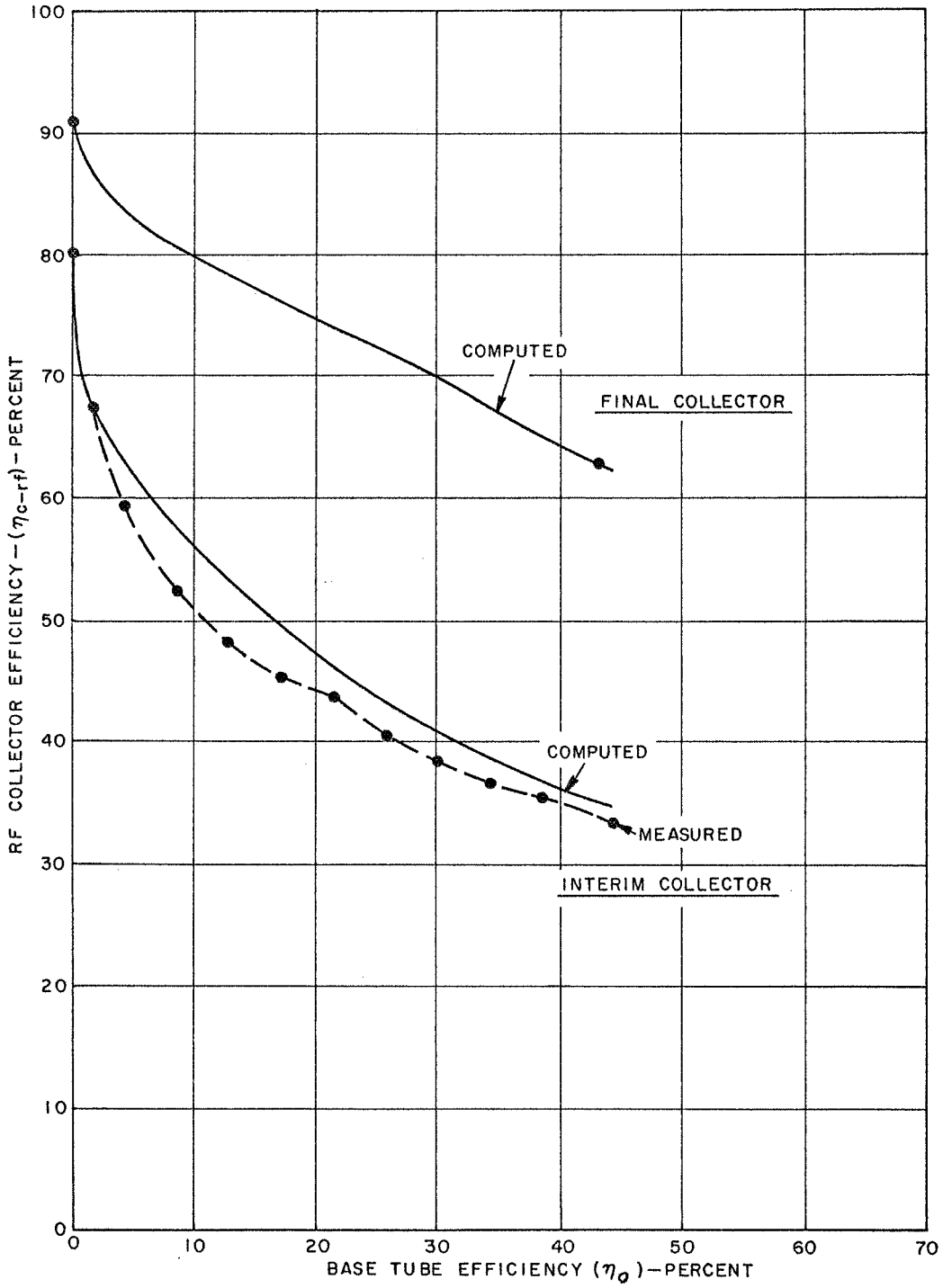

Figure 32 - Computed RF Efficiency of Final Collector

power conversion efficiency achieved was 44 percent, and this was assumed to occur at full rf output swing.

The predicted performance of the final collector shown in Figure 32 is nearly twice as good as the performance of the interim collector. Rather than achieving a 35-percent collector efficiency at full power output, predictions indicate that the final collector will achieve an rf collector efficiency of 62 percent. This figure is nearly as good as the 65-67 percent predicted efficiency for the graded spike collectors. Therefore, the construction of the final collector was based on the design presented here.

The construction and evaluation of the final collector are described in the next two sections.

CONSTRUCTION OF FINAL COLLECTOR

The final collector and tube are constructed as a sealed-off vacuum system with an ion pump, similar to the construction of the interim collector. The spike is identical to the one used previously, and the cup is water cooled as before. The suppressor grid and the active electrodes #3 through #11 shown in Figure 33 are supported by threaded stainless-steel rods which also serve as the electrical connection. Each electrode is supported by two rods. The leading edge of all the electrodes, made of molybdenum, is machined to a sharp angle so that end-on incidence of electrons is minimized. The lower surfaces of the electrodes are roughened to reduce secondary emission which degrades collector performance. Four radial slits, two inches long, are cut into each electrode to prevent buckling at elevated temperatures. The entire collector housing is water cooled by means of the pipe brazed to the outer surface. Except for the spike and cup, all the electrodes are radiation cooled. The suppressor grid, which is made of platinum-clad molybdenum, is very coarse and has more than 90 percent transmission. The collector is attached to the test klystron exactly as before.

Figure 34 depicts the cup, suppressor grid, and spike. All the threaded rods may be seen in this view. The assembled electrode stack is shown in Figure 35, where the roughened surface near the aperture of plate #11 may be seen. The tube with the ten-stage collector and the ion pump are shown in Figure 36 while on the exhaust set.

After the cathode was cleaned and recoated with oxide emission mix, the tube and collector were subjected to a standard pump-down and bakeout.

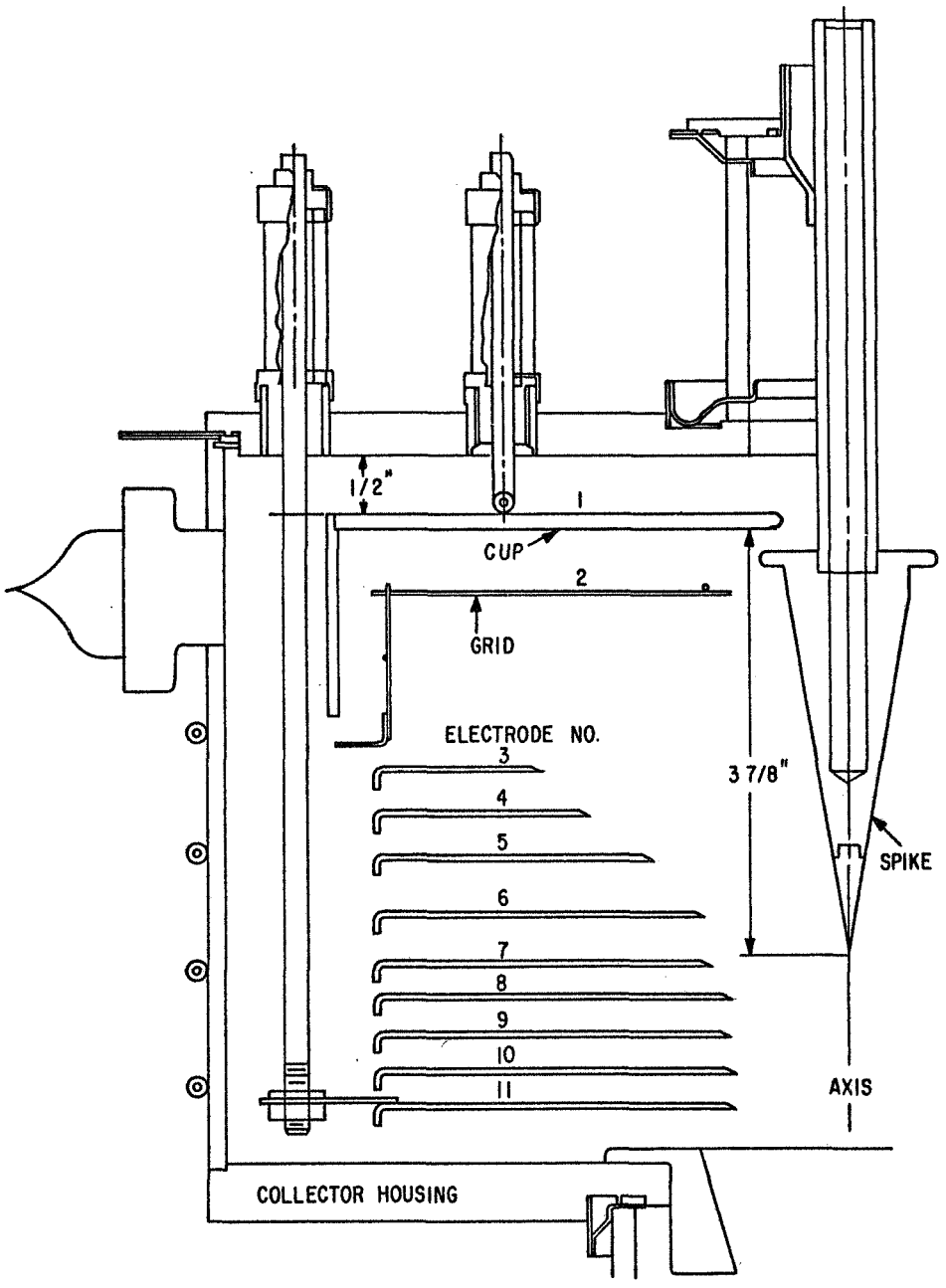

Figure 33 - Final Collector Layout

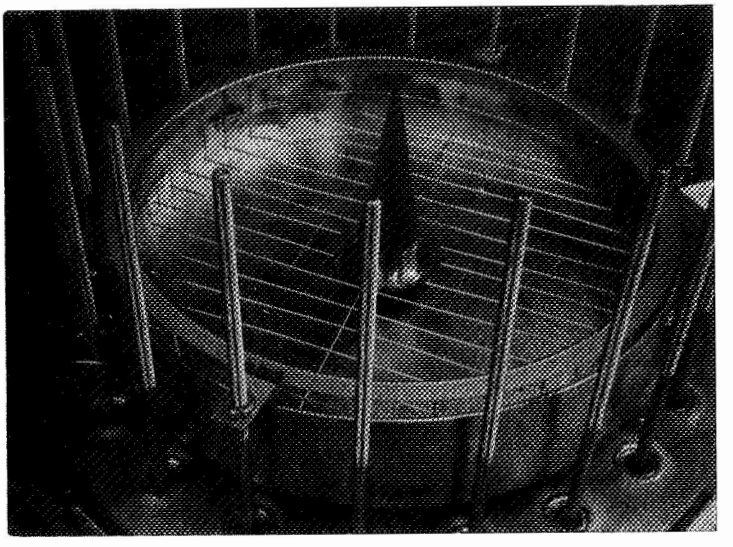

Figure 34 - Spike, Cut, Suppressor Grid and Supporting Rods

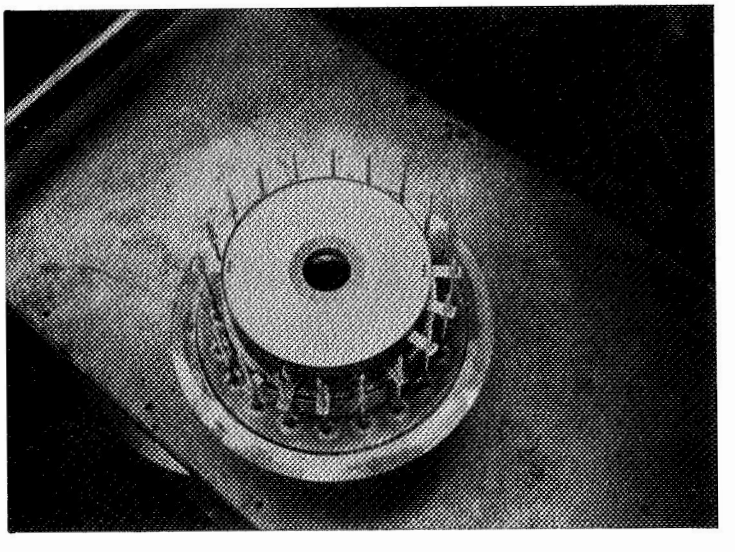

Figure 35 - Electrode Stack Showing Roughened Surface

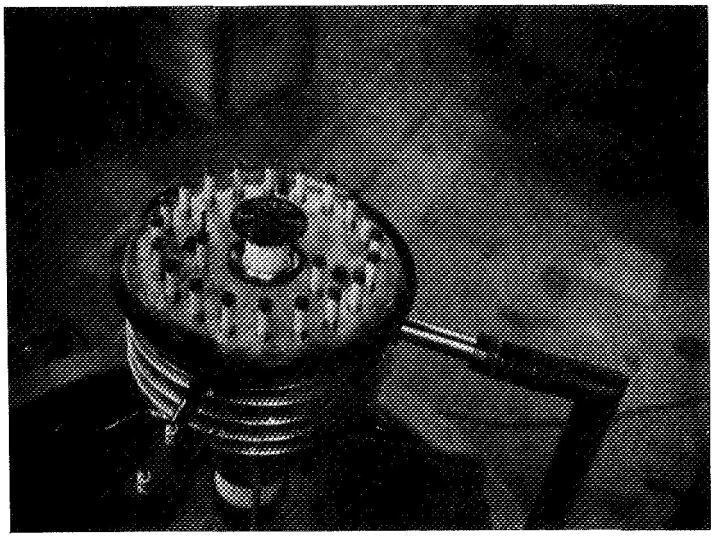

Figure 36 - Assembled Collector and Tube on Exhaust Set

The exhaust operation went smoothly, and subsequent high-voltage tests of all feedthrough insulators showed no electrically conducting films on any ceramic. The tube was immediately installed in the socket for testing.

PERFORMANCE OF FINAL COLLECTOR

The performance of the final collector came very close to theoretical predictions. To achieve this performance it was necessary to install a coil around the taper section between the tube and collector. This coil acted as a magnetic lens and diverted current carried by low-energy electrons from the collector housing to one or more of the collector electrodes, thus increasing collector efficiency.

RF Collector Efficiency

The tube was usually operated with full or partial rf drive in order to spread the spent beam power more or less uniformly over a number of electrodes. Operation under dc conditions was limited by a rise in temperature and gas pressure because only a few electrodes receive the entire collector current. The rf power output could be reduced to about one-half its maximum value before serious outgassing occurred; hence, the data in this section are limited to the region between one-half and full power output.

Measurements of the recovered power as a function of rf power output are plotted in Figure 37. The lower dashed curve represents the best

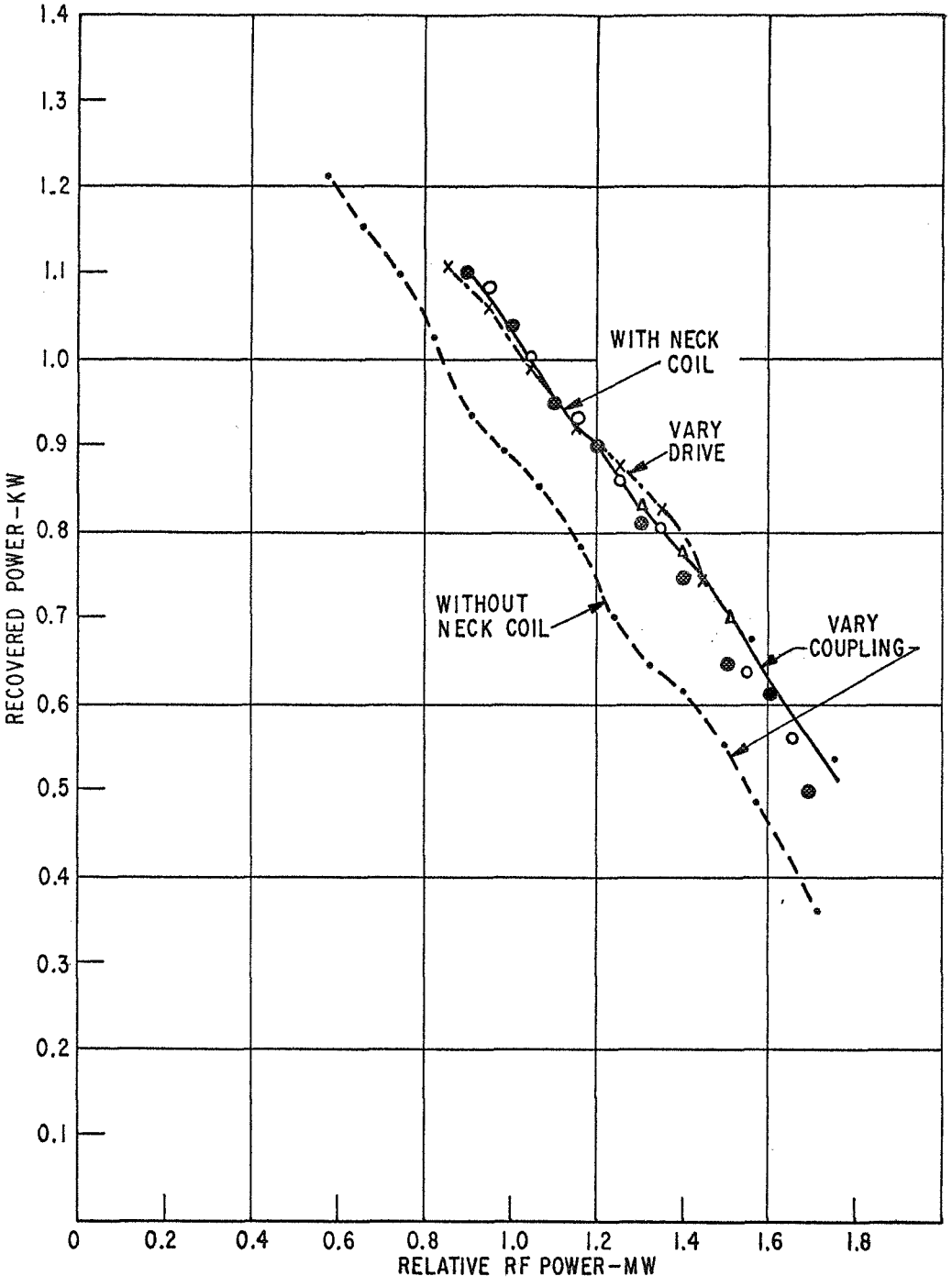

Figure 37 - Recovered Power as a Function of RF Power

performance that could be achieved without the addition of the pre-collector neck coil. When the coil was added, the recovered power increased by 150 watts over the entire range of power output, as shown by the solid line. This coil consisted of approximately 100 turns wound on the 4-1/2-inch diameter of the tube. Optimum coil current was in the vicinity of 3.5 amperes. The data presented here were taken in an interleaved manner. Starting at a relative power output of 1.69 mW, the power output was dropped in steps of 0.1 mW to 0.9 mW, as shown by the solid circle data points (1.65 mW equals 1165 watts internal rf power). The power output was then increased in 0.1-mW steps from 0.95 mW to 1.65 mW, as shown by the hollow circle data points. Finally, the power output was again reduced in 0.1-mW steps from 1.6 mW to 1.3 mW, yielding the points indicated by the triangles in Figure 37. During these measurements the rf output power was reduced by overcoupling the output cavity, while rf drive power was held constant.

Also shown in Figure 37 are a series of data points indicated by crosses. For this run, the output cavity was overcoupled slightly, reducing relative power output from 1.69 mW to 1.46 mW. This point corresponded to the best power output achieved on the interim collector tests. The output coupling was then held constant and the rf power output was reduced by decreasing drive power. These data points fall closely in line with the earlier data points, indicating that the spent beam power distributions under the two conditions of overcoupling and of reduced drive power were quite similar.

The measured rf collector efficiency data of Figure 37 are in excellent agreement with theoretical predictions, as can be seen in Figure 38. Computed curves and measured data points are given in this figure for both the interim collector (lower) and the final collector (upper). The crosses represent collector efficiency corrected only for dc interception ($\alpha = 0$), while the circles represent data corrected for the total intercepted current ($\alpha = 0.5$). In calculating the rf collector efficiency from the measured data, the output circuit efficiency was taken to be 90 percent, based on the measured loaded and unloaded Q factors of 250 and 2500 for this tube when optimally coupled. When the output is overcoupled, this efficiency is slightly higher. The agreement is excellent in the region from 25 to 45 percent efficiency. Above an efficiency of 45 percent, the measured data are somewhat scattered. It was noted in this region that the tunnel current was increasing rapidly. Whether this power interception is due to beam interception prior to entry into the collector, or is due to a rapid increase in electrons returned from the collector is not clear. If it is the former (the collector should not be charged with receiving this power), the calculated collector efficiency becomes 63 percent at the highest base efficiency point (at $\eta_o = 54.3$ percent) instead of 51.1 percent. The computed change in collector efficiency due to this rf interception is smaller at lower base efficiency. At the lower power data

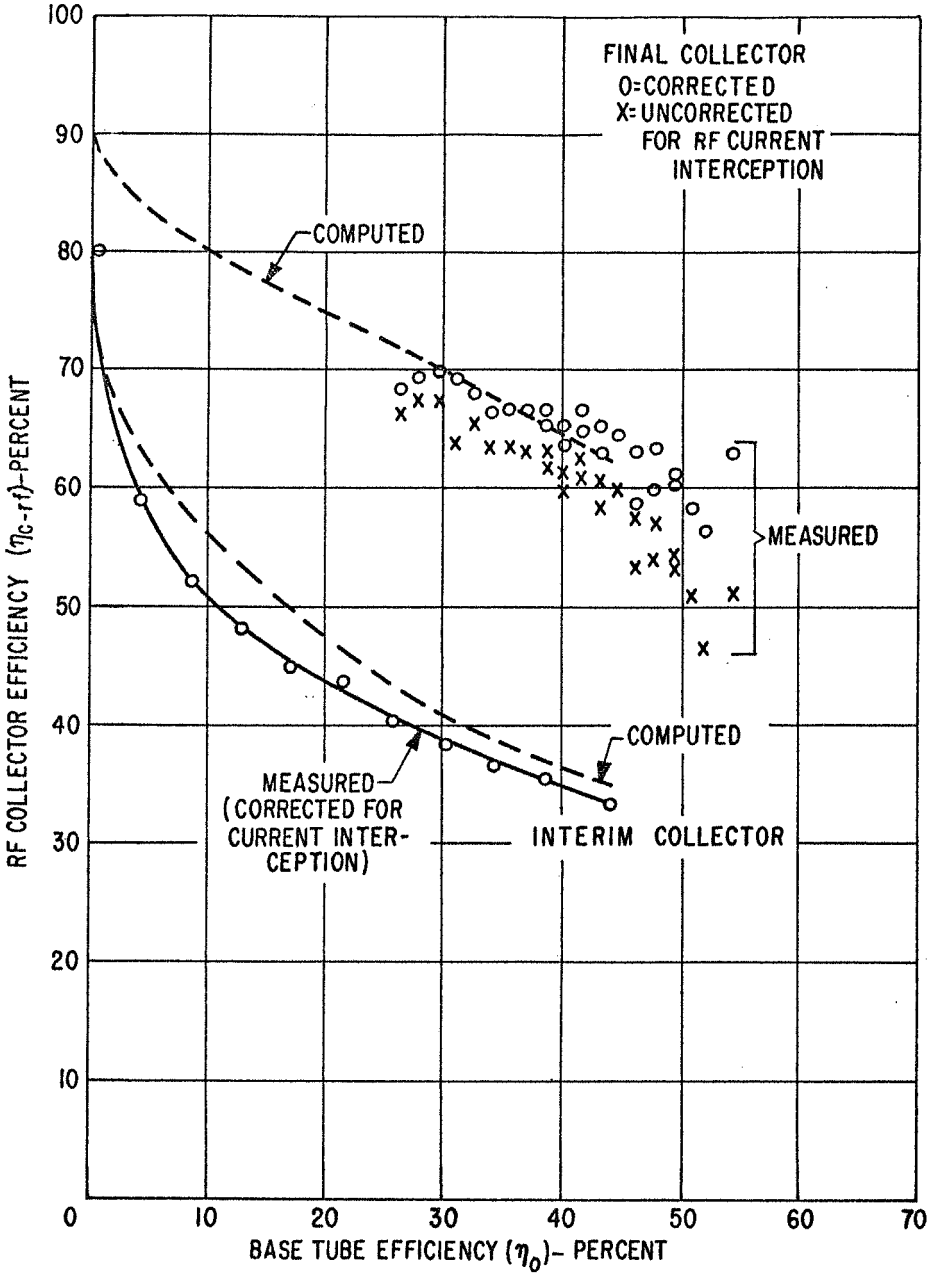

Figure 38 - Comparison of Measured and Calculated RF Collector Efficiencies

points, this correction increases collector efficiency by only two percentage points. The additional intercepted electrons due to rf are assumed to be traveling at one-half the dc beam potential in calculating this correction. In all of the data presented in this section, the collector has not been charged with the current intercepted under dc conditions. In the run shown in Figure 38, the dc current interception was only 4 mA out of 320 mA; hence this involves a correction of only 28 watts in spent beam power entering the collector.

Net Tube Efficiency

The most practical characteristic of a depressed collector is its ability to increase base tube efficiency η_o to a higher net tube efficiency η. In Figure 39, computed and measured net tube conversion efficiency is plotted as a function of base tube efficiency. For a klystron with a base efficiency of 54.3 percent, the net tube efficiency is increased to 70.9 percent, an increase of 16.6 percentage points. This is about twice the improvement reported in the past, as is evident from Figure 1. Sterzer's point at 58 percent still lies above the extension of the curve reported here, but (from his Figure 11[4]) it should be noted that when Sterzer reduced drive power by only 20 percent, the net tube efficiency dropped rapidly from 58 to 42 percent, indicating a lack of stability. Sterzer's published data do not appear to be complete enough to allow definitive evaluation of his collector performance.

Dynamic Collector Electrode Impedances

As part of the required tests of the final collector, the electrode voltages were varied individually and the changes in electrode currents were recorded. The results are given in Table III where the first three columns denote the electrode number and standard operating conditions with the output cavity overcoupled such that the base conversion efficiency η_o is 45.3 percent. The change in voltage and current and the associated impedance, together with the maximum and minimum collector efficiency, are given in the remainder of the table. In general the impedance looking into the electrode terminals is seen to be quite high, the lowest value being 29 kilohms. It is important to note, however, that some of these resistances are negative. The change in collector efficiency as electrode voltages are changed is seen to be minor, which means that its performance is not critically dependent on exact electrode voltages. The power supplies used with this depressed collector may therefore exhibit poor regulation without seriously degrading the collector efficiency.

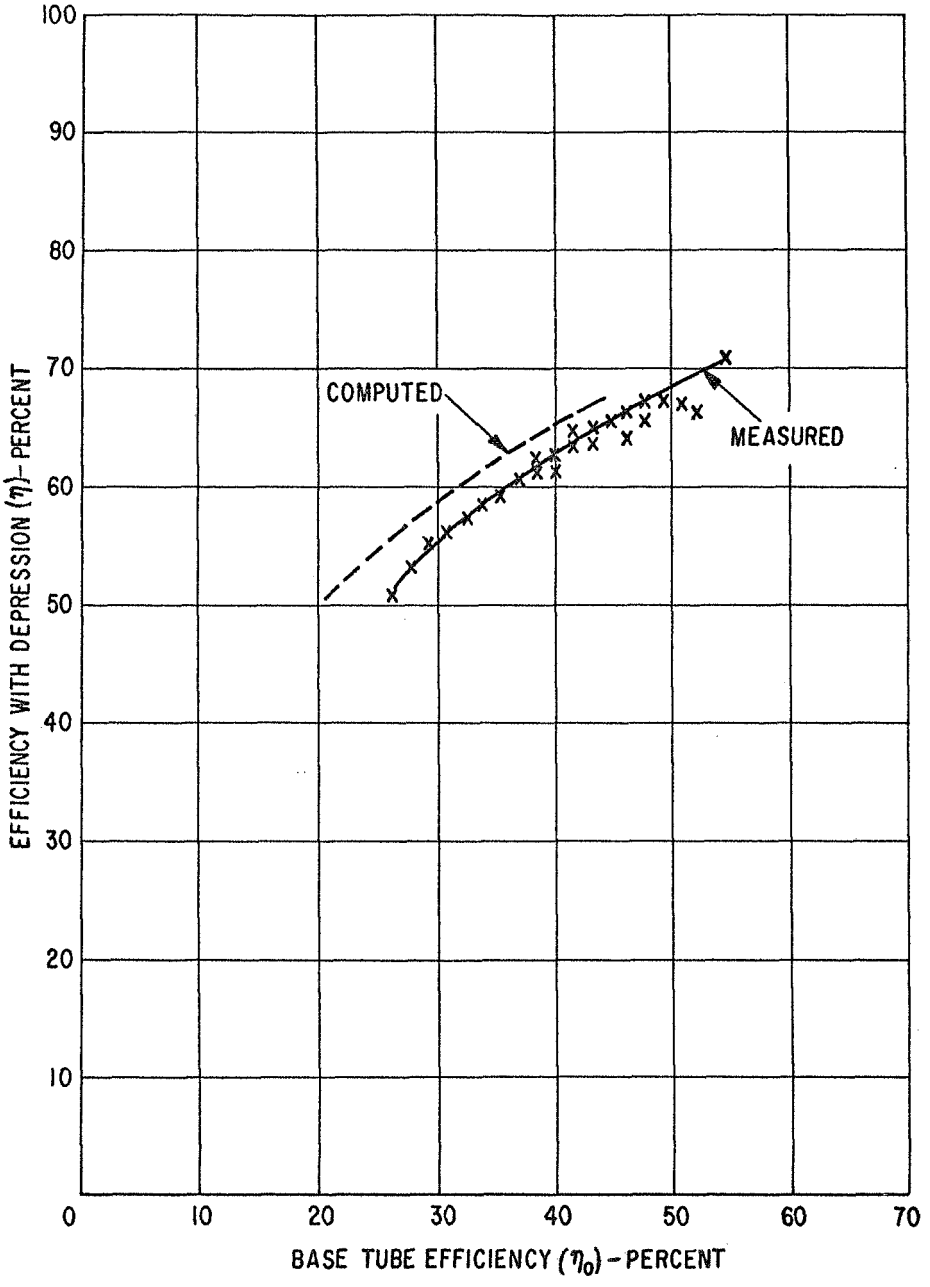

Figure 39 - Net Tube Efficiency as a Function of Base Tube Efficiency

TABLE III - ELECTRODE IMPEDANCES

Electrode #	Standard Values V	Standard Values I	volts ΔV	mA ΔI	kΩ Z	volts ΔV	mA ΔI	Ω Z	η_{c-rf} min.	η_{c-rf} max.
Cup 1	-6.95kV	20 mA	-	-	-	+400	+1	400KΩ	63.4	63.5
Grid 2	-7.11	0	-	-	-	-	-	-	-	-
3	-6.35	5	-200	-1	200KΩ	+400	0	∞	64.3	66.2
4	-5.72	10	-200	0	∞	+400	0	∞	64.5	67.0
5	-4.98	5	-200	-2	100	+200	-2	-100	63.5	63.8
6	-4.42	18	-200	+1	-200	+200	-1	-200	64.0	66.3
7	-3.63	36	-200	-3	68	+400	+3	133	63.3	66.7
8	-3.08	31	-200	+1	-200	+200	+2	100	63.0	63.7
9	-2.42	40	-200	-7	29	+200	-1	-200	63.7	64.6
10	-1.56	48	-200	0	∞	+200	+3	68	61.7	63.2
11	- .9	43	-200	+2	-100	+200	+1	200	60.7	63.9
Cathode	-7.11	-320	-	-		-	-	-	-	-
Body	0	24	-	-		-	-	-	-	-
Coll. Housing	0	54		-		-	-	-	-	-

Notes:

(a) All voltages measured with respect to tube body.

(b) All currents are assumed to flow into the tube

(c) Under standard conditions for this test $\eta_{c-rf} = 64.1\%$.

(d) Grid (electrode #2) is kept 160 v. negative with respect to cup at all times.

(e) All the given values of η_{c-rf} are corrected for interception with $\alpha = 0.5$.

(f) $\eta_o \approx 45.3\%$ for this test.

Effect of Interelectrode Shorts

Using approximately the same starting conditions listed in Table III, pairs of electrodes were systematically shorted together to ascertain the drop in collector efficiency. The results are listed in Table IV. No instabilities or oscillations were observed in any of the test performed. The corrected collector efficiency at a base tube efficiency of 43.0 percent decreased from 65 percent with all electrodes normal to a low of 58.2 percent when electrodes #9 and #10 were shorted. Shorting of other electrode pairs produced a lesser degradation of efficiency. It may be concluded from this test that a single interelectrode short circuit does not seriously impair collector performance.

- - - - - - - -

TABLE IV - EFFECT OF INTERELECTRODE SHORTS

Short (Electrode #)	$\eta_{c\text{-}rf}$
none	65.0
grid - 3	63.5
3-4	61.3
4-5	61.9
5-6	61.3
6-7	59.7
7-8	59.3
8-9	59.8
9-10	58.2
10-11	64.1

Notes:

(a) η_o = 43 percent during this test

(b) all values of $\eta_{c\text{-}rf}$ are corrected for interception with $\alpha = 0.5$

Output Spectrum Analysis

In an effort to determine the presence of any spurious oscillations, a spectrum analyzer was used to compare the driver and the klystron output spectrum under the standard rf operating conditions listed in Table III. The operating frequency of the klystron was 726 MHz and the spectrum analyzer filter was set for a bandwidth of 1 KHz which was swept across the signals at the rate of 15 KHz/sec. The results of this test are given in Figure 40 where both the input and the output are shown. The gain of the tube at this point was approximately 20 dB. The vertical scale is 11.7 dB/div. while the horizontal scale is 30 KHz/div. A comparison of the two spectra shows no spurious signals being introduced by the klystron or its collector in this band of frequencies. The driving source is seen to have fm variations comparable with the bandwidth of the klystron. A small difference in the noise level in the skirts of the spectrum appears to exist. Since it is not possible to operate this tube undepressed without risking serious collector damage, the precise source of this small added noise could not be determined.

The output spectrum was observed visually while the klystron rf drive was varied from zero to saturation. No changes in the spectrum other than amplitude were detected. It can therefore be concluded that the collector does not introduce any serious oscillations in this band of frequencies.

Current Distribution to the Electrodes

The current distribution to the various electrodes has been plotted in Figures 41 through 44 as a function of the base tube efficiency η_o. The electrode number (see Figure 33) and its voltage during these tests are given for each curve. The base efficiency was varied by changing the drive in the region from 26 to 45 percent. Above a conversion efficiency of 45 percent, both drive and coupling to the output cavity were changed. The current to the lower voltage electrodes is seen to increase as the efficiency increases. The opposite is true for the higher voltage electrodes. The grid current was below one milliampere during all tests that were performed. The spike current was essentially zero. Because the electrode voltages are determined by a resistive divider, they do not remain absolutely constant during the entire run. The maximum change in any one voltage is, however, less than two percent. In the calculation of the efficiencies reported earlier, the true voltages were used for each point. Data below a base efficiency of 26.1 percent were not taken because of the heavy gas evolution that occurs when most of the current impinges on one or two electrodes. Further operation of the tube will eventually eliminate this problem.

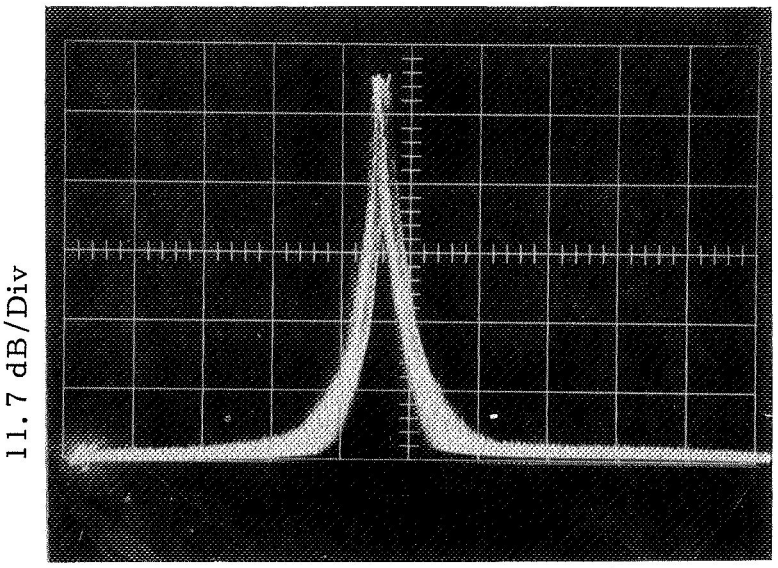

Input Spectrum

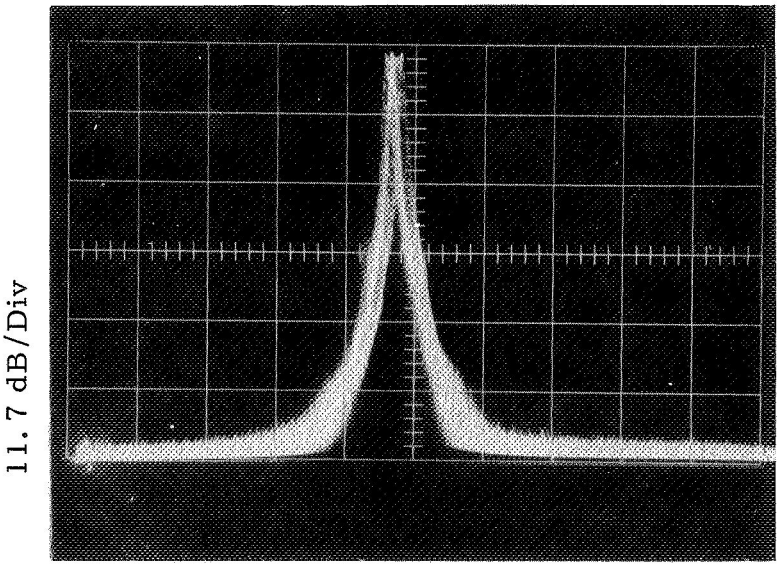

Output Spectrum

Figure 40 - Input and Output Frequency Spectra
(2 sec/cm Time Sweep, f_o - 726 MHz,
1 KHz BW Filter

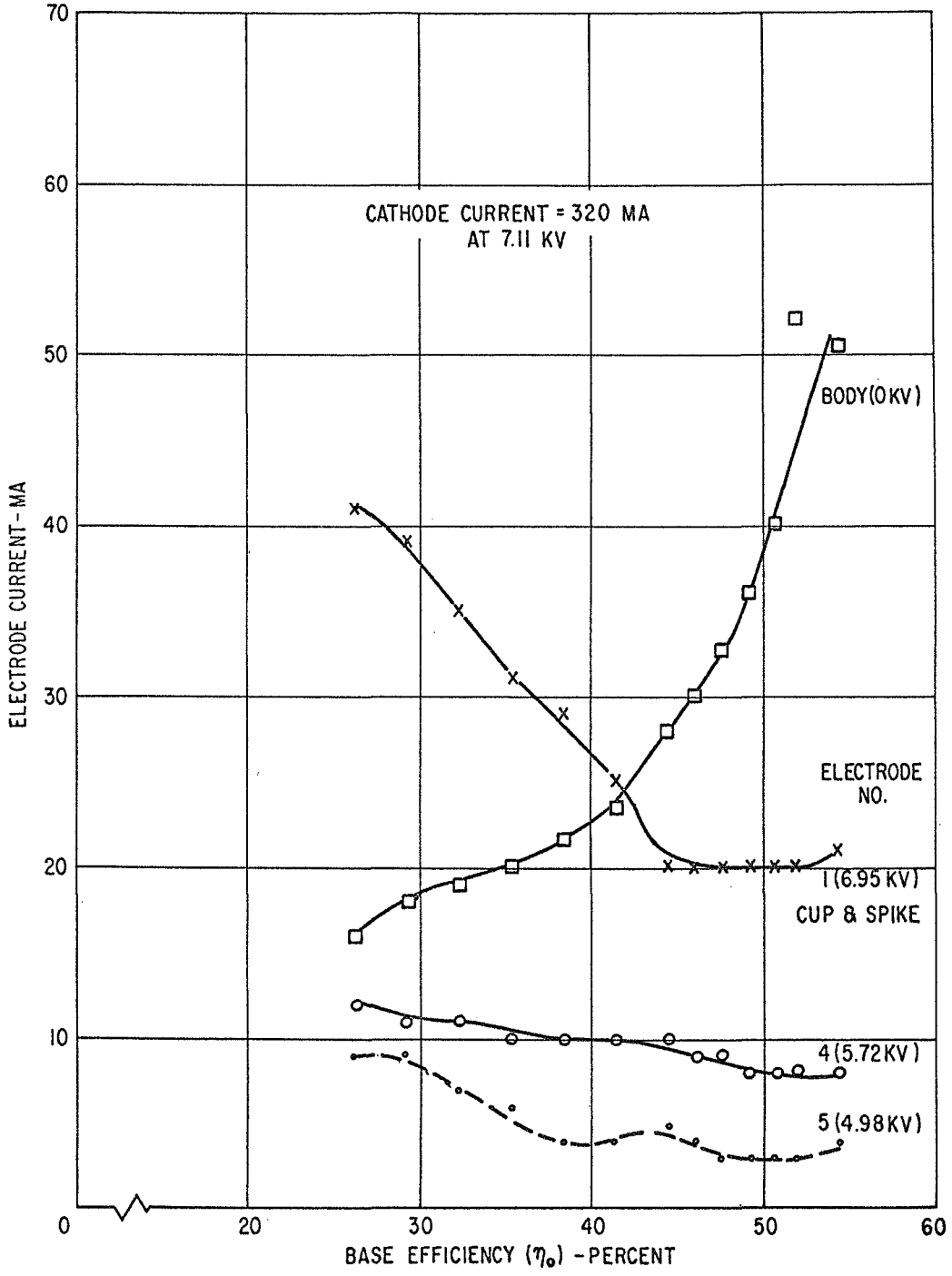

Figure 41 - Electrode Currents versus Base Efficiency
(Body and Electrode Nos. 1, 4 and 5)

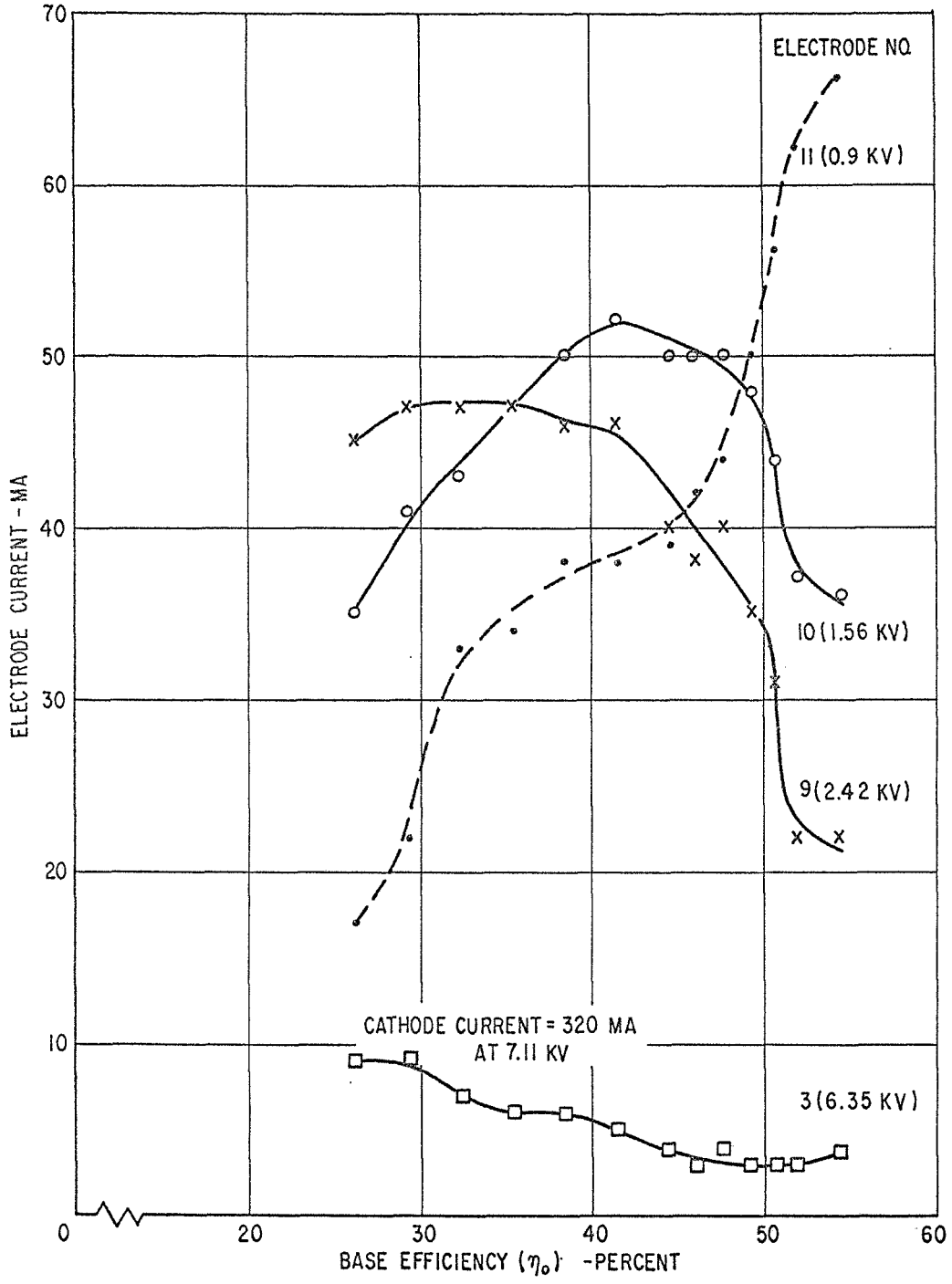

Figure 42 - Electrode Currents versus Base Efficiency
(Electrode Nos. 3, 9, 10 and 11)

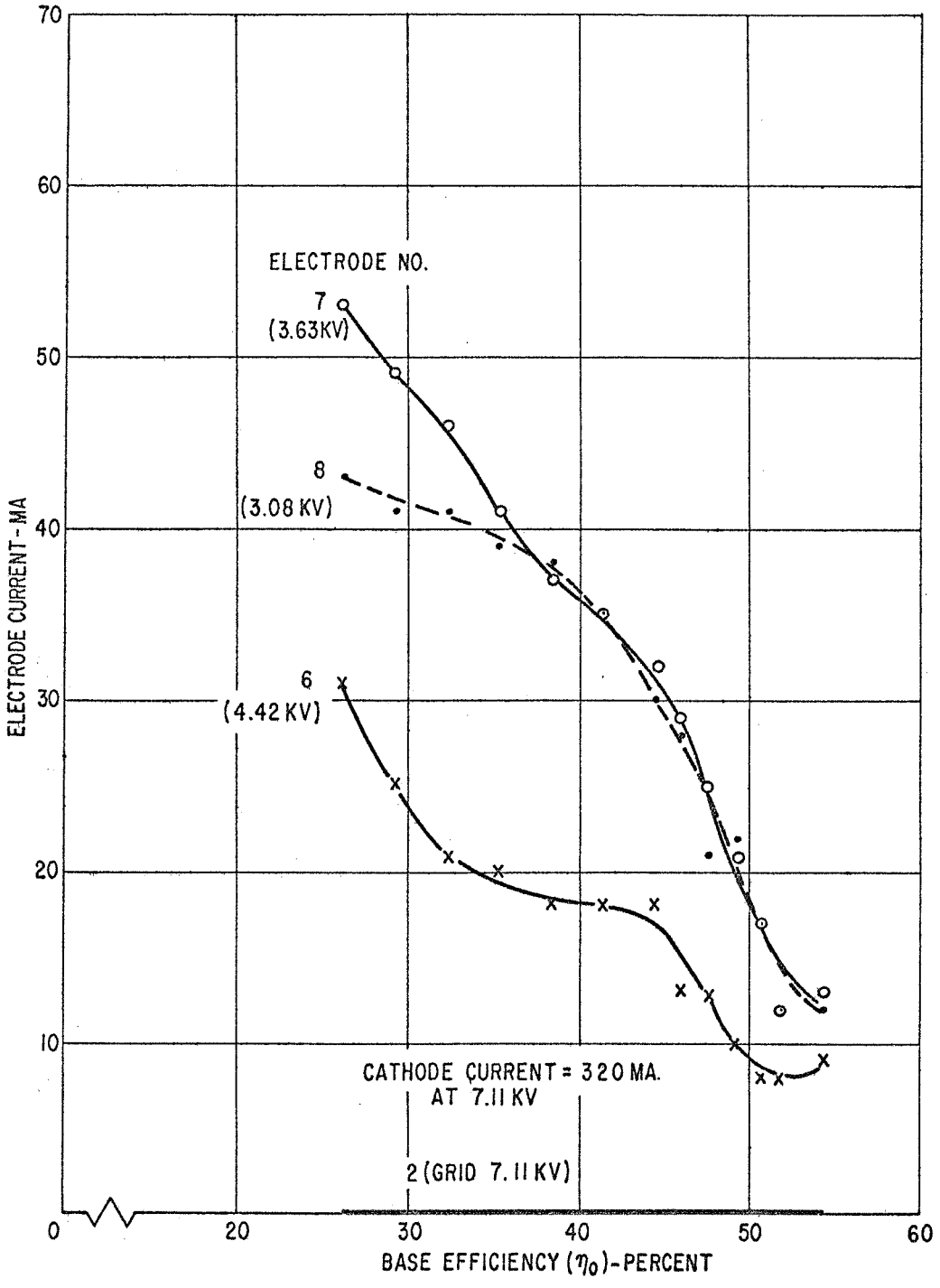

Figure 43 - Electrode Currents versus Base Efficiency
(Electrode Nos. 2, 6, 7 and 8)

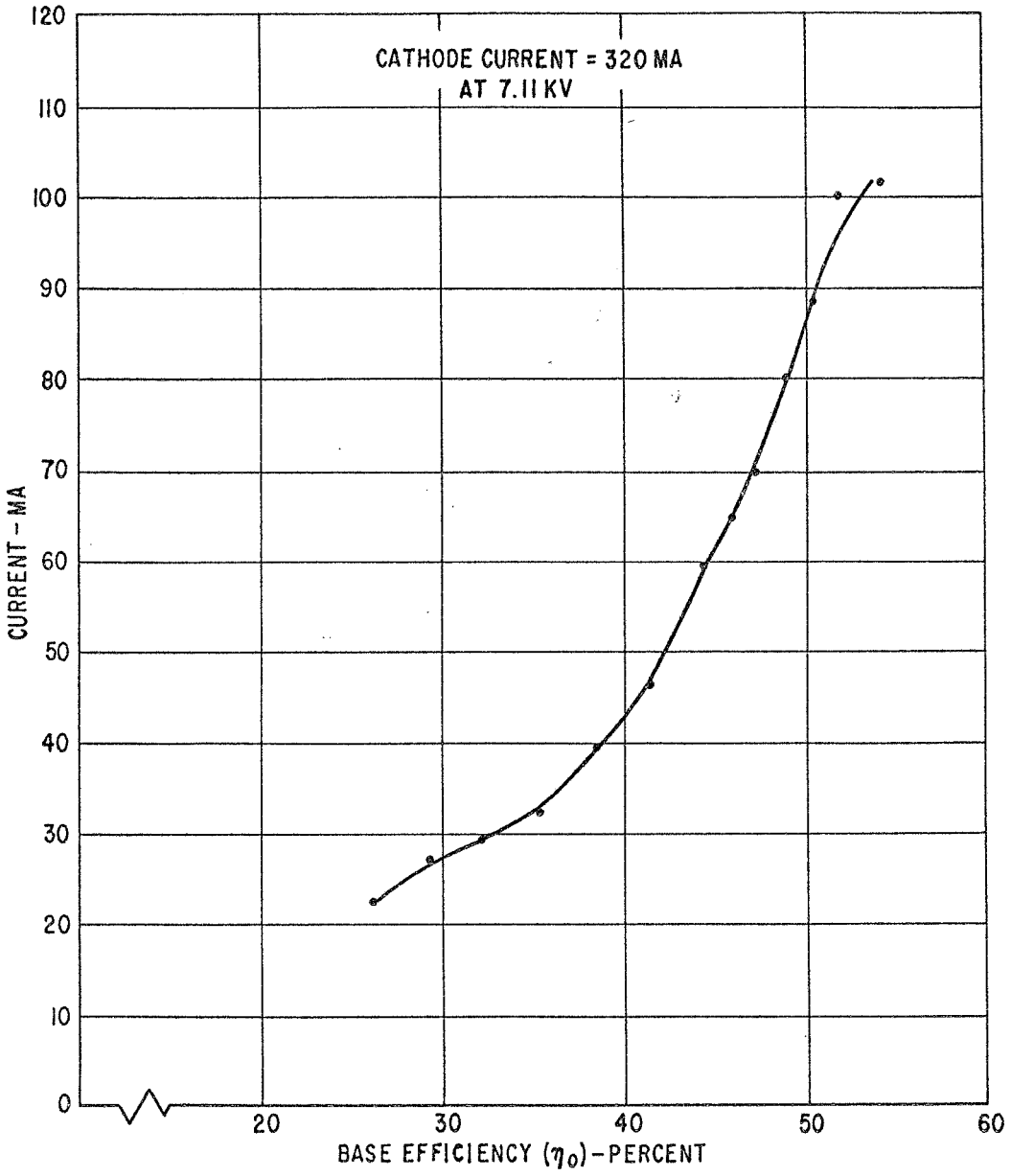

Figure 44 - Collector Housing Current versus Base Efficiency

DISCUSSION OF RESULTS

A design method for depressed collectors, based on analog computer trajectory calculations, has been established and verified. Both of the collectors built under this program exhibit performance which is in excellent agreement with theoretical predictions. It was shown that an electrostatic reflex depressed collector can contribute significantly to the efficiency improvement of klystron microwave amplifiers. It was also shown that this improvement can be achieved without the occurrence of any spurious oscillations or other instabilities.

Another important result demonstrated in this program is the insensitivity of the reflex collector performance to the precise voltages on the active electrodes. This implies that all power supplies except the one providing cathode to anode voltage may have poor regulation without seriously degrading the performance of the collector. The collector was also shown to be relatively rugged electrically because the deliberate short circuiting of individual electrode pairs did not reduce the collection efficiency appreciably.

One of the main obstacles in designing successful collectors is the absence of specific knowledge regarding the vector velocity and radial position distributions present in a spent klystron beam under various conditions of rf power output and with different magnetic field configurations. Unless this knowledge is available from either theory or experiment, an optimum collector cannot be designed by the methods developed in this program. At best, a reasonably good collector can be designed by making certain plausable assumptions regarding the vector velocity distribution and the beam diameter. The efficiency improvement through the use of the neck coil was probably due to its ability to change the conditions in the spent beam to a form close to those assumed in the calculations.

CONCLUSIONS

A ten-stage reflex electrostatic collector has been successfully designed and demonstrated. Its measured performance agrees with predicted performance both in absolute value and in variation with rf power output. A typical measured collector efficiency is 63 percent, taking a base tube efficiency of 54.3 percent up to a net tube efficiency of 70.9 percent. For a lower base tube efficiency of 25 percent, the collector efficiency approaches 70 percent, leading to a net tube efficiency of 50 percent.

The final collector was designed on the basis of an analog computer analysis which was verified by earlier measurements on an interim collector. The success of the analysis indicates that the computer program is basically valid.

An additional focusing field obtained from a small neck coil preceding the collector was required to achieve optimum performance. This coil increased recovered power by 150 watts, which represents a 30 percent increase at full rf power output.

RECOMMENDATIONS FOR FUTURE WORK

Recommendations for future work fall into two categories:

(1) Additional measurements and comparison with analog computations on the existing final collector.

(2) A scaling study of future collector designs with respect to frequency and power handling capacity.

These categories will now be discussed.

ADDITIONAL WORK ON EXISTING COLLECTOR

The successful operation of the final collector is due in great measure to two features: (1) the suppressor grid, and (2) the pre-collector neck coil. The successful operation of the suppressor grid can be inferred from the

successful rf performance of the collector. It would be much more satisfying, however, to take data showing collector efficiency between V_o and $2V_o$, similar to that shown in Figure 17. This would verify that the loss of efficiency due to cup secondaries has indeed been eliminated.

The action of the pre-collector neck coil should be investigated on the analog computer. It seems reasonable to infer that this coil allows the beam diameter to be fine-tuned to fit the low energy portion of the electrode edge locus. It is not clear, though, why this fine adjustment should be necessary. It would be informative to use the analog computer to examine the effect of this coil on both forward-going and reflected low-energy electrons.

As the existing tube/collector system ages-in over a period of weeks and months, outgassing under dc conditions should minimize, and it will become possible to take a dc collector efficiency characteristic as a function of beam voltage. This characteristic approximately represents a mathematical differentiation of the rf collector efficiency characteristic shown in Figure 38. The current to the various electrodes can be measured and compared in a fashion similar to that shown in Figures 14 and 15. Hopefully, from this data some new and useful inferences can be made about the characteristics of the spent beam as it enters the collector. These input conditions still remain the single greatest unknown factor in collector design.

FUTURE COLLECTOR DESIGNS

The question of scaling reflex collector designs to different power levels and different frequencies needs careful study. The present collector will work just as well at 12.2 GHz provided the beam perveance and the ratio V/B^2L^2 are held constant in scaling the size of both the tube and collector. V, B, and L represent the voltage, magnetic field amplitude, and linear dimension respectively. These scaling laws can be deduced from the Lorentz force equation and Gauss' Law without making any assumptions regarding cathode immersion as shown by Pierce[21]. There is a point, however, at which thermal dissipation places a lower limit on collector size. This thermal limitation might require that in a practical case a larger collector-length (L) to beam-radius (b) ratio be used than in the existing collector. A larger L/b ratio would not only increase space charge effects but would also reduce the efficiency loss associated with finite beam size. The larger relative space charge forces would tend to reduce collector efficiency. The specific tradeoffs involved in L/b optimization need to be studied quantitatively before reliable new reflex collector designs can be established at different frequencies and power levels.

REFERENCES

1. Priest, O. H. and Leidigh, W. J., "A Two Cavity Extended Interaction Klystron Yielding 65 Percent Efficiency", IEEE Trans. Electron Devices, Vol. ED-11, pp. 369-373; August 1964.

2. Chen, T. S., Wolkstein, H. J. and McMurrough, R. W., "Theory and Performance of Depressed Trochoidal Collectors for Improving Traveling-Wave-Tube Efficiency", IEEE Trans. on Elec. Dev., Vol. ED-10, pp. 243-254; July 1963.

3. Mihran, T. G. and Neugebauer, W., "Analytic Study of Collectors Using Magnetic Field", NASA Final Report CR- Contract NAS3-11530, August 1970.

4. Sterzer, F., "Improvement of Traveling-Wave Tube Efficiency Through Collector Potential Depression", IRE Trans. on Elec. Dev., Vol. ED-5, pp. 300-305; October 1958.

5. Branch, G. M. and Mihran, T. G., "Analytical Designs of a Space-Borne Magnetically-Focused Klystron Amplifier", Final Report, Contract NAS3-11514, NASA Lewis Research Center, Cleveland, Ohio; October 25, 1968.

6. Haeff, A. V. and Nergaard, L. S., "A Wide-Band Inductive Output Amplifier", Proc. IRE, Vol. 28, pp. 126-130; March 1940.

7. Litton, C. V., "Electrode Structure for Velocity Modulation Tubes", U.S. Patent No. 2325865; August 3, 1943.

8. Cutler, C. C. and Brangaccio, D. J., "Factors Affecting Traveling-Wave Tube Power Output", IRE Trans. on Elec. Dev., Vol. PGED-3, pp. 9-23; June 1953.

9. Winkler, R. H., "A Method of Improving the Efficiency of Klystrons", Microwave Lab. Rpt. No. 235, Stanford University; May 1954.

10. Laico, J. P., McDowell, H. L. and Moster, C. R., "A Medium Power Traveling-Wave Tube for 6,000-Mc Radio Relay", BSTJ, Vol. XXXV, pp. 1285-1346; November 1956.

11. Wolkstein, H. J., "Effect of Collector Potential on the Efficiency of Traveling-Wave Tubes", RCA Rev., Vol. XIX, pp. 259-282; June 1958.

12. Dunn, D. A., Luebke, W. R. and Wada, G., "A Low Potential Collector Employing an Asymmetrical Electrode in an Axially-Symmetric Magnetic Field", IRE Trans. on Elec. Dev., Vol. ED-6, pp. 294-296; July 1959.

13. Dunn, D. A., Borghi, R. P. and Wada, G., "A Crossed-Field Multi-segment Depressed Collector for Beam-Type Tubes", IRE Trans. on Elec. Dev., Vol. ED-7, pp. 262-267; October 1960.

14. Murata, S. and Kinoshita, S., "Collector Potential Depressed Klystron", Record of Int'l Cong. on Microwave Tubes, Munich, June 7-11, 1960, Friedr. Vieweg & Sohn, Braunschweig, pp. 64-72.

15. Hansen, J. W. and Susskind, C., "Improvement of Beam-Type Performance by Collector-Potential Depression, and a Novel Design", IRE Trans. on Elec. Dev., Vol. ED-7, pp. 282-288; October 1960.

16. McCune, E., "Depressed Collector Klystron (VA-843) Development Program", Final Report Varian Associates, Contract No. DA 36-039-sc-78093; March 1961.

17. Met, V., "Depressed Collector Studies for High Power Klystrons", Final Technical Report, Contract AF 30(602)1500, Task 45083, RADC-TR-61-204, Rome Air Development Center; March 30, 1961.

18. Walder, J., "The Biased Gap Klystron", M.S. Thesis, Cornell University; February 1965. Also, Walder, J. and McIsaac, P. R., "Experimental Analysis of Biased Gap Klystron", IEEE Trans. on Elec. Dev., Vol. ED-13, pp. 950-955; December 1966.

19. Okoshi, T. and Chiu, E., "A 'Soft-Landing' Collector for Improving the Efficiency of Beam-Type Tubes", preprint Dept. of Electronic Engineering, Univ. of Tokyo, Bunkyo-ku, Tokyo, Japan; undated. Also, Okoshi, T., Chiu, E. and Mzusawa, J., "TEF (Tilted Electric Field) Soft-Landing Collector for Beam-Type Microwave Tubes", Trans. Inst. Electronics Comm. Engrs. Japan, Vol. 51, pp. 10-12; November 1968.

20. Sauseng, O., Basiulis, A. and Tammaru, I., "An Analytical Study Program to Develop the Theoretical Design of Traveling-Wave Tubes", NASA Final Report CR-72450, Contract No. NAS3-9719, October 31, 1968.

21. Pierce, J. R., "Theory and Design of Electron Beams", D. Van Nostrand Company, New York, pp. 16-18, 1954.

DISTRIBUTION LIST

	Copies
National Aeronautics & Space Administration	
Headquarters	
Washington, D.C. 20546	
Attn: SA/L. Jaffe	1
SAC/A.M.G. Andrus	10
SC/R.B. Marsten	1
NASA-Lewis Research Center	
21000 Brookpark Road	
Cleveland, Ohio 44135	
Attn: C. C. Conger (MS 54-1)	1
R. E. Alexovich (MS 54-3)	1
Dr. H. G. Kosmahl (MS 54-3)	1
Technology Utilization Officer (MS 3-19)	1
Library (MS 60-3)	2
Report Control Office (MS 5-5)	1
N. T. Musial (MS 501-3)	1
G. J. Chomos (MS 54-5)	50
Spacecraft & Support Proc. Section (MS 500-110)	1
Communication Systems, Inc.	
5817 Columbia Pike	
Falls Church, Virginia 22046	
Attn: J. Bisaga	1
Rand Corporation	
1700 Main Street	
Santa Monica, California 90404	
Attn: Dr. J. Holt	1
NASA-George C. Marshall Space Flight Center	
Huntsville, Alabama 35812	
Attn: RASTR-A/E. C. Hamilton	1
Library	1
NASA-Goddard Space Flight Center	
Greenbelt, Maryland 20771	
Attn: 733/R. Pickard	1
Library	1

	Copies
NASA-Ames Research Center Moffett Field, California 94035	
Attn: OART/MOA/E. Van Vleck (MS 202-6)	1
Library	1
NASA-Langley Research Center Langley Station Hampton, Virginia 23365	
Attn: B. Kendall (MS 173)	1
Library (MS 185)	1
NASA-Manned Spacecraft Center Houston, Texas 77001	
Attn: Library	1
Jet Propulsion Laboratory 4800 Oak Grove Drive Pasadena, California 91103	
Attn: L. Derr	1
Library	1
NASA Scientific and Technical Information Facility P.O. Box 33 College Park, Maryland 20740	
Attn: NASA Representative	3
TRW Systems One Space Park Redondo Beach, California 90278	
Attn: W. A. Finley/Space Vehicle Division	1
General Dynamics, Convair Division P.O. Box 1128 San Diego, California 92112	
Attn: F. J. Dore/Advanced Programs Laboratory	1
Hughes Aircraft Company Space Systems Division 1194 W. Jefferson Boulevard Culver City, California 90230	
Attn: H. A. Rosen/Satellite Systems Laboratory	1

	Copies
General Electric Company Missile and Space Division Valley Forge Space Technology Center P.O. Box 8555 Philadelphia, Pennsylvania 19101	
Attn: H. Collins	1
P. Nadler	1
Federal Communications Commission 521 12th Street Washington, D.C. 20554	
Attn: M. Fine	1
U.S. Information Agency 25M St. S.W. Washington, D.C. 20547	
Attn: IBS/EF/G. Jacobs	1
General Electric Company Tube Department Microwave Tube Operation Schenectady, New York 12305	
Attn: R. Dehn	1
Litton Industries Electron Tube Division 960 Industrial Road San Carlos, California 94070	
Attn: Dr. G. Pokorney	1
J. Orr	1
W. Day	1
Dr. O. Sauseng	1
S-F-D Laboratories, Inc. 800 Rahway Avenue Union, New Jersey 07083	
Attn: Dr. G. Farney	1
Hughes Aircraft Company Electron Dynamics Division P.O. Box 2999 Torrance, California 90509	
Attn: Dr. J. Mendel	1
Dr. I. Tammaru	1

Copies

Watkins Johnson Company
333 Hillview Avenue
Palo Alto, California 94304
Attn: Dr. D. Watkins 1

Varian Associates
611 Hansen Way
Palo Alto, California 94303
Attn: Dr. G. Caryotakis 1
Dr. J. Reutz 1

R.C.A.
Industrial Tube Division
Lancaster, Pennyslvania 17604
Attn: W. P. Bennett 1

Raytheon Company
Research Division
28 Seyon Street
Waltham, Massachusetts 02154
Attn: W. Teich 1
Dr. J. M. Osepchuk 1

Mr. Lawrence Gasch
Aerospace Radar Branch
U.S. NRL
Washington, D.C. 20390 1

Mr. Robert Richardson
Mail No. 1620
Martin-Marietta Corp.
Denver Division
P.O. Box 179
Denver, Colorado 80201 1

Mr. William E. Waters
Sr. Engr. Staff Specialist
3939 Fabian Way
M.S. C-70
Palo Alto, California 94303 1

	Copies
Mr. George Orr Code 733 Goddard Space Flight Center Greenbelt, Maryland 20771	1
Sperry Electronic Tube Division Gainsville, Florida 32601 Attn: H. H. Conners	1
Naval Electronic Systems Command PME 116 Washington, D.C. 20360 Attn: Lt. Commander L. Wardel	1